Title
Fabrication of Thin Films by Pulsed Laser Deposition for Clean Energy Applications

Author
Zhang, Xiaojun

Publication Date
2011

Peer reviewed|Thesis/dissertation

Fabrication of Thin Films by Pulsed Laser Deposition for Clean Energy Applications

By

Xiaojun Zhang

A dissertation submitted in partial satisfaction of the

requirements for the degree of

Doctor of Philosophy

in

Engineering-Mechanical Engineering

in the

Graduate Division

of the

University of California, Berkeley

Committee in charge:

Professor Samuel S. Mao, Co-Chair
Professor Xiang Zhang, Co-Chair
Professor Costas Grigoropoulos
Professor Oscar Dubon

Fall 2011

Fabrication of Thin Films by Pulsed Laser Deposition for Clean Energy Applications

By

Xiaojun Zhang

Abstract

Fabrication of Thin Films by Pulsed Laser Deposition for Clean Energy Applications

by

Xiaojun Zhang

Doctor of Philosophy in Engineering-Mechanical Engineering

University of California, Berkeley

Professor Samuel S. Mao, Co-Chair

Professor Xiang Zhang, Co-Chair

Pulsed laser deposition (PLD) is a physical vapor deposition technique for thin film fabrication. Compared with other techniques, pulsed laser deposition technique has advantages such as stoichiometry, flexibility, versatility, lower deposition temperature, ability to grow metastable materials. Because of these advantages, pulsed laser deposition has been widely used in materials research. In this dissertation, pulsed laser deposition has been used to grow thin films for solid oxide fuel cell, light-emitting diode, and solar cell applications.

Firstly, yttria-stabilized zirconia (YSZ) and cerium dioxide (CeO_2) thin films are deposited in oxygen-deficient environments; their properties are compared to those deposited in oxygen-rich environments. Oxygen-deficient films are highly (001)-oriented, which corresponds to a surface that is expected to be forbidden based on Tasker's theoretical calculation of stoichiometric ionic crystals. A model considering non-stoichiometry-induced surface relaxation and surface atomic density is proposed to explain the orientation phenomenon observed under oxygen-deficient deposition conditions. This model is consistent with previous experimental results for indium tin oxide (ITO), SnO_2 and NiO thin films deposited under similar conditions. Detailed studies of the preferred orientation of these oxygen-deficient ionic crystals are of direct relevance to the fabrication of films for use in solid oxide fuel cells.

Secondly, undoped, Cu-doped, Se-enriched, Cu_2Se-doped, Ag-doped, Ag_2Se-doped, and nitrogen-doped ZnSe films have been grown on fused quartz substrates by pulsed laser deposition. It is found that adding a small amount (~2 mol%) of Cu_2Se can significantly improve crystallinity and (111) texturing of ZnSe films. While the other films are highly resistive,

Cu_2Se-doped ZnSe films are p-type conducting with hole concentrations of $\sim 1.1\times10^{19}$ cm^{-3} and resistivity of ~0.098 Ohm•cm (compared with previous reports of $\sim 1\times10^{18}$ cm^{-3} and 0.75 Ohm•cm, respectively). The successful heavy p-type doping of ZnSe films is attributed to substitution of Zn atoms with Cu while limiting selenium-vacancy-associated compensating defects with additional selenium. Nitrogen doping has turned ZnSe films more favorable to wurtzite structures. Two newly observed Raman peaks at 555 cm^{-1} and 602 cm^{-1} are assigned to N local vibrational modes of hexagonal ZnSe structures. The nitrogen-doped ZnSe films are not conductive, which might be due to compensating defects arising from the presence of native defects or other impurities. This work is of importance to solve doping difficulties and contact problems of wide-bandgap semiconductors.

Finally, batch growth of thin films by pulsed laser deposition has been tried. Using the natural temperature gradient, films with different deposition temperatures have been fabricated together. With change of deposition temperatures, ZnSe films are shown to have problems associated with crystalline defects, selenium loss, or phase separation. ZnSe films with improved crystallinity and no phase separation have been achieved using a 16 mol% Se enriched target. Multi-plume pulsed laser deposition has been proposed and discussed. With directionality of PLD plumes and non-uniformity of PLD films, this system is supposed to be more suitable for high-throughput compound thin film fabrication, which makes it very promising for efficient materials optimization and exploration. High-throughput fabrication of compound thin films has been successfully achieved using this system.

Acknowledgements

First of all, I would like to, express my most sincere gratitude to my research advisor, Professor Samuel S. Mao, for his guidance, encouragement, inspiration, patience and support throughout the entire years. His enthusiasm, optimism and generosity will inspire me most in my future career. I will never forget his friendly talk to help me out of the difficult times. The experiences and opportunities that I have been exposed to at Berkeley are truly unforgettable and unparalleled in my life. I would also like to extend my special thanks to Mr. Paul Berdahl at Lawrence Berkeley National Laboratory for his supervision and valuable discussions.

I would like to thank all of the colleagues I have worked with at Berkeley for their valuable collaboration and friendly help. I am thankful to Coleman Kronawitter, Zhixun Ma, Travis Owens, Matthew Rogers, Ping Xiao, Zhaoyang Chen, Dongfang Liu, Steven Barcelo, Kenneth Russell Carrington, Rula Klini, Lucas Oehlerking, Bin Liu, Deang Liu, Meiying Liu, Dongdong Wang, Hexiang Zhong, Huiying Hao, Bin Li, Feng Ren, Li Ren, Li Zhao, Xiaobo Chen, Derrick Speaks, Timothy Suen, Michael Fina, Matt Beres, Haitao Wang, and Heng Pan.

I would like to thank Jhanis Gonzalez, Xianglei Mao, and Rick Russo for their equipment sharing and suggestions. I would also like to thank Laurence J. Hardwick, Ivan Lucas, and Robert Kostecki for their help with Raman measurement, thank James Wu for making PLD targets. Special thanks are also due to Kin Man Yu and Professor Peter Y. Yu for their patient guidance and in depth discussions that are very helpful to my research.

Finally, I am very grateful to my family for their love and understanding. I would like to thank my brother and parents for their unconditional support and encouragement. They have been always supportive and understanding. This dissertation is dedicated to them.

Table of Contents

List of Figures

List of Tables

Chapter 1
Introduction

1.1 Pulsed Laser Deposition

Pulsed laser deposition (PLD) is a thin film deposition technique that uses a high power pulsed laser beam to strike a target material, vaporize and deposit it as a thin film on a substrate. The first pulsed laser deposition experiment was carried out in the 1960s. [1] However it was not until its success in the growth of high temperature Y-Ba-Cu-O superconducting films that widespread attention was given. [2] Nowadays, because of significant development of laser technology, pulsed laser deposition has become one of the most versatile techniques for oxide film growth.

Although the underlying mechanisms are very complex, the PLD setup and experiment are simple. As shown in Figure 1.1 [3], during the deposition, a pulsed laser beam (pulse duration: 10 to 50 ns) is focused onto the surface of the target material to be deposited. With proper energy fluence (1-5 J/cm^2), each laser pulse vaporizes a small amount of the material. The ablated material is ejected from the target in a form of plume and deposited onto the substrate placed normally opposite to the target. The whole deposition process can be divided into four steps [4-7]:

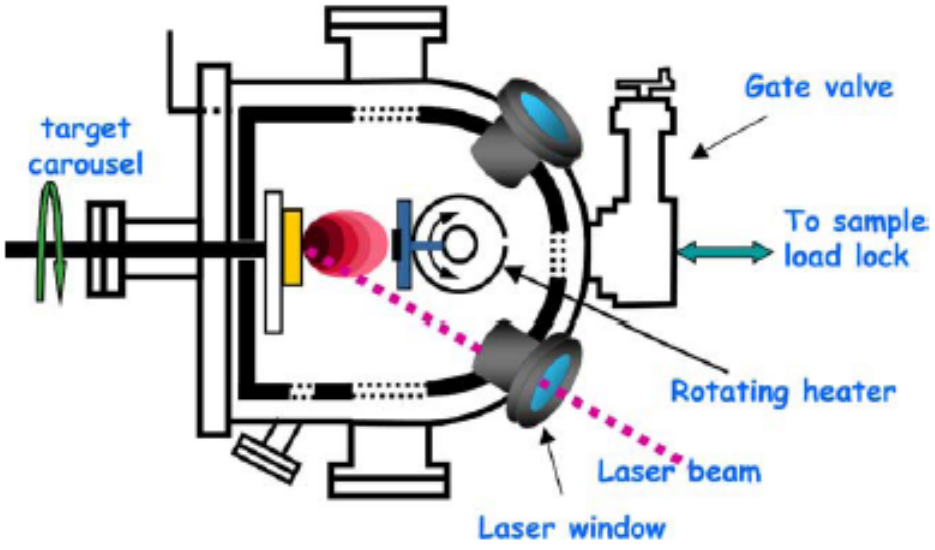

Figure 1.1 Schematic diagram of a pulsed-laser deposition system. [3]

(1) Ablation of the target material and creation of a plasma. At this stage, the incident laser penetrates into surface of the target material. The penetration

depth, dependent on the laser wavelength and absorption coefficient of the target material, is about 10 nm for most materials. Free electrons excited by the laser light oscillate within the electromagnetic field and transfer their energy to the lattice. The material is then heated up and vaporized.

(2) Dynamics of the plasma. The material expands in the plasma parallel to the normal vector of the target surface. The spatial distribution of the plume is dependent on the ambient gas inside the PLD chamber. The flux of the plume can be described by a $\cos^n(\theta)$ (where *n* can vary from 4 to 30) law with a shape similar to a Gaussian curve. The ambient gas interacts with the plume and slows down the highly energetic species.

(3) Deposition of ablated species on the substrate. This stage is important to the quality of deposited film. Highly energetic species from the plume may bombard the substrate surface and sputter off atoms from the surface, which may cause defect formation in the film. The particles emitted from the target collide with the sputtered species from the substrate, which may form particles deposited onto the substrate.

(4) Nucleation and film growth on the substrate surface. Depending on the substrate surface, substrate temperature, background gas, and the deposited material, the deposited species may nucleate in different growth modes and grow into a film.

Pulsed laser deposition has many advantages [8,9]:

(1) The energy source is separated with the vacuum chamber which, in contrast to techniques with vacuum-installed energy sources, can provide a much greater degree of flexibility and geometrical arrangements.

(2) Pulsed laser deposition is versatile. The high power UV laser can ablate almost any condensed matter material.

(3) Thickness of deposited films can be digitally controlled by controlling pulse number. The pulsed nature of PLD also means that film growth rates can be controlled by changing pulse laser frequency.

(4) PLD targets can be much smaller than sputtering targets since the evaporated source material is localized only to the area defined by the laser focus. Therefore, it is very easy to make PLD targets using powder, which makes this technique very flexible in growing new materials.

(5) Because of the high energy density, ablated materials are vaporized stoichiometrically, disregarding of the vapor pressure of the constituents. Therefore, the composition of PLD films is very close to that of the target.

Films can be deposited with expected compositions, even for chemically complex systems. By making different target materials with relatively easy processes such as pressing or annealing of the mixed powders, pulsed laser deposition can be used efficiently to explore functional properties of metal oxide materials or other multi-component materials.

(6) Kinetic energies of the ablated species can promote surface mobility. Therefore deposition temperature can be lower than other techniques.

(7) Deposited species with electronic states far from chemical equilibrium state opens up the potential to fabricate novel or metastable materials that would be unattainable in other techniques.

(8) With a multi-target holder, it is easy and fast to grow multi-layer structures by switching the targets.

PLD also has some technical and fundamental drawbacks [8,9]:

(1) Because of melting and ejection of target surface material, particles with diameters ranging from 0.1 to 10 μm usually are present in PLD films. To reduce particle formation, dense targets with smooth surface should be used. It is also necessary to rotate targets during deposition. A rotating-vane "velocity filter" can also be used to intercept the massive and relatively slow particles while transmitting high-velocity atoms and ions.

(2) The bombardment by deposited species with high kinetic energy can cause crystallographic defects in the film. Using ambient gas can to some extent solve this problem.

(3) The PLD plume is highly directional with a flux of the plume that can be described by a $\cos^n(\theta)$ (where n can vary from 4 to 30) law. The inhomogeneous flux and angular energy distributions within the ablation plume can cause non-uniformity of film thickness. In order to solve this problem, substrate rotation during deposition can be used. In addition, laser beam rastering over a large PLD target can produce uniform and large area films. However, this adds complexity to the process and needs more requirements to the deposition system.

(4) Ablated species can contaminate the laser window. The contamination can decrease the transmittance of the laser beam and affect the deposition rate greatly during deposition. A long tube and a lens with a longer focus length can be used to move quartz laser window away from the target. Ambient gas can also be used to reduce the contamination.

With these disadvantages, pulsed laser deposition is therefore not common in industry. However, it has been widely used in research laboratories to explore new properties or new materials, especially complex compounds.

In this dissertation, pulsed laser deposition has been used to grow oxide thin films for solid oxide fuel cell (SOFC) applications, semiconductor films for light-emitting diode (LED) and solar cell applications.

1.2 Fabrication of Yttria-stabilized Zirconia (YSZ) and CeO_2 Thin Films for Solid Oxide Fuel Cell Applications

Solid oxide fuel cell (SOFC) is an electrochemical conversion device that generates electricity directly from oxidizing a fuel. As shown in Figure 1.2, it has three major parts: anode, cathode, and electrolyte. For electrolyte applications, the oxide film needs to have high oxygen ionic conductivity and low electronic conductivity.

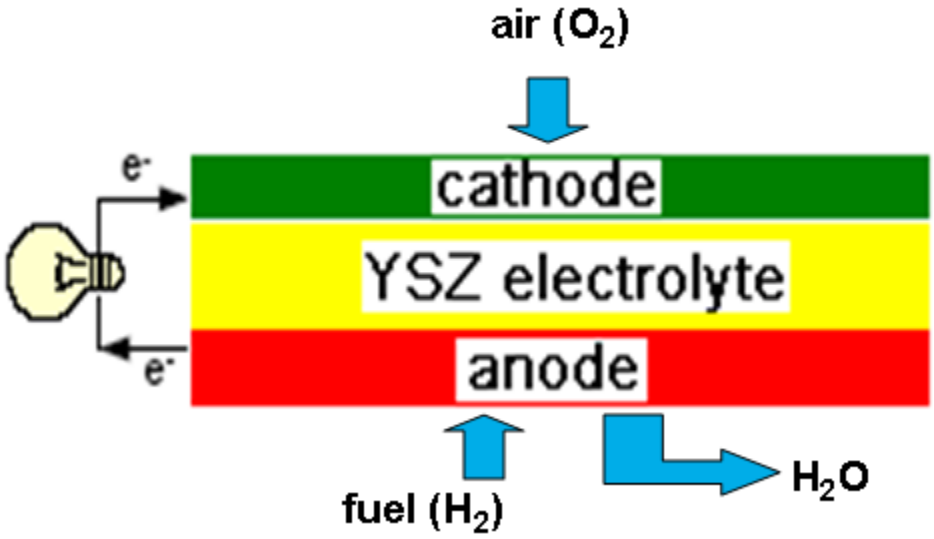

Figure 1.2 Schematic of a solid oxide fuel cell structure.

Yttria-stabilized zirconia and CeO_2 both have fluorite structures as shown in Figure 1.3. [3] Examples of oxide fluorite materials include insulators CeO_2, PrO_2, and HfO_2. High-temperature or yttria-stabilized ZrO_2 cubic phase is also fluorite. The basic fluorite structure can be described as a face-centered-cubic packing of cations, in which all tetrahedral sites are occupied by anions. The unit cell is composed of eight tetrahedra, with cations at the corners and an anion in the center for each tetrahedron. For an ideal fluorite structure with closest packed cations and all anions contacting cations, the radius ratio of cation to anion must be 4.38. A smaller cation to anion radius ratio would leave cations apart such that they would not be closest packed to each other. Although an ideal fluorite structure has a very high atomic density, cation to anion radius ratios are smaller

than 4.38 for all of the known fluorite materials, forcing the closest packed atoms apart and dramatically decreasing the density. [10]

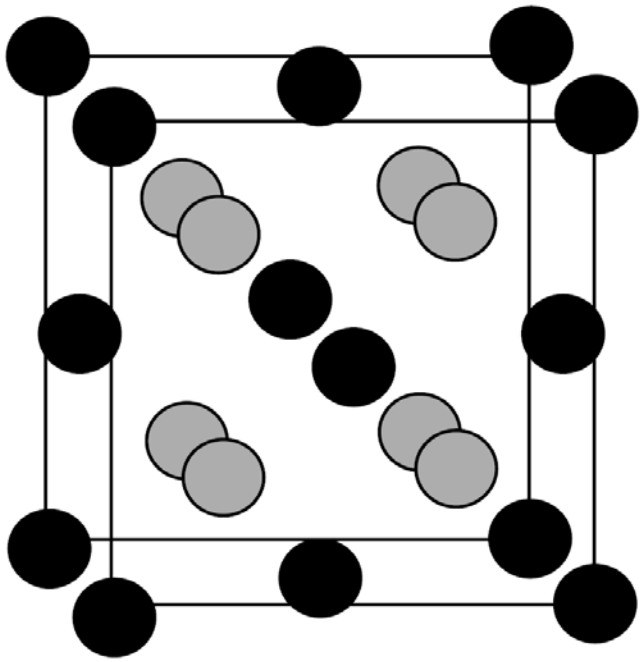

Figure 1.3 Schematic of a fluorite structure unit cell (Black balls represent metal cations, and grey balls represent oxide anions). [3]

Room-temperature ZrO_2 is monoclinic in crystal structure. Yttria is added to stabilize the cubic fluorite structure. Replacing the tetravalent Zr^{4+} ions with trivalent Y^{3+} ions can also create oxygen vacancies. Those created oxygen vacancies can promote oxygen ion diffusion and enhance the oxygen ion conductivity. Similarly trivalent Ga, Sm and La metal oxides have been widely used to increase oxygen ion conductivity of CeO_2. [11,12]

It can be seen from Figure 1.3 that for each oxygen ion, nearest oxygen ions are long <100> directions. <100> directions are therefore supposed to have a largest oxygen ion conductivity because of the shortest diffusion length. Due to lattice match, YSZ has been grown epitaxially on single crystal silicon substrates [13] or (1102) sapphire substrates. [14] Ion beam assisted deposition was also used to achieve film texture. [15,16] Epitaxial CeO_2 films have been successfully grown on silicon, sapphire, and $LaAlO_3$ substrates. [17-19] Both (001)- and (111)-oriented CeO_2 thin films have been grown on amorphous fused silica substrates by ion-beam assisted pulsed laser ablation, using 200 eV Ar^+ ions incident at 55° to the substrate normal. [20] However, in solid oxide fuel cell electrolyte application, YSZ and CeO_2 films are fabricated on porous anodes where epitaxial techniques obviously can not be used. Therefore it is of great importance to find a simple technique to grow highly (100)-oriented YSZ or CeO_2 films.

1.3 P-type Doping of ZnSe Films

Zinc selenide (ZnSe) is a semiconductor with a direct bandgap of about 2.7 eV at room temperature. It is suitable for optical applications using blue or green light, including semiconductor lasers and light-emitting diodes. Extremely high electron concentration was obtained with Cl by molecular beam epitaxy (MBE), where n above $l0^{20}/cm^3$ was obtained with selective doping [21], and above $10^{19}/cm^3$, with non-selective doping. [21] With C1 doping, n above $10^{19}/cm^3$ was also obtained by other researchers, some by MBE [22], others with Hot-Wall Epitaxy. [23] However, like other wide-band-gap semiconductors that typically can not be doped both type, ZnSe is not easy to be doped p-type. Extensive studies have been focused on p-type doping of ZnSe thin films in order to make the devices. Dopants such as As, P, Na, K, Li, Li_3N, and N have been tried for p-type ZnSe doping. Here recent doping efforts are reviewed in terms of dopants.

1.3.1 Phosphorous and Arsenic Doping

Stutius *et al.* have grown Phosphorous-doped ZnSe thin films on (100) GaAs substrates by metalorganic chemical vapor deposition (MOCVD). [24] Edge emission was not observed, and deep emission at 1.97 eV was dominant. Similarly Park *et al.* have tried phosphorous implantation to dope ZnSe. A peak at wavelength of 630 nm (corresponding to 1.97 eV) was dominant in the electroluminescence spectra. However, after the implantation, a p-type layer with low-resistivity was formed. They proposed that shallow acceptor level was formed due to Phosphorous-associated complexes. Yao *et al.* confirmed the coexistence of shallow acceptor and deep acceptor levels occurred in ZnSe using Zn_3P_2 as the source in MBE. [25] Low-temperature PL spectra were carefully studied. It was found that Phosphorous formed a shallow acceptor with an activation energy of 80-92 meV for light Phosphorous doping, and a deep acceptor with an activation energy for heavy doping. Figure 1.4 shows a typical low temperature PL spectrum of Phosphorous-doped ZnSe grown using Zn_3P_2 as the source.

Arsenic is known to be an effective p-type dopant in for ZnTe and CdTe II-VI semiconductors. [26-28] However, there are very few reports on p-type As-doping ZnSe. Similar to phosphorous doping, strong deep-level photoluminescence (PL) peaks were observed in As-doped ZnSe bulk materials, and thin films grown by MOCVD and MBE. [29-32]

Theoretical calculations have been performed to explain the behaviors of ZnSe doping. Chadi and Chang proposed the following model [33]: for dopants such as As and Phosphorous, there are two acceptor states, a metastable effective-mass-like state with a small lattice relaxation, and a deep state with a large relaxation where As has relaxed off the substitutional site and As-Zn bond has been broken. Chadi explained that the mechanism was similar to the DX center in AlGaAs alloys as shown in Figure 1.5. [34] The measured high resistivity of As-doped and Phosphorous-doped ZnSe was due to the DX center. The energy of the deep state was low enough for the relaxation to occur

spontaneously, and the semiconductor was spontaneously "self-compensated". However, Kwak *et al.* also calculated the relaxation using first-principles with a larger supercell. [35] A much smaller relaxation was reported. Kwak *et al.* attributed the failure of effective p-type doping to the occurrence of P_{Zn} antisite defects, which compensated the semiconductor as donors. They also proposed that the deep acceptor level observed previously resulted from the Phosphorous interstitials. The exact reason is still unclear because of limited characterization.

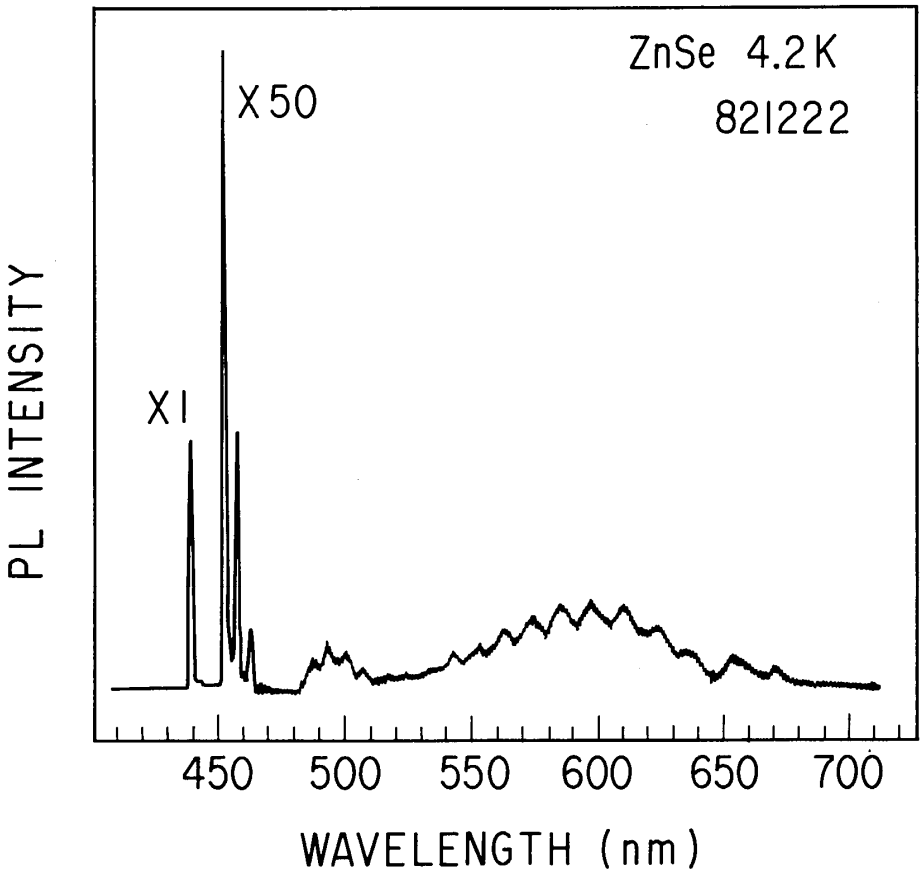

Figure 1.4 Low temperature PL spectrum of P-doped ZnSe grown at 400 °C. [25]

1.3.2 Li, Na, K Doping

Column-I dopants such as Li, Na, and K have been considered to be acceptors in ZnSe. In 1987, Cheng *et al.* successfully grew Li-doped p-type ZnSe thin films by MBE. [36] Haase *et al.* then achieved p-type ZnSe with much lower resistivities by dramatically increasing the Se pressure with a Se to Zn pressure ratio of 8 instead of 2 in Cheng's experiment. [37] Net acceptor concentrations as high as 8×10^{16} cm^{-3} and resistivities as low as 2.9 Ωcm were achieved. Low-temperature PL spectra showed dominant acceptor-bound exciton emission around 2.78 eV. Deep level emission, with a broad peak at 2.19 eV, was 1000 times less than the ABE peak in intensity. However, as a small atom, lithium diffused interstitially in ZnSe. Figure 1.6 shows the measured SIMS depth

profile of Li concentration in the doped sample grown by Haase *et al.* It is seen that Li diffused into a uniform distribution throughout the layer. In the PL spectra, as the Li concentration increased, donor-acceptor-pairs (DAP) peaks increased obviously as a result of self-compensation, as shown in Figure 1.7.

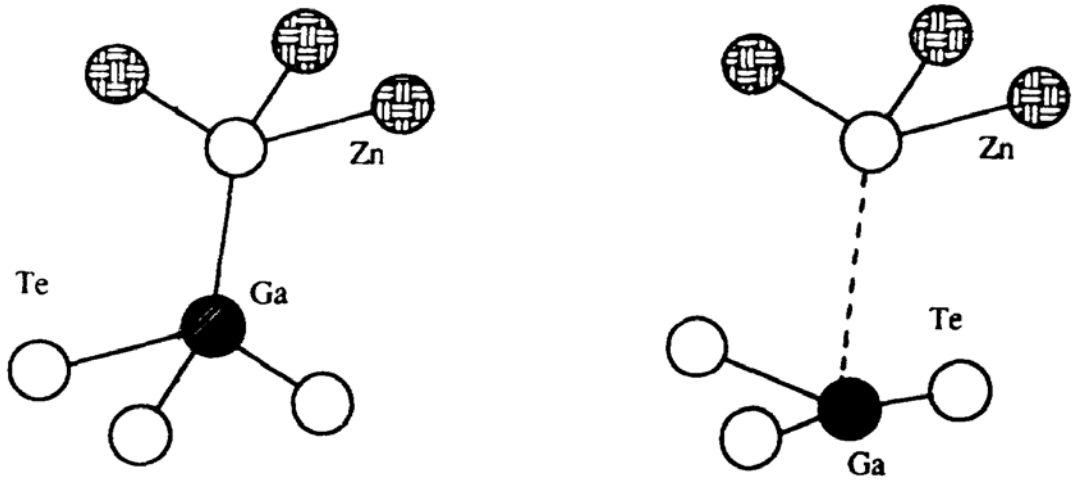

(a) (b)

Figure 1.5 The normal substitutional state of a Ga donor impurity in ZnTe. (b) The localized deep donor DX state, in which the Ga atom has undergone a large displacement. [34]

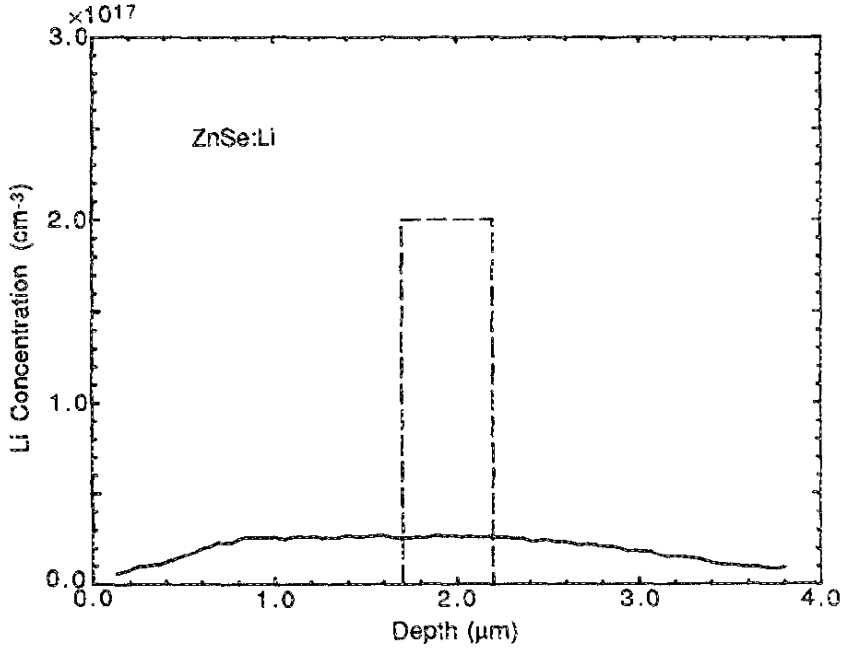

Figure 1.6 SIMS depth profile of the Li concentration after diffusion. The dashed line illustrates the Li profile that would be expected in case of no diffusion. [37]

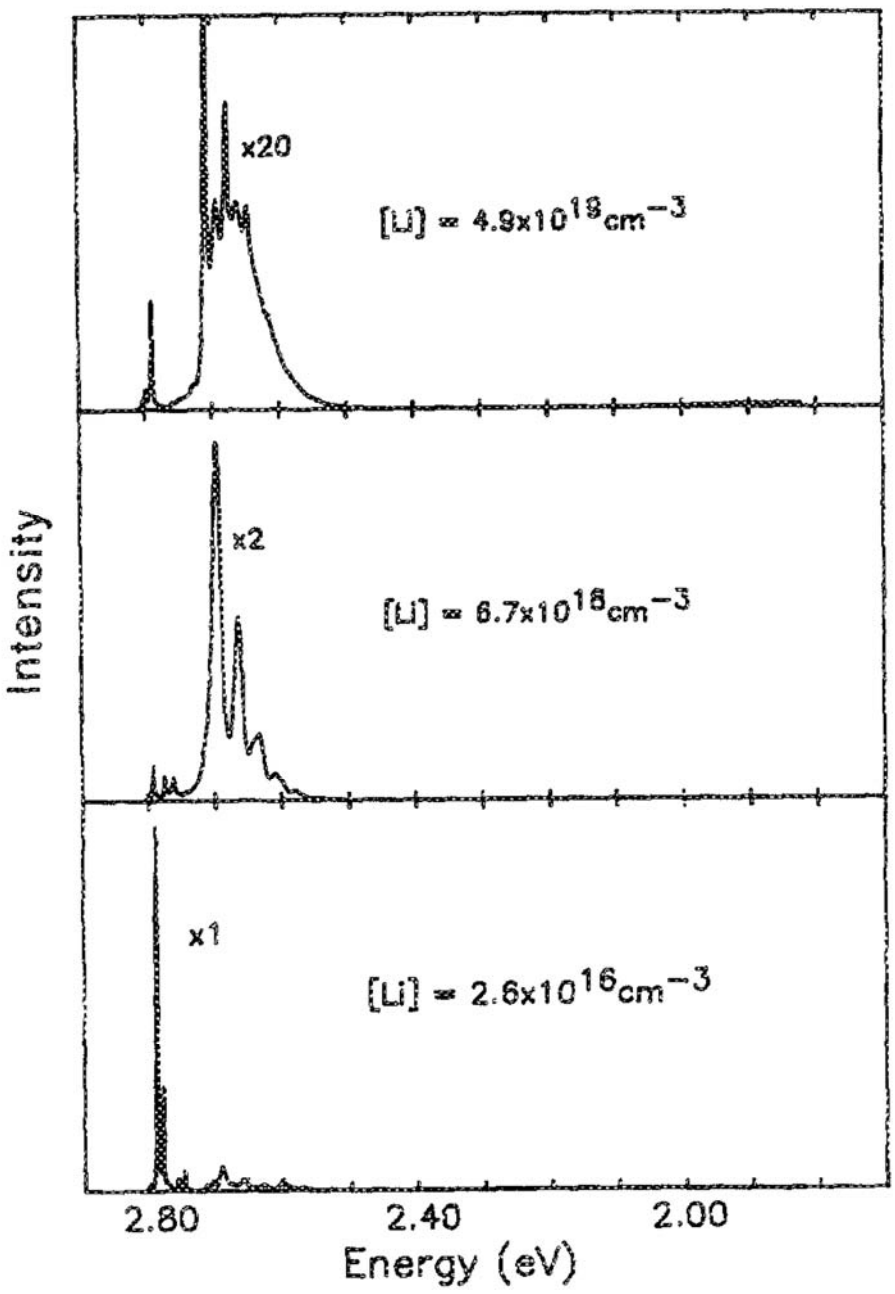

Figure 1.7 Low temperature photoluminescence spectra from samples with different Li concentrations. [37]

Electronically Na and K behave similarly to Li. However, their larger ion size makes them stay uncomfortably on the Zn site. The larger formation energy of the substitution was attributed to this size mismatch by Laks *et al.*. [38] In addition, solubility limit is also an issue. Experimental doping therefore was not successful. [39]

1.3.3 Nitrogen Doping

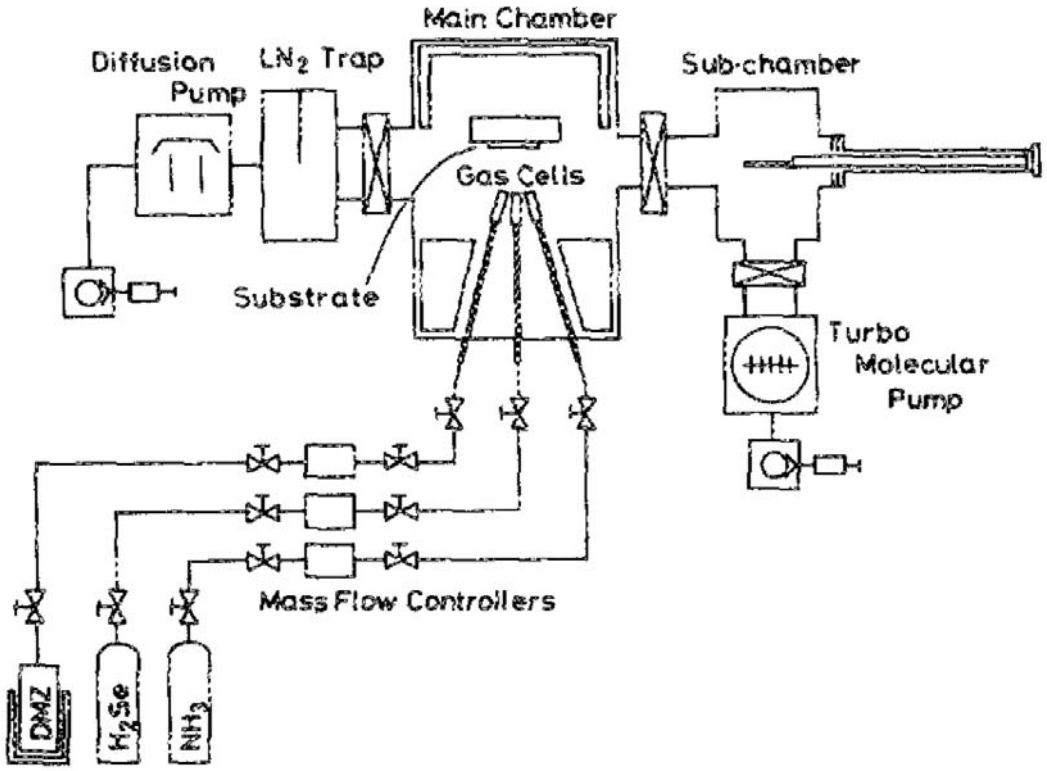

Figure 1.8 Schematic diagram of MOMBE setup. [42]

Nitrogen has produced the most effective p-type doping in ZnSe. In 1985, Park *et al.* tried background gas of N_2 or NH_3 during MBE growth. [40] However, only a small concentration of nitrogen was incorporated as convinced by the dominance of free-exciton emission over acceptor-bound exciton emission in the low-temperature PL spectra. Mitsuyu *et al.* enhanced incorporation of nitrogen by employing ionized N, N_2 and NH_3 gas beams. [41] However, the lowest resistivity achieved was still very high (~ 10^4 Ω•cm). Taike *et al.* used NH_3 as the source of nitrogen impurity in metalorganic molecular beam epitaxy growth (so called "MOMBE") [42], shown in Figure 1.8. The authors claimed that their MOMBE setup was better than the conventional MOCVD for ZnSe film growth since MOMBE could grow high-quality ZnSe films under Zn-rich conditions, thus nitrogen could be easily incorporated. A hole concentration as high as 5×10^{17} cm^{-3} and resistivity as low as 0.57Ω•cm were obtained. In 1990, Park *et al.* firstly used a specially designed free-radical source (FRS) instead of a conventional effusion source in MBE. [43] A high-frequency (13.5 MHz) discharge under conditions of molecular flow provided a flux of atomic nitrogen together with a nondissociated N_2. By adjusting the power of plasma discharge, the atomic nitrogen level was controlled. After optimizing growth conditions in their work later, a net acceptor concentration as high as 1×10^{18} cm^{-3} was achieved. [44] Sooner after, light-emitting diode and laser diode were

obtained using this technique. [43,45,46] Figure 1.9 shows the cross sectional view of a blue-green laser diode reported. [46] An investigation of nitrogen in ZnSe was reported by Walle *et al.* [47] Nitrgen on a substitutional site (N_{Se}) was found to act as a shallow acceptor since the surrounding Zn atoms around N_{Se} undergo a significant inward relaxation. Chadi *et al.* proposed that even if symmetry-lowering relaxation might occur, they would not interfere with the shallow acceptor level. [33]

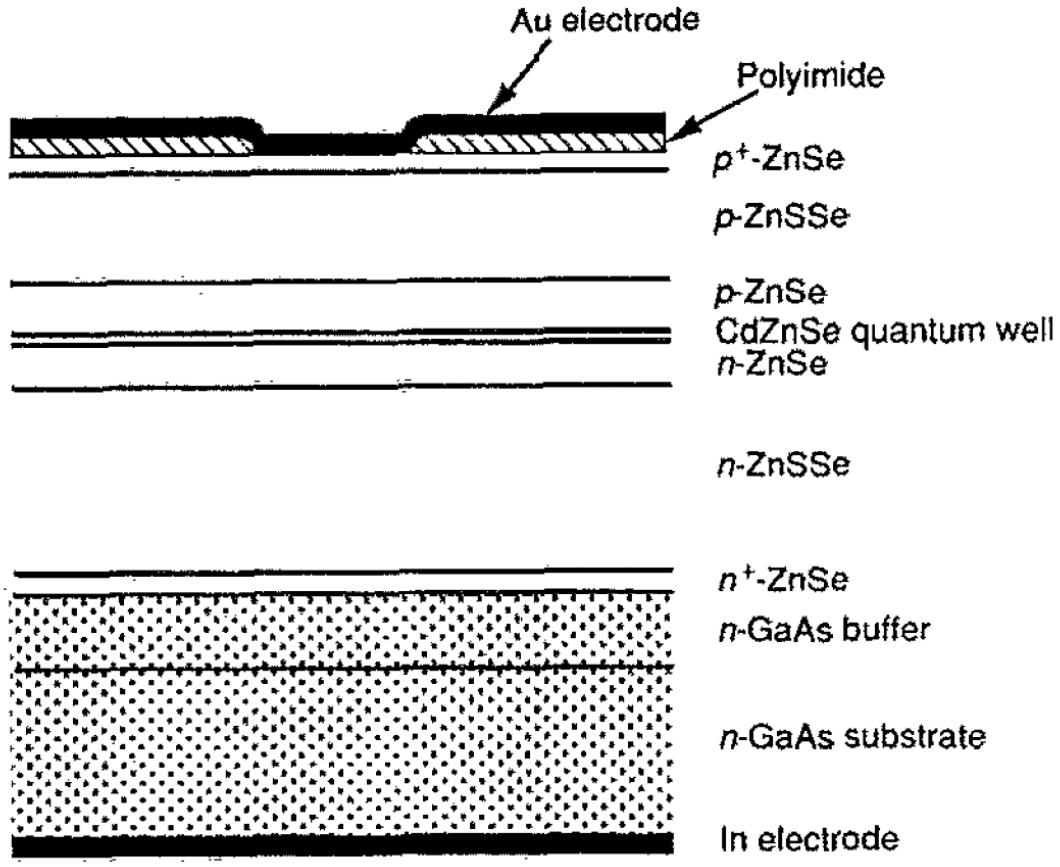

Figure 1.9 Cross-sectional view of a typical blue-green laser diode. [46]

However, just like As and Phorsphous, nitrogen atoms may go to interstitial sites, especially for high doping of nitrogen. [44] A large number of defects has been found to be an issue that can cause degradation. [48] These problems still remain unresolved.

1.3.4 Other doping techniques

Li_3N doping of ZnSe was carried out by Yasuda *et al.* in 1987 with MOCVD growth of ZnSe films. [49] Recently Schulz *et al.* achieved stable acceptor complex with Li_3N indifussion after ZnSe deposition by MBE. [50] However, for both cases, Li diffusion is still a problem as can be expected. Oxygen is an isovalent impurity if it stays in a

substitutional Se lattice site. Its high electronegativity can cause larger charge transfer from the host lattice to O lattice. This can induce holes within the lattice. However the hole concentration induced was so far too low (around 1.2×10^{16} cm^{-3}). [51,52]

1.4 High-throughput Combinatorial Synthesis

To grow thin films using pulsed laser deposition is found to be time-consuming. It usually takes about one day to grow one sample considering pump down, deposition, and cooling down time. It is therefore desirable to grow thin films in a high-throughput way.

In 1995, Xiang *et al.* developed a method that combined thin film deposition and masking techniques for parallel synthesis of spatially addressable libraries of thin film materials. Arrays containing different combinations, stoichiometries, and thickness were generated with a series of binary masks as shown in Figure 1.10. [53] Later they revised the mask design to maximize efficiency of library fabrication. A quaternary masking scheme was developed, which used a series of *n* masks to subdivide the substrate into a series of self-similar patterns of quadrants, as shown in Figure 1.11. [54] Each mask was used up to four sequential depositions and each time the mask was rotated by 90 degrees. This process can produce 4^n different compositions with only $4n$ deposition steps and *n* masks. Therefore, by using the physical shadowing effect of masks, a library of thin films with different compositions or thickness can be fabricated together, which can save much time for loading of samples and pumping down and save the total deposition time as well since the same layer in thin films in this way can be deposited together. The optimization of experimental factors can be greatly accelerated.

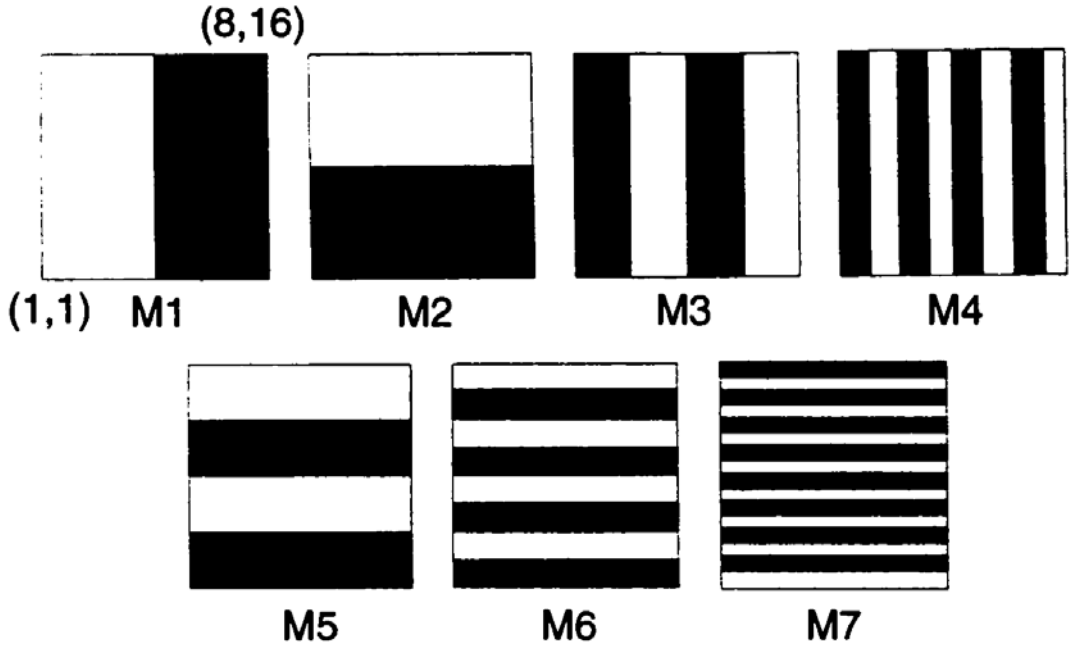

Figure 1.10 Binary masks used for combinatorial synthesis. [53]

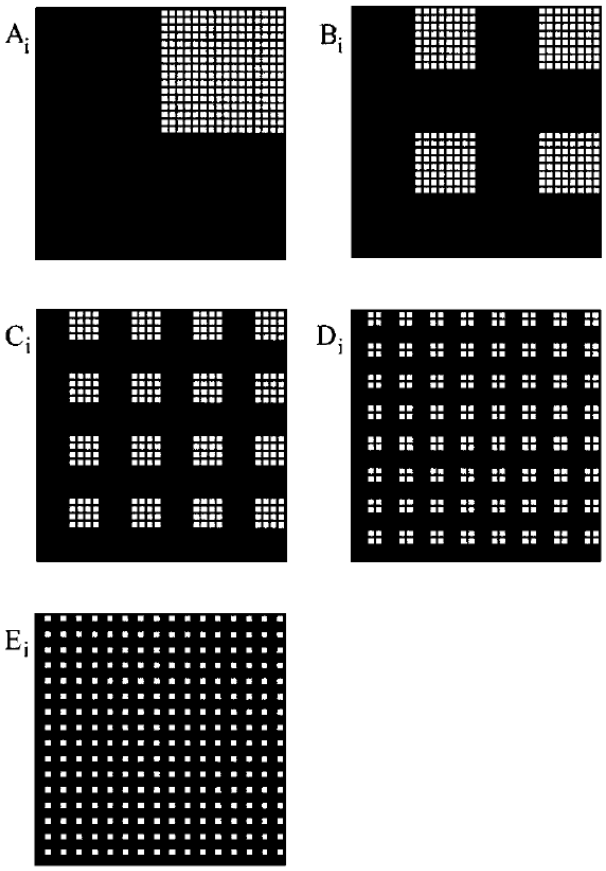

Figure 1.11 Masks for generating a library of materials (A_i, B_i, C_i, D_i, and E_i represent the five different masks). [54]

1.5 Scope of Dissertation

In chapter 2, the deposition yttria-stabilized zirconia (YSZ) and cerium dioxide (CeO_2) thin films at different oxygen pressures is described. Highly (001)-oriented films, which have surfaces that are expected to be forbidden based on Tasker's theoretical calculation of stoichiometric ionic crystals, are obtained. A model considering non-stoichiometry-induced surface relaxation and surface atomic density is proposed to explain the orientation phenomenon observed under oxygen-deficient deposition conditions. The results are compared to previous experimental results of oxide films deposited under similar conditions. Detailed studies of the preferred orientation of these oxygen-deficient ionic crystals are promising for fabrication of highly oriented films in solid oxide fuel cells electrolyte applications.

In chapter 3, undoped, Cu-doped, Se-enriched, Cu_2Se-doped, Ag-doped, Ag_2Se-doped, and nitrogen-doped ZnSe films have been grown on fused quartz substrates by pulsed laser deposition (PLD). Successful heavy p-type doping has been achieved,

which is promising for electrode applications of ZnSe-based devices such as light-emitting diodes. The successful heavy p-type doping of ZnSe films is attributed to substitution of Zn atoms with Cu while limiting selenium-vacancy-associated compensating defects with additional selenium. Nitrogen doping has made ZnSe films more favorable to wurtzite structures. Two newly observed Raman peaks are assigned to N local vibrational modes of hexagonal ZnSe structures. The high resistivity of nitrogen-doped ZnSe films is observed and discussed. This work is of importance to solve doping difficulties and contact problems of wide-bandgap semiconductors.

In chapter 4, batch growth of thin films by pulsed laser deposition has been tried. Using the natural temperature gradient, films with different deposition temperatures have been fabricated together and characterized. The growth of ZnSe films with change of deposition temperatures is analyzed. Multi-plume pulsed laser deposition has been proposed and compared with previous techniques in detail. With directionality of PLD plumes and non-uniformity of PLD films, this system has many advantages and is very promising for efficient materials optimization and exploration.

References:

[1] H. M. Smith and A. F. Turner, Applied Optics **4,** 147 (1965).

[2] D. Dijkkamp, T. Venkatesan, X. D. Wu, S. A. Shaheen, N. Jisrawi, Y. H. Minlee, W. L. McLean, and M. Croft, Applied Physics Letters **51,** 619-621 (1987).

[3] D. P. Norton, Materials Science and Engineering: R: Reports **43,** 139-247 (2004).

[4] D. B. Chrisey and G. K. Hubler, *Pulsed Laser Deposition of Thin Films* (John Wiley & Sons, 1994).

[5] M. N. R. Ashfold, F. Claeyssens, G. M. Fuge, and S. J. Henley, Chemical Society Reviews **33,** 23-31 (2004).

[6] O. Tsuyoshi, S. Keisuke, Y. Takahisa, and L. Mikk, Journal of Applied Physics **103,** 103703 (2008).

[7] G. Koster, G. Rijnders, D. H. A. Blank, and H. Rogalla, Applied Physics Letters **74,** 3729-3731 (1999).

[8] P. R. Willmott and J. R. Huber, Reviews of Modern Physics **72,** 315 (2000).

[9] D. H. Lowndes, D. B. Geohegan, A. A. Puretzky, D. P. Norton, and C. M. Rouleau, Science **273,** 898-903 (1996).

[10] Z. L. Wang and Z. C. Kang, *Functional and Smart Materials: Structural Evolution and Structure Analysis* (Plenum Press, New York, NY, 1998).

[11] M. Mogensen, T. Lindegaard, U. R. Hansen, and G. Mogensen, Journal of the Electrochemical Society **141,** 2122-2128 (1994).

[12] T. Mori, J. Drennan, J. H. Lee, J. G. Li, and T. Ikegami, Solid State Ionics **154,** 461-466 (2002).

[13] D. K. Fork, D. B. Fenner, G. A. N. Connell, J. M. Phillips, and T. H. Geballe, Applied Physics Letters **57,** 1137-1139 (1990).

[14] X. D. Wu, R. E. Muenchausen, N. S. Nogar, A. Pique, R. Edwards, B. Wilkens, T. S. Ravi, D. M. Hwang, and C. Y. Chen, Applied Physics Letters **58,** 304-306 (1991).

[15] C. P. Wang, K. B. Do, M. R. Beasley, T. H. Geballe, and R. H. Hammond, Applied Physics Letters **71,** 2955-2957 (1997).

[16] R. P. Reade, P. Berdahl, R. E. Russo, and S. M. Garrison, Applied Physics Letters **61,** 2231-2233 (1992).

[17] M. W. Denhoff and J. P. McCaffrey, Journal of Applied Physics **70,** 3986-3998 (1991).

[18] T. Inoue, Y. Yamamoto, S. Koyama, S. Suzuki, and Y. Ueda, Applied Physics Letters **56,** 1332-1333 (1990).

[19] X. D. Wu, R. C. Dye, R. E. Muenchausen, S. R. Foltyn, M. Maley, A. D. Rollett, A. R. Garcia, and N. S. Nogar, Applied Physics Letters **58,** 2165-2167 (1991).

[20] S. Zhu, D. H. Lowndes, J. D. Budai, and D. P. Norton, Applied Physics Letters **65,** 2012-2014 (1994).

[21] T. Yao and Z. Zhu, Physica Status Solidi B-Basic Research **187,** 387-392 (1995).

[22] W. Faschinger, S. Ferreira, and H. Sitter, Applied Physics Letters **64,** 2682-2684 (1994).

[23] S. Sakakibara, K. Fujimoto, N. Amano, K. Ishino, A. Ishida, and H. Fujiyasu, Japanese Journal of Applied Physics Part 1-Regular Papers Short Notes & Review Papers **33,** 2008-2014 (1994).

[24] W. Stutius, Journal of Crystal Growth **59,** 1-9 (1982).
[25] T. Yao and Y. Okada, Japanese Journal of Applied Physics Part 1-Regular Papers Short Notes & Review Papers **25,** 821-827 (1986).
[26] M. Ekawa, K. Yasuda, T. Ferid, M. Saji, and A. Tanaka, Journal of Applied Physics **71,** 2669-2674 (1992).
[27] N. C. Giles, K. A. Bowers, R. L. Harper, S. Hwang, and J. F. Schetzina, Journal of Crystal Growth **101,** 67-72 (1990).
[28] F. S. Turcosandroff, M. Brasil, R. E. Nahory, R. J. Martin, Y. Zhang, and B. J. Skromme, Applied Physics Letters **59,** 688-690 (1991).
[29] K. Hingerl, W. Jantsch, P. Juza, M. Lang, H. Sitter, J. Lilja, M. Pessa, D. J. As, and W. Rothemund, Journal of Crystal Growth **117,** 341-347 (1992).
[30] A. R. Reinberg, W. C. Holton, M. Dewit, and R. K. Watts, Physical Review B **3,** 410 (1971).
[31] S. M. Shibli, M. C. Tamargo, B. J. Skromme, S. A. Schwarz, C. L. Schwartz, R. E. Nahory, and R. J. Martin, Journal of Vacuum Science & Technology B **8,** 187-191 (1990).
[32] R. K. Watts, W. C. Holton, and M. Dewit, Physical Review B **3,** 404 (1971).
[33] D. J. Chadi and K. J. Chang, Applied Physics Letters **55,** 575-577 (1989).
[34] D. J. Chadi, Physical Review Letters **72,** 534-537 (1994).
[35] K. W. Kwak, R. D. Kingsmith, and D. Vanderbilt, Physical Review B **48,** 17827-17834 (1993).
[36] H. Cheng, J. M. Depuydt, J. E. Potts, and T. L. Smith, Applied Physics Letters **52,** 147-149 (1988).
[37] M. A. Haase, H. Cheng, J. M. Depuydt, and J. E. Potts, Journal of Applied Physics **67,** 448-452 (1990).
[38] D. B. Laks, C. G. Vandewalle, G. F. Neumark, and S. T. Pantelides, Applied Physics Letters **63,** 1375-1377 (1993).
[39] H. Cheng, J. M. Depuydt, J. E. Potts, and M. A. Haase, Journal of Crystal Growth **95,** 512-516 (1989).
[40] R. M. Park, H. A. Mar, and N. M. Salansky, Journal of Applied Physics **58,** 1047-1049 (1985).
[41] T. Mitsuyu, K. Ohkawa, and O. Yamazaki, Applied Physics Letters **49,** 1348-1350 (1986).
[42] A. Taike, M. Migita, and H. Yamamoto, Applied Physics Letters **56,** 1989-1991 (1990).
[43] R. M. Park, M. B. Troffer, C. M. Rouleau, J. M. Depuydt, and M. A. Haase, Applied Physics Letters **57,** 2127-2129 (1990).
[44] J. Qiu, J. M. Depuydt, H. Cheng, and M. A. Haase, Applied Physics Letters **59,** 2992-2994 (1991).
[45] M. A. Haase, J. Qiu, J. M. Depuydt, and H. Cheng, Ieee Transactions on Electron Devices **38,** 2708-2708 (1991).
[46] M. A. Haase, J. Qiu, J. M. Depuydt, and H. Cheng, Applied Physics Letters **59,** 1272-1274 (1991).
[47] C. G. Vandewalle and P. E. Blochl, Physical Review B **47,** 4244-4255 (1993).
[48] S. Guha, J. M. Depuydt, M. A. Haase, J. Qiu, and H. Cheng, Applied Physics Letters **63,** 3107-3109 (1993).

[49] T. Yasuda, I. Mitsuishi, and H. Kukimoto, Applied Physics Letters **52,** 57-59 (1988).
[50] O. Schulz, M. Strassburg, T. Rissom, U. W. Pohl, D. Bimberg, M. Klude, and D. Hommel, Applied Physics Letters **81,** 4916-4918 (2002).
[51] K. Akimoto, T. Miyajima, and Y. Mori, Physical Review B **39,** 3138-3144 (1989).
[52] K. Akimoto, T. Miyajima, and Y. Mori, Japanese Journal of Applied Physics Part 2-Letters **28,** L531-L534 (1989).
[53] X. D. Xiang, X. D. Sun, G. Briceno, Y. L. Lou, K. A. Wang, H. Y. Chang, W. G. Wallacefreedman, S. W. Chen, and P. G. Schultz, Science **268,** 1738-1740 (1995).
[54] J. Wang, Y. Yoo, C. Gao, I. Takeuchi, X. Sun, H. Chang, X. D. Xiang, and P. G. Schultz, Science **279,** 1712-1714 (1998).

Chapter 2
Growth of Oxide Films for Solid Oxide Fuel Cell Applications

2.1 Introduction

Solid oxide fuel cells (SOFCs) are clean power-generation devices that convert chemical energy directly into electricity while producing little noise and pollution. [1] Yttria-stabilized zirconia (YSZ) and cerium oxide (CeO_2) have attracted great interest for SOFC electrolyte applications owing to its high oxygen ion conductivity and low electron conductivity. Important to SOFC performance, the mechanical, electrical, and electrochemical properties of YSZ films depend on their crystal orientation, and prior research has achieved epitaxial or textured YSZ film growth. [2-6] For instance, Norton and Yamada *et al.* used (001) silicon single crystal substrates and rolling-assisted biaxially textured substrates to grow the c-axis oriented cubic YSZ films. [3,6] Iijima and Sonnenberg *et al.* obtained biaxially aligned YSZ films with (220), (111) or (001) orientation normal to the substrate by ion-beam-assisted deposition. [2,5]

However, for current techniques, the most widely used anodes are porous materials such as Ni-YSZ cermets [7], Cu-based YSZ cermets [8], and samaria-doped ceria-NiO powders. [9] These porous anodes cannot be used for epitaxial growth of YSZ and CeO_2 electrolytes. Ion-beam-assisted deposition has the disadvantages of possible incorporation of bombarding gas, complex processing, low film growth rate, and excessive residual compressive film stress, etc. Therefore, it is of great interest to find an easy and effective method to achieve highly oriented YSZ thin films as SOFC electrolytes.

In 1979, Tasker investigated the stability of stoichiometric ionic crystal surfaces in terms of electrostatic energy. [10] This study classified ionic crystal surfaces into three types, whereby Type 3, which describes the physical scenario where the dipole moment is perpendicular to the surface, should be forbidden. While stoichiometric oxide films have been studied extensively, there are very few reports on the growth of these ionic materials under oxygen-deficient deposition conditions.

In this work, YSZ and CeO_2 thin films were prepared on stainless steel, glass, and fused quartz substrates by pulsed laser deposition method in oxygen-deficient environments and their structural properties are compared to those of films grown in oxygen-rich environments. It is found that the orientation of YSZ films is sensitive to the oxygen pressure during deposition. Highly oriented thin films, whose surfaces are categorized as forbidden in terms of Tasker's analysis, have been obtained. These results are compared to previous reports on ITO, SnO_2, and NiO thin films grown under similar conditions.

2.2 Experimental Details

A Lambda Physik (LPX 210i) pulsed excimer laser with a wavelength of 248 nm was used as the excitation source for the ablation of YSZ (with 5wt% Y_2O_3) and CeO_2 pellets (cold-pressed from 99.99% purity powders). [11] The laser beam, oriented at an incidence angle of 45° to the target normal, was focused onto the YSZ or CeO_2 target in a vacuum chamber with a fluence of 2.4 J/cm^2 and at a pulse frequency of 10 Hz. Substrates were mounted on a resistively heated block facing the target and at a distance of 4.5 cm. Stainless steel, glass and fused quartz substrates were cleaned consecutively in an ultrasonic bath of acetone, methanol and deionized water for 15 minutes. Before deposition, the chamber was pumped overnight to a base pressure of $\sim 2 \times 10^{-6}$ Torr, and during deposition oxygen or nitrogen gas flowed into the chamber through a mass flow controller to establish various background pressures as discussed in the text. YSZ were deposited at 60 °C, 300 °C, and 600 °C. CeO_2 thin films were deposited at room temperature. Crystal structures and morphology of the films were analyzed by X-ray diffraction (XRD) using Cu Kα radiation and scanning electron microscopy (SEM).

2.3 Results and Discussions

Figure 2.1 shows the XRD patterns of YSZ films grown on stainless steel substrates at 60 °C and different oxygen pressures (0.1 mTorr, 1 mTorr, 10 mTorr, 100 mTorr, 500 mTorr and 1000 mTorr) after 15000 deposition pulses. The base pressure was 2×10^{-6} Torr. The peaks are analyzed and tetragonal, monoclinic and amorphous YSZ phases are observed. In this analysis, for simplicity, all the indices of YSZ and CeO_2 are labeled using cubic notation. As seen from the figure, the growth of YSZ films is critically dependent on the oxygen pressure during the deposition. At the oxygen pressure of 10 mTorr and below, the YSZ films crystallize very well and only the tetragonal YSZ phase is observed. Note that for films deposited at 1 mTorr and 10 mTorr, the (002) peaks are very sharp and strong. The full widths at half maximum (FWHM) of (002) peaks are about 0.4°. As the oxygen pressure increases, the YSZ films become amorphous. The critical pressure above which amorphous phase occurs is about 100 mTorr. The occurrence of the amorphous phase at high oxygen pressure may be explained by poor crystallization because of reduced energy of the deposited species. The oxygen gas molecules tend to impede the expansion of the laser-produced vapor plume. This interaction acts to decrease the plume energy, thus reducing the average energy of the ions deposited onto the substrate. This explanation is consistent with the results of films deposited at 300 °C and 600 °C, as shown in Figures 2.2 and 2.3. As the substrate temperature increases, amorphous phase formation occurs at higher oxygen pressures, since higher temperature offers higher energy for crystallization. At 300 °C, the critical pressure becomes 500 mTorr while at 600 °C no obvious amorphous phase is observed below 1000 mTorr.

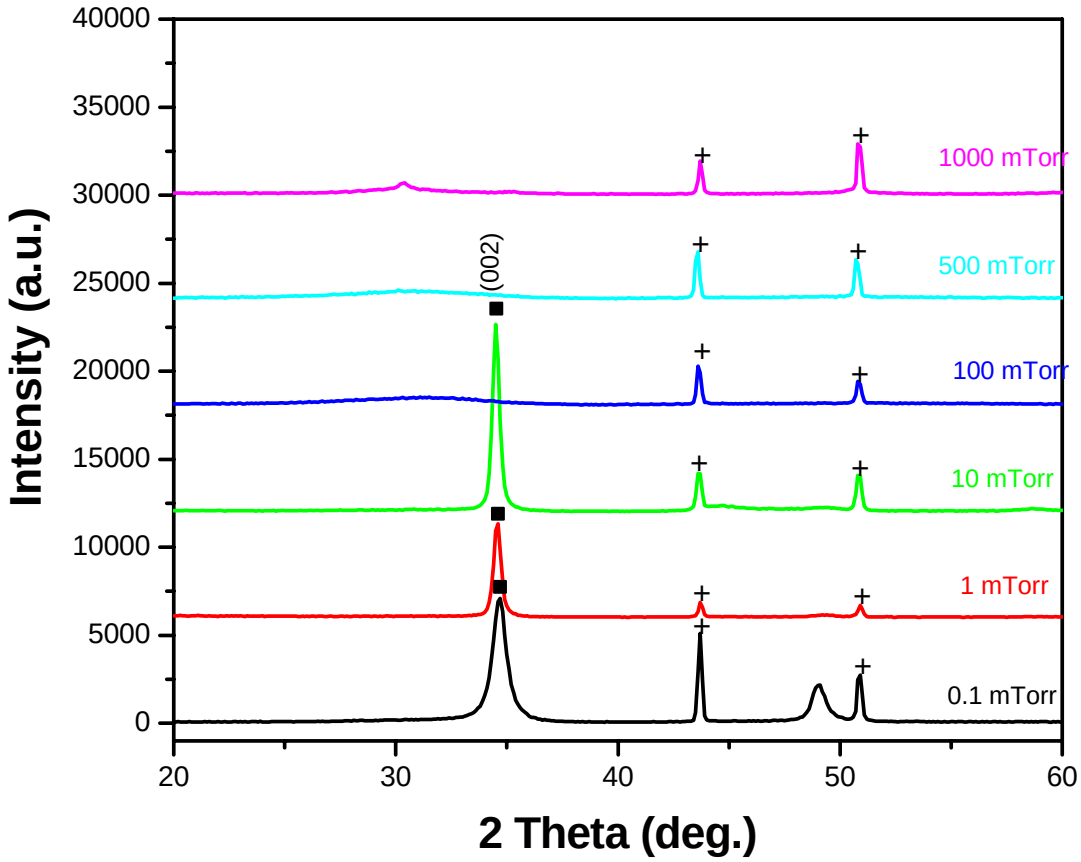

Figure 2.1 XRD patterns of YSZ films deposited at 60 °C and different oxygen pressures on stainless steel substrates. (In all the XRD patterns, squares, circles and crosses are used representing peaks of the tetragonal YSZ, monoclinic YSZ and the stainless steel substrate, respectively.)

From the three XRD figures at different temperatures, it is seen that (001) orientation predominantly occurs in low oxygen pressure regions. Except for the 60 °C depositions, in which the amorphous phase occurs at pressures higher than 100 mTorr, (111) peaks become dominant as the oxygen pressure increases to intermediate pressures. At 300 °C, 100 mTorr and 600 °C, 500 mTorr, YSZ films become mainly (111)-oriented.

A similar transition in film preferred orientation from (001) to (111) is observed for CeO_2 thin films when deposited at higher oxygen pressures. Figure 2.4 shows XRD patterns of CeO_2 films deposited on stainless steel substrates at room temperature. Highly (001)-oriented CeO_2 films were obtained in vacuum conditions (base pressure: 2×10^{-6} Torr), as shown in Figure 2.4(a). As oxygen pressure is increased to 8 mTorr, the (002) peak becomes much weaker while the (111) peak increases in intensity. This

reveals a transition of texture from (001) to (111) when ambient oxygen pressures are increased.

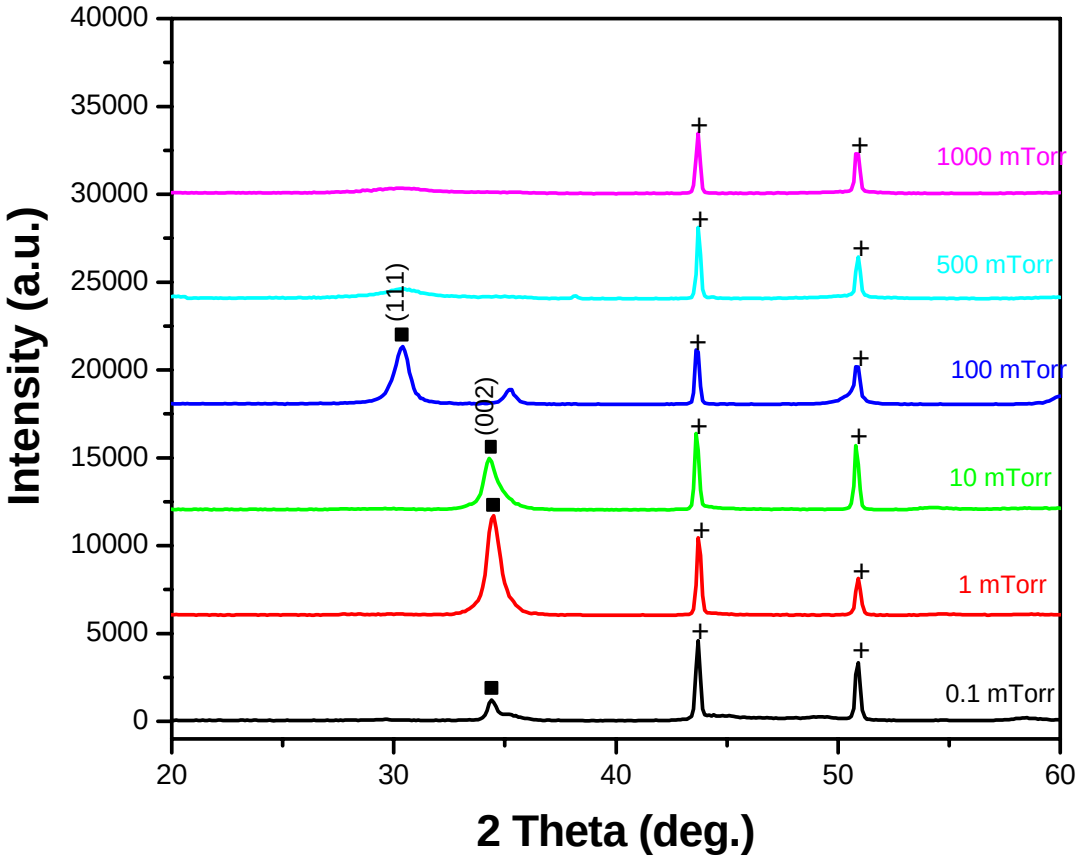

Figure 2.2 XRD patterns of YSZ films deposited at 300 °C and different oxygen pressures on stainless steel substrates.

Collision with ambient gas molecules is known to decrease the kinetic energy of deposited species (ions, atoms, and radicals). The attenuation of species' energy could potentially influence the observed film texture of samples in this study. In order to address this concern, CeO_2 thin films were deposited in nitrogen under identical conditions. As shown in Figure 2.4(c), CeO_2 films deposited at 8 mTorr N_2 possess very similar relative peak intensities to those deposited in vacuum. Similar film orientations have been obtained for films deposited in argon ambient gas (data not shown). This suggests that the change of texture is not due to the kinetic energy of deposition species, but results from the oxygen content in the deposition chamber instead.

Knowing that substrates can affect film texture, films were also deposited onto glass and fused quartz substrate to determine the influence of substrates on film orientation.

Figure 2.5 shows the XRD pattern of a YSZ thin film deposited on glass at 1 mTorr oxygen pressure. This pattern indicates very similar orientation as those films deposited on stainless steel substrates under the same conditions. It is observed experimentally that as film thickness increases (to more than ~500 nm), the film texture is not dependent on the nature of the substrate.

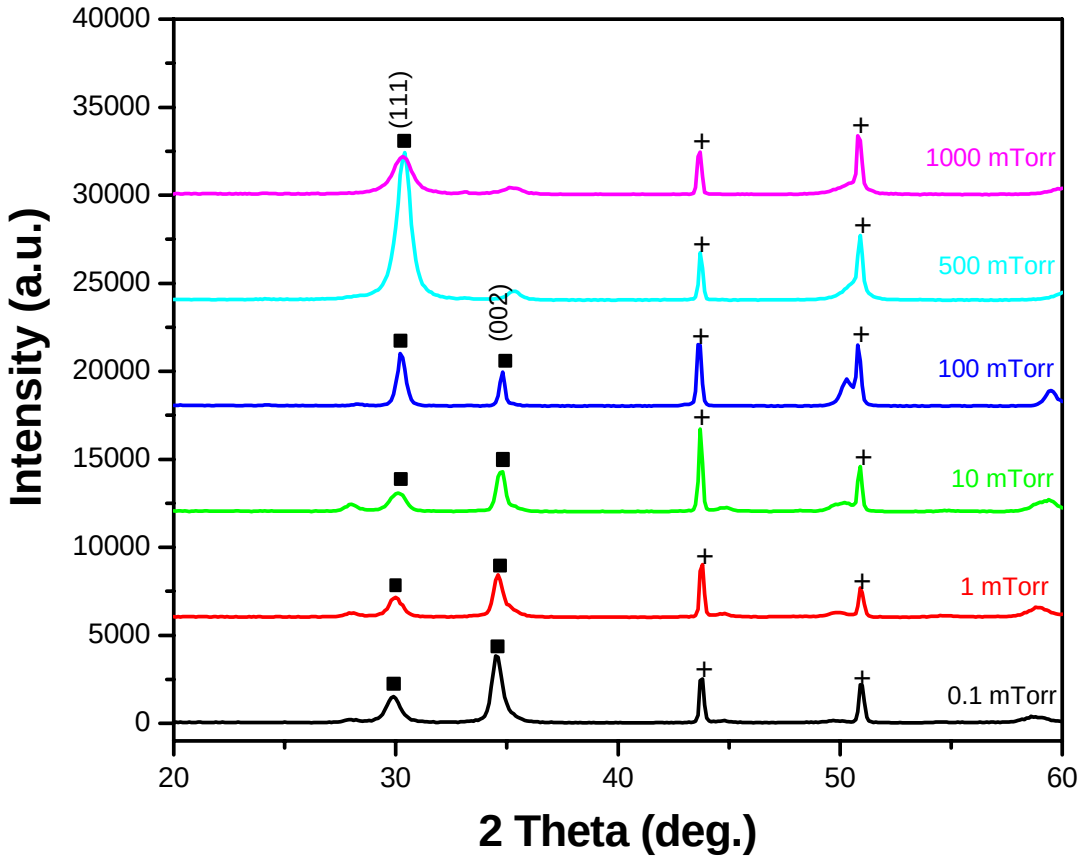

Figure 2.3 XRD patterns of YSZ films deposited at 600 °C and different oxygen pressures on stainless steel substrates.

It has been reported previously that strain can influence film orientation.[12-14] However, since in this study CeO_2 films were grown at room temperature, strain effects caused by the differing thermal expansion coefficients of films and substrates should be very small. Both compressive and tensile stresses should exist in YSZ films since substrates with thermal expansion coefficients either larger or smaller than that of the film have been used (thermal expansion coefficients: CeO_2: $\sim 9.5 \times 10^{-6}$ K^{-1}; YSZ: $\sim 8.6 \times 10^{-6}$ K^{-1}; stainless steel: $\sim 17.3 \times 10^{-6}$ K^{-1}; fused quartz: $\sim 0.59 \times 10^{-6}$ K^{-1}). As described previously, no dependence of film orientation on substrate selection was

observed. Therefore, it is suggested to be unlikely that film orientations as presented above are influenced by strain.

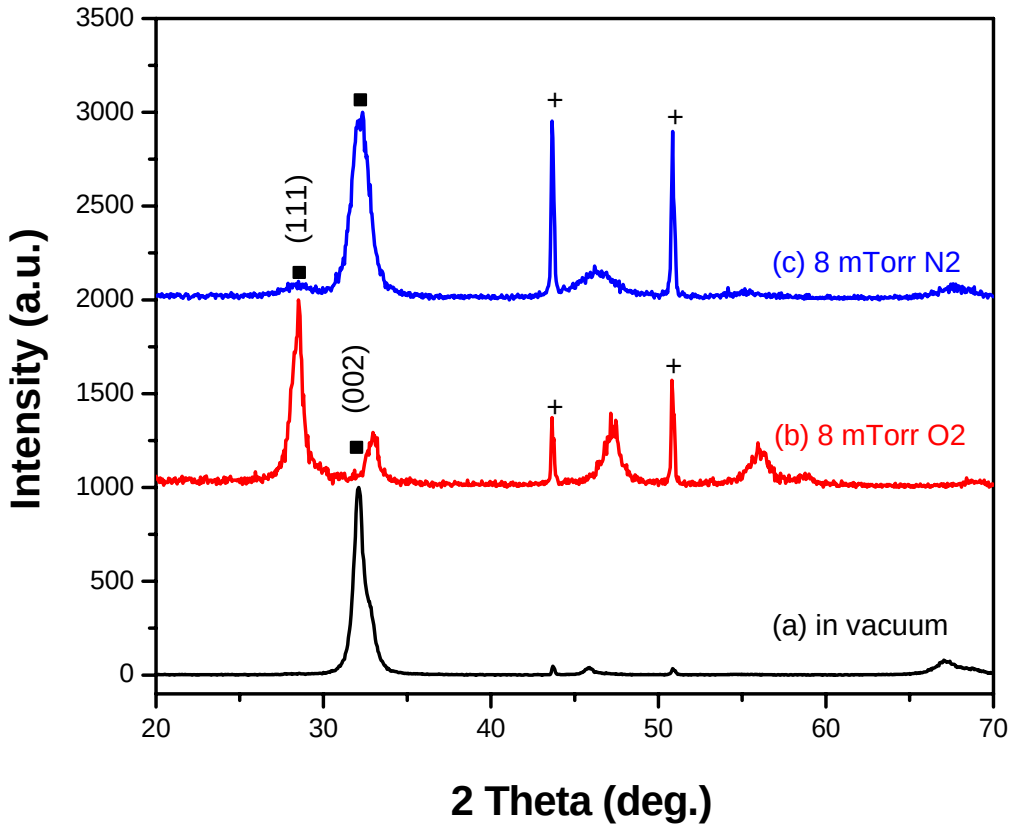

Figure 2.4 XRD patterns of CeO_2 thin films deposited on stainless steel substrates (a) in vacuum, (b) at 8 mTorr O_2, and (c) at 8 mTorr N_2.

As is well-known, the texture of films can be thermodynamically or kinetically driven. Here we attribute the highly (001) orientation to be determined by the surface energy. Note that in the (111) planes of fluorite structures both anions and cations are arranged hexagonally. If the film surface develops with this atomic arrangement, the material has the greatest bonds in the surface plane and least dangling bonds out of plane. The formation of this surface minimizes surface free energy and therefore typically represents the thermodynamically favorable atomic configuration. Figure 2.6 shows side views of (111) and (001) planes. Normal to the growth direction of [111] or [001], (111) and (001) planes are stacked with charged atomic planes of anions or cations. According to Tasker's calculation[10], the stacking sequence of (111) planes with a terminating anion plane is Type 2, which has no dipole perpendicular to the surface. However, for (001) planes, the stacking sequence is Type 3, with alternating positively and negatively charged atomic planes, which results in dipoles normal to the surface. This surface is expected to be forbidden as a result of its infinite surface energy. Therefore, considering

the density of dangling bonds and corresponding stacking sequence, the (111) orientation is more likely to occur while the (001) orientation should be forbidden.

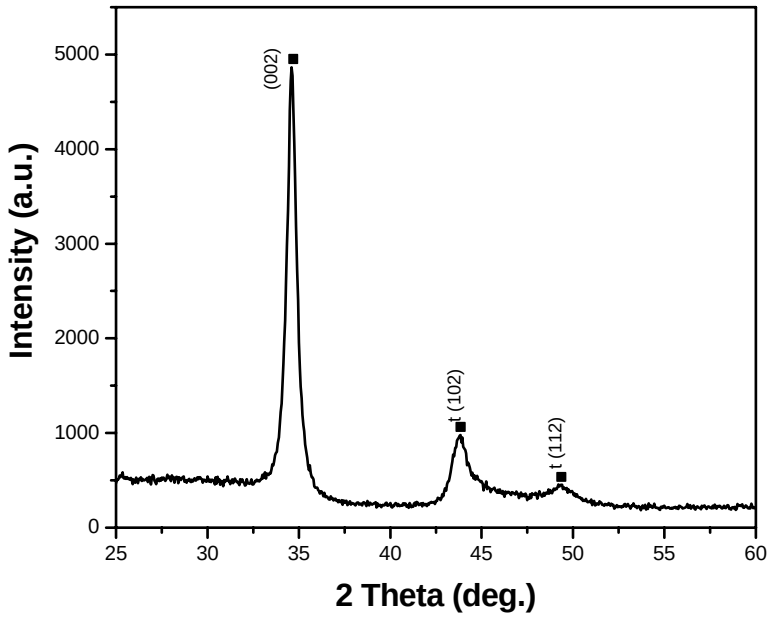

Figure 2.5 XRD pattern of a YSZ film deposited at 60 °C and 1 mTorr oxygen pressure on glass.

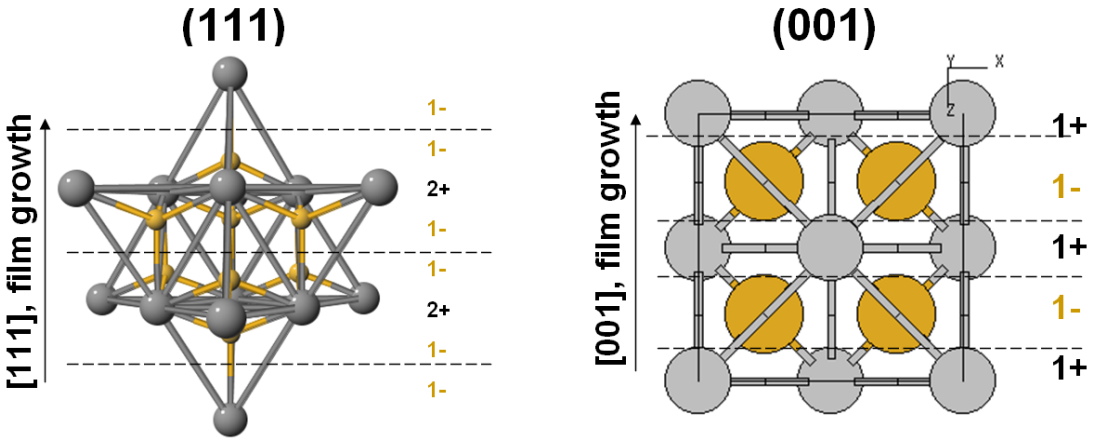

Figure 2.6 Schematic of side views of (a) (111) planes without dipole perpendicular to the surface (b) (001) planes with dipole perpendicular to the surface. Oxygen ions are in yellow.

However, in this report thin films with fluorite structure are experimentally observed to possess the (001) orientation. Note that the discussion above has assumed that the

surface is stoichiometric and contains no relaxation or reconstruction. However, surface reconstruction and relaxation may play an important role in affecting the surface energy and thus determining the film texture. It is proposed below that the occurrence of (001) texture is due to oxygen-vacancy-induced surface reconstruction and relaxation.

Herman and Norenberg et. al. have proposed several models of (001) surface reconstructions.[15,16] However, all of these models are based on the assumption that there is a significant amount of oxygen vacancies on the surface. As an example, if the surface oxygen concentration is reduced by 50%, the (001) stacking sequence can be regarded as $\frac{1}{2}$ ML of oxygen—1 ML of cerium—$\frac{1}{2}$ ML of oxygen…, in which case there will be no dipole moments along the growth direction. Therefore, films grown under oxygen-deficient conditions can promote these oxygen-vacancy-induced surface reconstructions, reduce the surface energy, and make the (001) orientation more energetically favorable.

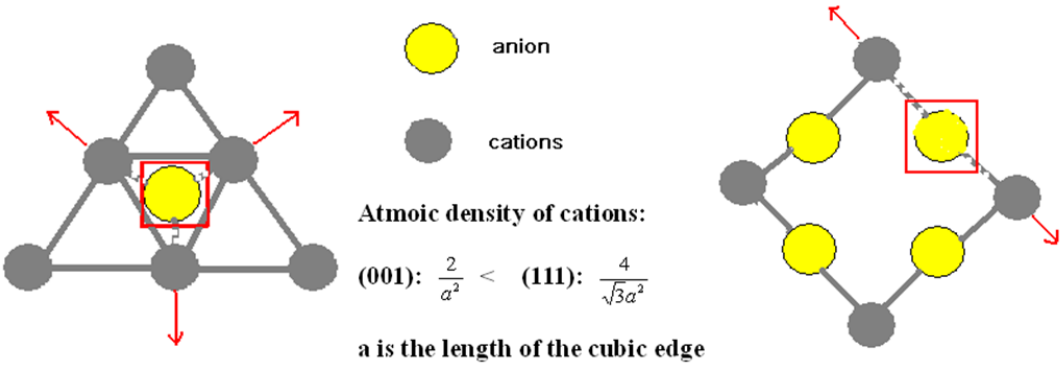

Figure 2.7 Schematic of top-down views of (a) (111) planes with an oxygen anion on the top surface, and (b) (001) planes with oxygen anions on the top. Yellow circles represent oxygen anions.

Oxygen-vacancy-induced surface relaxation also plays an important role. Figure 2.7 shows top-view schematics of (111) and (001) surfaces with oxygen planes as terminating planes. In a stoichiometric crystal, the oxygen ion in the (111) plane is expected to remain in a position where it attracts the three adjacent cations. Similarly, in the (001) plane, the oxygen ion is expected to attract the two adjacent cations in the unit cell. However, when films are deposited under oxygen-deficient conditions, an oxygen vacancy may be present in place of the oxygen anion. Without the attracting oxygen anion, the three aforementioned cations in the (111) plane will repel each other. A simple calculation indicates that the number density of cations in (111) is larger than that in (001), indicating that cations in (001) might be easier to move and relax. As surface relaxation can release electrostatic energy and result in a decrease in surface energy, it is therefore energetically favorable for the (001) orientation to occur at low oxygen deposition pressures. This conclusion of stronger relaxation on (001) surface is consistent

with previous molecular dynamics simulations, density functional theory (DFT) calculations, and first principle calculations.[17-19]

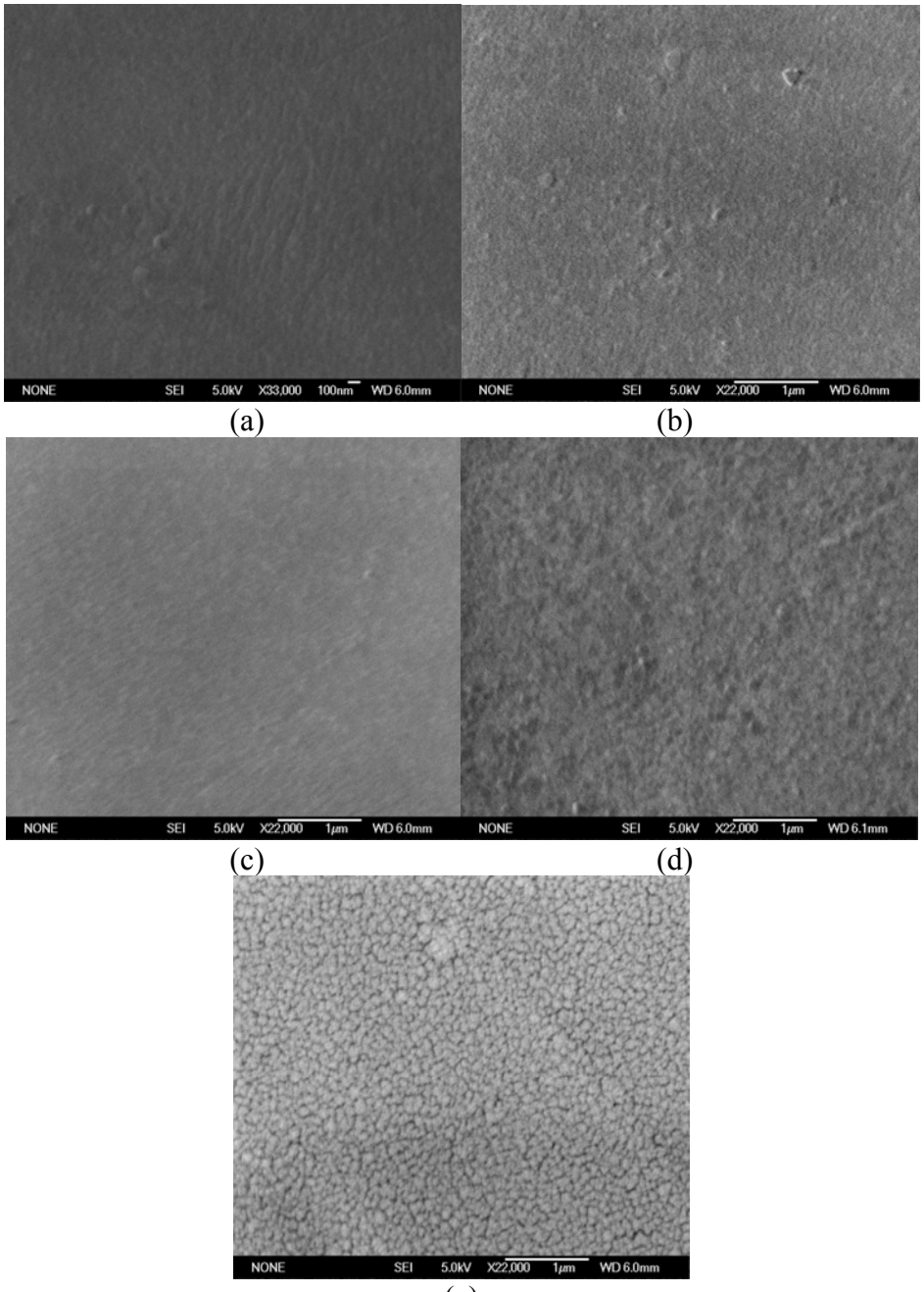

Figure 2.8 SEM images of YSZ thin films grown at 300 °C and at an oxygen ambient pressure of (a) 0.1 mTorr, (b) 1 mTorr, (c) 10 mTorr, (d) 100 mTorr and (e) 1000 mTorr.

It is interesting to note that there are several accounts of oxygen-deficient films exhibiting forbidden Type 3 surfaces, which posses lower atomic number densities in

their exposed surfaces. This includes oxygen-deficient ITO, SnO_2, and NiO.[20-23] Thilakan *et al.*. reported that oxygen deficient ITO thin films grown by reactive thermal deposition were highly (004)-textured, while (222) texture was preferred at higher oxygen pressures.[23] SnO_2 has shown a significantly preferred (001) orientation when deposited in oxygen-deficient environments.[21] When grown by radio-frequency magnetron sputtering, NiO films have been reported to prefer (111) orientation when deposited with a limited oxygen supply, and (002) orientation with increased oxygen supply.[20] In each of these ionic crystals the forbidden surface planes [(004) plane of ITO, (001) plane of SnO_2 and (111) plane of NiO], Type 3 in terms of stacking sequence, are observed when films are deposited in oxygen-deficient environments. Note that all the forbidden planes in these studies are those with atomic densities lower than the planes that have lowest surface energy in stoichiometric crystals [(222) plane of ITO, (110) plane of SnO_2 and (100) plane of NiO]. It is suggested that when these films are deposited in oxygen deficient environments, surface relaxation may play an important role in determining the thermodynamically favorable film texture. In these oxygen-deficient films, the orientation may be determined by planes whose low atomic densities facilitate enhanced surface relaxation, which results in a decreased surface energy.

Surface morphology of YSZ thin films was analyzed by scanning electron microscopy (SEM) as shown in Figures 2.8 (a)-(e). For films grown at an oxygen ambient pressure of 100 mTorr or below, films are dense. However, films grown at 1000 mTorr as shown in Figure 2.8(e) are porous.

Some of the films grown on glass were examined by optical transmission spectroscopy; the results will be reported elsewhere. However, we note here that broadband optical absorption in the visible spectrum is found, an absorption that is larger in samples prepared at lower oxygen pressures. This behavior supports our expectation that films grown at lower oxygen pressures indeed are more oxygen deficient, which is due to an process of oxygen uptake from the chamber gas.

2.4 Summary

In summary, the fabrication of highly oriented YSZ and CeO_2 thin films with (002) surfaces, which should be forbidden because of nonzero surface dipole in stoichiometric fluorite ionic crystals, has been presented. Oxygen-vacancy-induced surface reconstruction and relaxation are proposed. This analysis is consistent with previous experimental results of ITO, SnO_2 and NiO thin films grown under similar oxygen-deficient conditions.

References:

[1] N. Q. Minh, Journal of the American Ceramic Society **76,** 563-588 (1993).
[2] Y. Iijima, M. Hosaka, N. Tanabe, N. Sadakata, T. Saitoh, O. Kohno, and K. Takeda, Journal of Materials Research **12,** 2913-2923 (1997).
[3] D. P. Norton, A. Goyal, J. D. Budai, D. K. Christen, D. M. Kroeger, E. D. Specht, Q. He, B. Saffian, M. Paranthaman, C. E. Klabunde, D. F. Lee, B. C. Sales, and F. A. List, Science **274,** 755-757 (1996).
[4] R. P. Reade, P. Berdahl, R. E. Russo, and S. M. Garrison, Applied Physics Letters **61,** 2231-2233 (1992).
[5] N. Sonnenberg, A. S. Longo, M. J. Cima, B. P. Chang, K. G. Ressler, P. C. McIntyre, and Y. P. Liu, Journal of Applied Physics **74,** 1027-1034 (1993).
[6] T. Yamada, N. Wakiya, K. Shinozaki, and N. Mizutani, Applied Physics Letters **83,** 4815-4817 (2003).
[7] S. deSouza, S. J. Visco, and L. C. DeJonghe, Solid State Ionics **98,** 57-61 (1997).
[8] S. McIntosh, J. M. Vohs, and R. J. Gorte, Electrochimica Acta **47,** 3815-3821 (2002).
[9] R. Maric, S. Ohara, T. Fukui, H. Yoshida, M. Nishimura, T. Inagaki, and K. Miura, Journal of the Electrochemical Society **146,** 2006-2010 (1999).
[10] P. W. Tasker, Journal of Physics C-Solid State Physics **12,** 4977-4984 (1979).
[11] X. Zhang, P. Berdahl, A. Klini, C. Fotakis, and S. S. Mao, Applied Physics A-Materials Science & Processing **91,** 407-410 (2008).
[12] D. R. McKenzie, Y. Yin, W. D. McFall, and N. H. Hoang, Journal of Physics-Condensed Matter **8,** 5883-5890 (1996).
[13] U. C. Oh and J. H. Je, Journal of Applied Physics **74,** 1692-1696 (1993).
[14] J. M. Zhang, K. W. Xu, and V. Ji, Applied Surface Science **180,** 1-5 (2001).
[15] G. S. Herman, Physical Review B **59,** 14899 (1999).
[16] H. Norenberg and J. H. Harding, Surface Science **477,** 17-24 (2001).
[17] M. Baudin, M. Wick, and K. Hermansson, Surface Science **468,** 51-61 (2000).
[18] M. Nolan, S. Grigoleit, D. C. Sayle, S. C. Parker, and G. W. Watson, Surface Science **576,** 217-229 (2005).
[19] N. V. Skorodumova, M. Baudin, and K. Hermansson, Physical Review B **69,** 075401 (2004).
[20] C. Hao-Long and Y. Yao-Sheng, Thin Solid Films **516,** 5590-5596 (2008).
[21] Y. Matsushima, K. Maeda, and T. Suzuki, Journal of the Ceramic Society of Japan **116,** 989-993 (2008).
[22] M. Nisha, S. Anusha, A. Antony, R. Manoj, and M. K. Jayaraj, Applied Surface Science **252,** 1430-1435 (2005).
[23] P. Thilakan and J. Kumar, Vacuum **48,** 463-466 (1997).

Chapter 3
Heavy P-type Doping of ZnSe Films for Light-Emitting Diode Electrode Applications

3.1 Introduction

Zinc selenide (ZnSe), a semiconductor with a direct bandgap of about 2.7 eV at room temperature, is widely studied for potential application in optoelectronic devices including semiconductor lasers and light-emitting diodes. The successful p-type doping of ZnSe by incorporation of nitrogen radicals during molecular beam epitaxy (MBE) has led to the demonstration of blue-green lasers and light-emitting diodes based on ZnSe active layers. [1-4] However, because the highest hole concentration reported is limited to about 10^{18} cm^{-3} [3], fabrication of low-resistance ohmic contacts to p-type ZnSe is still a formidable challenge. All metals, including Au and Pt, produce appreciable energy barriers (more than 1.0 eV) when deposited on p-type ZnSe layer. [5] Graded Zn(Se,Te) heterostructures have been incorporated as an efficient injector of holes for devices. [6,7] However, due to the large lattice mismatch between ZnSe and ZnTe, ZnSe-based lasers tend to degrade due to defects originating from the Zn(Se,Te) heterostructure. [8] Graded BeTe/ZnSe contacts have also been reported. [9,10] The formation of a BeSe interfacial layer, which has a large lattice mismatch with the ZnSe layer, also causes the BeTe/ZnSe interface to degrade rapidly. [11]

In this chapter, undoped, Cu-doped, Se-enriched, and Cu_2Se-doped, Ag-doped, nitrogen-doped ZnSe films were grown on fused quartz substrates by pulsed laser deposition and characterized by X-ray diffraction (XRD), scanning electron microscopy (SEM), Rutherford backscattering spectrometry (RBS), particle-induced X-ray emission (PIXE), optical transmission/reflection spectroscopy, Hall effect, and I-V measurements. It is demonstrated that a small amount of Cu_2Se (~2 mol%) can significantly improve the (111) texturing of ZnSe films and promote grain growth while causing a very small amount of lattice constant change ($\leq$ 0.143%). P-type ZnSe thin films with hole concentrations up to $\sim 1.1 \times 10^{19}$ cm^{-3} (compared with previous reports of $\sim 1 \times 10^{18}$ cm^{-3}) and resistivities of ~0.098 Ohm•cm (compared with previous reports of ~0.75 Ohm•cm) have been obtained. [3,4] Linear I-V curves are achieved as well. The results have shown that Cu_2Se-doping is an effective means to achieve heavily p-type ZnSe films that can be used as ohmic contact layers for ZnSe-based devices.

3.2 Experimental Details

The pulsed laser deposition system used for this work has been described previously in detail. In order to increase film uniformity and to avoid paste-related contaminations, fused quartz or GaAs substrates with a stainless steel mask were affixed to a home-built rotatable mounting plate. Before deposition the chamber was pumped down to a base pressure of 2×10^{-7} Torr, and the substrate was heated to 400 °C. Deposition occurred by selective ablation of commercially available ZnSe, Cu_2Se, and Cu, Ag targets with purity of 99.99%. The focused laser spot ablated the dopant target (Cu, Ag, or Cu_2Se) and ZnSe target alternatively at 5 Hz pulse repetition rate. A 16 mol%-Se-enriched ZnSe target was used for Se-enriched ZnSe film deposition. After 2.5 hours' deposition at 400 °C, the films were annealed in-situ for 1.5 hours and then cooled down. Crystal structures and morphology of the films were analyzed by X-ray diffraction (XRD) using Cu Kα radiation and SEM. Optical transmission and reflection spectroscopy measurements were performed with a FilmTek 3000PAR SE thin film metrology system, operating in transmission and reflection mode. After XRD and optical measurements, gold electrodes were sputtered onto edges of the samples. Annealing was performed in nitrogen ambient at 200 °C for 30 minutes. Hall effect measurements were performed using an Ecopia HMS-3000 system with a magnetic field of 0.6 T. Film thickness was measured by a Tencor AS500 profilometer. The copper compositions were determined by Rutherford backscattering (RBS) and particle-induced X-ray emission (PIXE) using a 3 MeV alpha ion beam.

For nitrogen doping, nitrogen gas was introduced into the deposition chamber after pumping down to base pressure. An ISA Groupe Horiba microscope Raman system with an internal He-Ne (632nm) 10 mW laser was used. Detail of the raman spectrum measurement has been described previously. [12]

3.3 Results and Discussions

3.3.1 Doping with Cu, Se, Cu_2Se

Figure 3.1(a) shows typical XRD patterns of undoped (sample 22), Cu-doped (samples 31 and 51, with PIXE-determined Cu compositions up to 3 mol%), Se-enriched (sample 401, with 16 mol% Se enrichment), and Cu_2Se-doped ZnSe films (samples 105, 107, and 101 with PIXE determined Cu compositions of 3 mol%, 4 mol% and 15 mol%, respectively). The samples are listed in Table 1. It can be seen that the films are grown in the cubic phase with mainly (111), (200), and (311) orientations. While single phase ZnSe is observed for samples 105 and 107, a weak peak of (111) Cu_2Se is detected for sample 101, suggesting that phase separation occurs for this sample when the Cu composition (15 mol%) exceeds the miscibility limit. It is interesting to note that the crystallinity and the (111) texturing of the films have significantly improved when a small amount of Cu_2Se (samples 105 and 107) is added to the ZnSe film.

Higher resolution XRD measurements of the ZnSe (111) diffraction peak from the various samples are shown in Figure 3.1(b). It is found that (111) peaks of undoped

(sample 22), Cu-doped (samples 31 and 51) and Se-enriched (sample 401) ZnSe films are weak and broad with full widths at half maximum (FWHM) of ~0.25°. For Cu_2Se doped samples 105 and 107 (3% and 4% Cu), (111) peaks become much stronger and sharper with widths of ~0.12°. A rough estimation of grain size has been made using Debye-Scherrer equation after subtracting the instrumental broadening effect. It is estimated that grain sizes are increased from 60 nm to 400 nm after adding in Cu_2Se. Compared with those of the undoped ZnSe film, peaks of Cu-doped ZnSe films shift to smaller angles, indicating an increase in the lattice constant, while peaks of Cu_2Se-doped ZnSe shift to larger angles, indicating a decrease of lattice constant. The shift of peak position is very small (~ 0.04°), and corresponds to a 0.143% lattice constant decrease. Such a small lattice change is beneficial for minimizing dopant-induced strains in ZnSe films.

Table 3.1 A list of the ZnSe samples and their structural and electrical properties.

Sample No.	**Dopant**	**Cu content (mol %)**	**Grain Size (nm)**	**Bandgap (eV)**	**Hall effect**		
					Type	**Conc. (/cm^3)**	**Mobility** (cm^2/V·s)
22	Undoped	--	100	2.626	--	--	--
31	Cu	< 3	120	2.614	--	--	--
51	Cu	3	130	2.609	--	--	--
401	Se	--	150	2.685	--	--	--
105	Cu_2Se	3	380	2.640	p	6.94×10^{18}	5.95
107	Cu_2Se	4	380	2.643	p	1.1×10^{19}	5.9
101	Cu_2Se	15	500	2.622	p	7.44×10^{20}	0.66

The grain growth induced by Cu_2Se doping is observable in microscopy analyses. Figure 3.2(a) shows a typical SEM image of undoped ZnSe surface morphology (sample 22). Grain sizes in this image are estimated to be about 100 nm. However, after adding in Cu_2Se, we observe a dramatic increase in the grain size to about 380 nm as shown in Figure 3.2(b). This result is consistent with the XRD analysis discussed above. In Figure 3.2(b), it is seen that grains become tight and faceted on the surface. The significant grain growth after adding Cu_2Se could possibly be explained by liquid-phase assisted grain growth.[13,14]

Absorption coefficients shown in Figure 3.3 are calculated from the equation $\alpha = -\frac{1}{d}\ln\left(\frac{T}{1-R}\right)$, where T is transmittance, R is reflectance, and d is film thickness, which is determined directly from profilometry. The film thicknesses range from 1.2 μm to 2.1 μm. Bandgaps are calculated by extrapolation of $(\alpha h\nu)^2$ near the band edges. It is found that except for sample 101, which shows evidence of phase separation as explained above, all the other samples (samples 22, 51, 401, 105 and 107) show dramatic absorption increases at the band edge energies. Bandgaps of samples 22, 51, 401, 105,

and 107, as listed in Table 1, are 2.626 eV, 2.609 eV, 2.685 eV, 2.640 eV, and 2.643 eV, respectively. The bandgaps are consistent with previous reports of ZnSe. [15,16] The optical bandgap is decreased by ~17 meV with Cu doping, increased by ~14 meV with Cu_2Se doping, and increased by ~59 meV by Se enrichment.

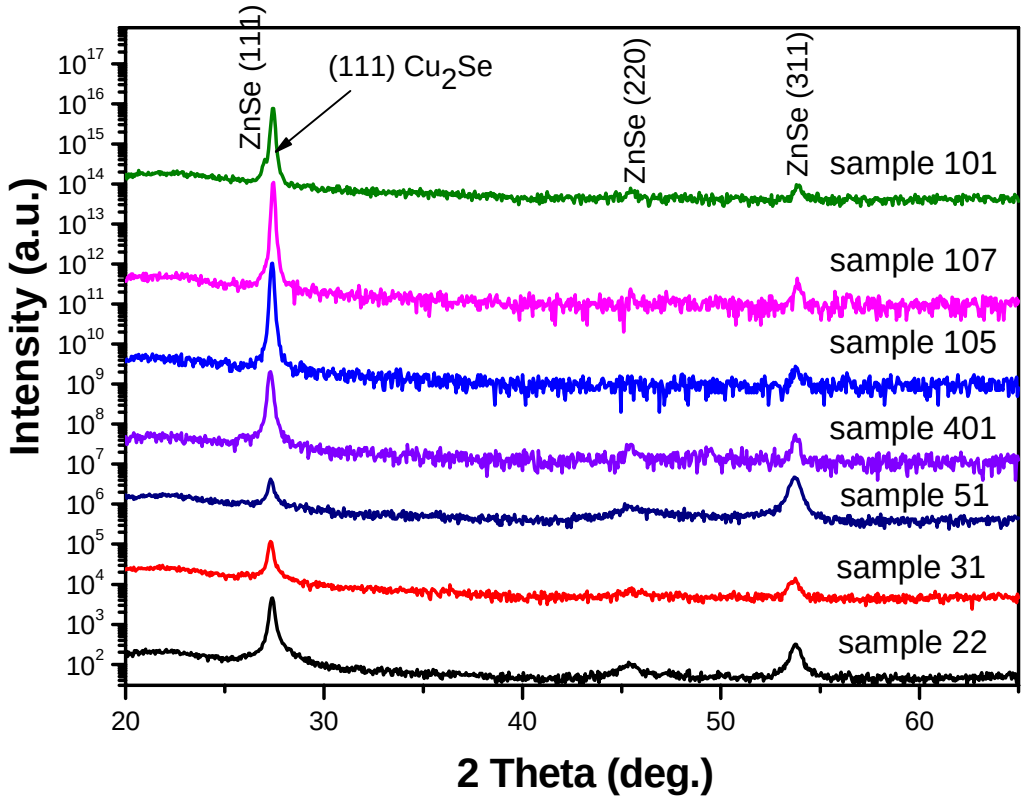

Figure 3.1(a) XRD patterns of undoped (sample 22), Cu-doped (samples 31 and 51), Se-enriched (sample 401), Cu_2Se-doped (samples 105, 107, and 101) ZnSe thin films. The plots are shifted for better view.

The electrical properties were analyzed by Hall effect measurements. It was determined that both the 16 mol%-Se-enriched ZnSe film and Cu-doped ZnSe films are highly resistant. Hall effect measurement results of Cu_2Se-doped ZnSe films are also listed in Table 1. These results indicate the films are highly p-type. Sample 107 shows a hole concentration of 1.1×10^{19} cm^{-3}, which is about one order of magnitude larger than previously reported value of 1×10^{18} cm^{-3}. [6,16,17] The resistivity of sample 107 is 0.098 Ohm•cm, also much lower than previously reported 0.75 Ohm•cm. Since the depletion layer thickness is inversely proportional to $\sqrt{N}$ (N is the carrier concentration), tunneling effects are more significant at such high hole concentrations. A typical I-V curve of a sample without using gold electrodes is shown in Figure 3.4. The curve is linear, demonstrating an excellent ohmic contact established between the measurement probes and sample surface.

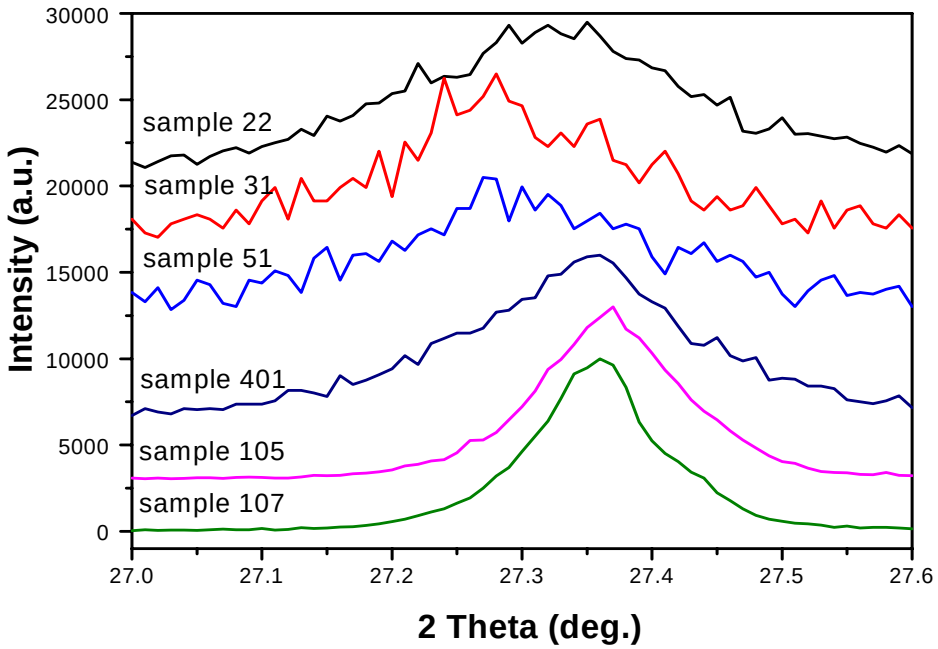

Figure 3.1(b) Small region XRD patterns of undoped (sample 22), Cu-doped (samples 31 and 51), Se-enriched (sample 401), and Cu_2Se-doped (samples 105 and 107) ZnSe thin films.

It has been proposed previously that compensation in p-type ZnSe films is mainly due to complexes associated with selenium vacancies such as V_{Se}-Zn-N_{Se}.[18,19] Doping ZnSe films with Cu can further increase the anion deficiency. By introducing selenium and thus reducing selenium vacancies, this type of compensation is minimized. In addition, it is known that Cu atoms act as donors in interstitial sites and as acceptors when substituting Zn^{2+} (Cu_{Zn}). Adding selenium could increase zinc vacancies and assist Cu atoms to enter acceptor Zn sublattice. This scenario explains the possible mechanisms involved in the increased p-type doping of ZnSe films using Cu_2Se.

The observed lattice constant decrease in Cu_2Se-doped films presented above may provide evidence for a reduction in selenium vacancy concentration. As shown above, Cu-doping increases the lattice constant while Se enrichment and Cu_2Se doping decrease it. Resulting from the repulsion among cations, the selenium vacancies in a unit cell can increase the lattice constant. It is possible that doping with Cu_2Se reduces the overall Se vacancy concentration as compared with Cu doping, which results in a decrease in lattice constant.

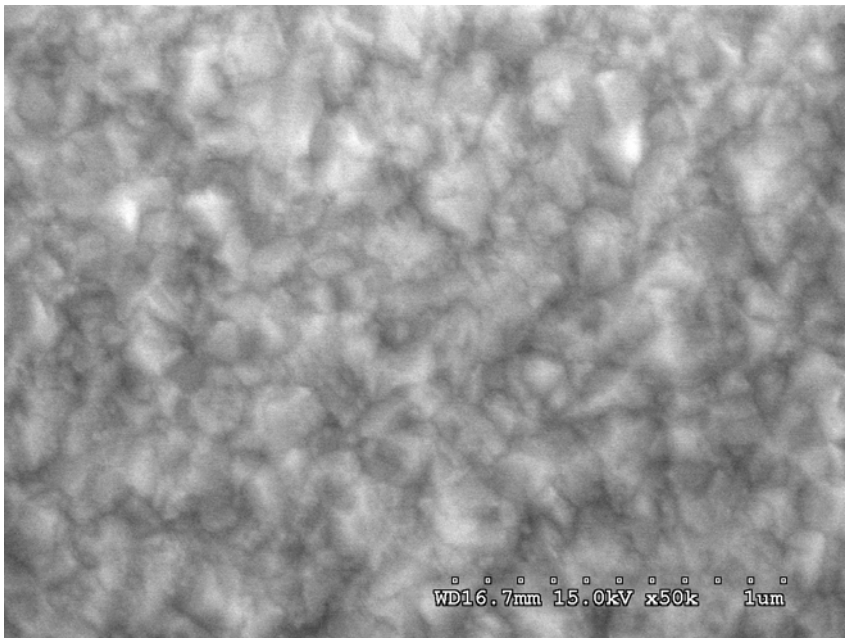

Figure 3.2(a) A SEM image of undoped ZnSe film surface (sample 22).

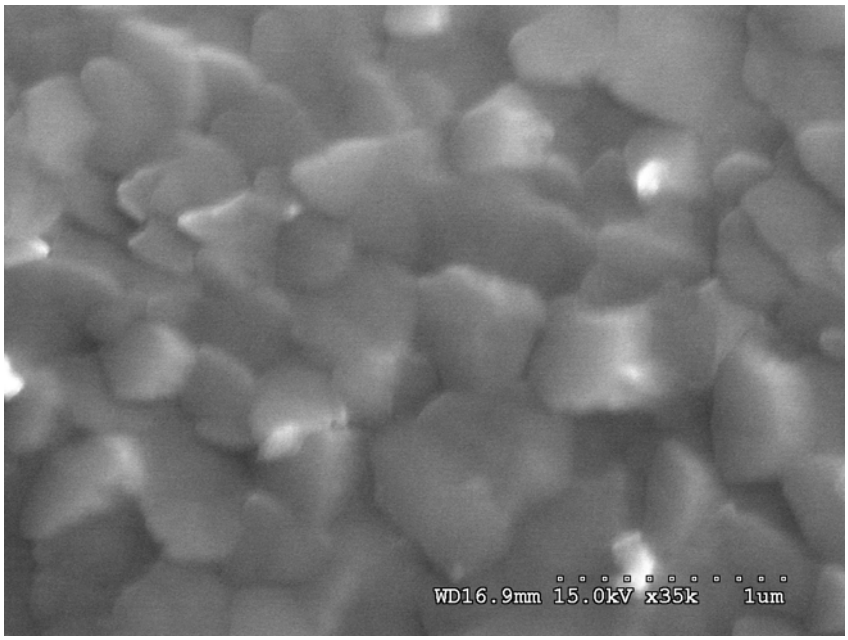

Figure 3.2(b) A typical SEM image of Cu_2Se-doped ZnSe film surface (sample 105).

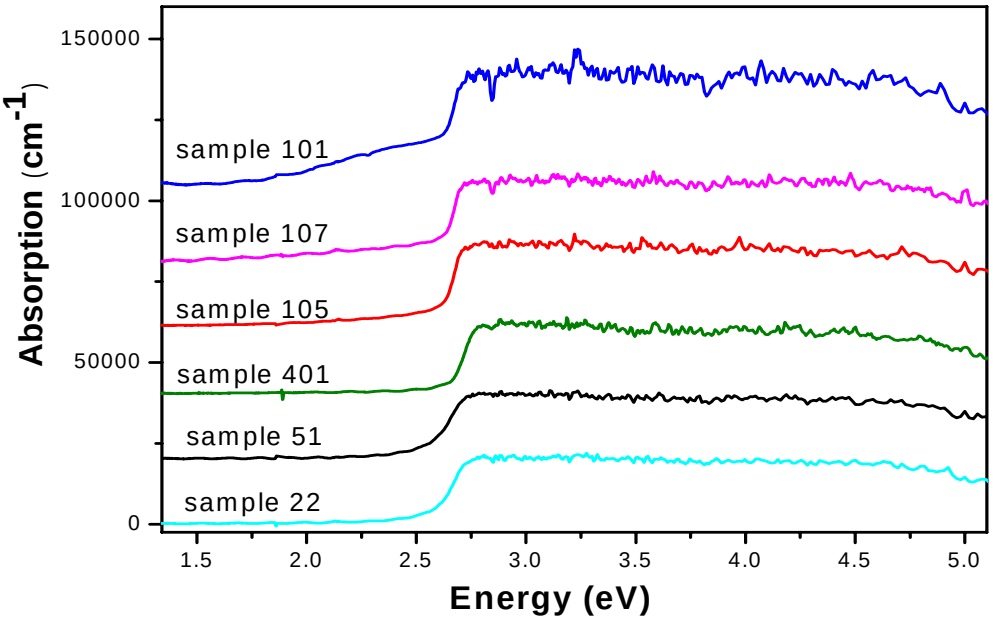

Figure 3.3 Absorption coefficients of undoped (sample 22), Cu-doped (sample 51), Se-enriched (sample 401), Cu_2Se-doped (samples 105, 107, and 101) ZnSe films. The plots are shifted by 20000 cm^{-1} for better view.

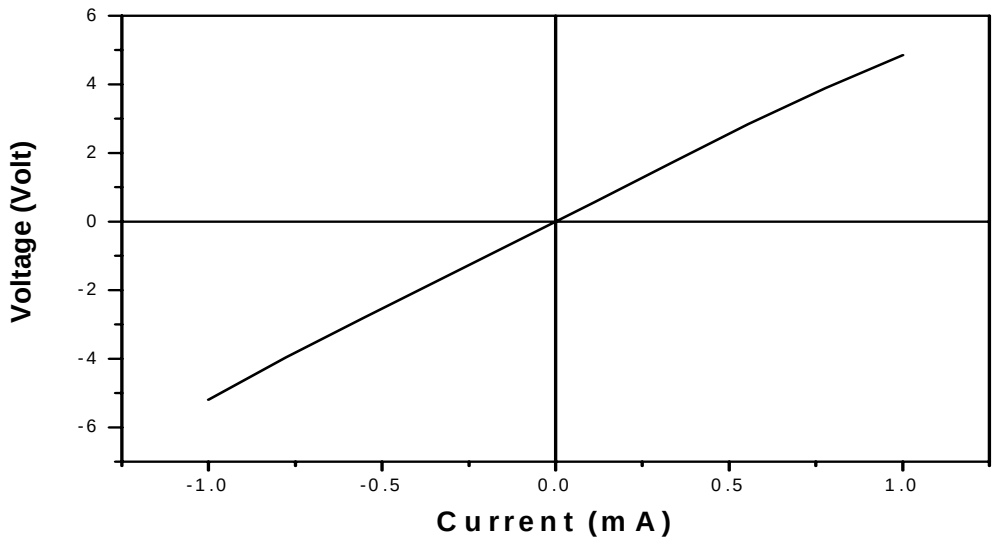

Figure 3.4 A typical I-V curve of Cu_2Se-doped ZnSe films.

3.3.2 Doping with Ag, Ag_2Se

Although different amounts of Ag have been tried, Ag-doped ZnSe samples are all non-conductive. XRD pattern and Transmittance and Reflectance spectra are shown in Figure 3.5(b) and 3.8(d). Using the same method as discussed above, the bandgap is determined to be 2.612 eV. The bandgap is decreased just like Cu-doping. The (111) peak shits to a lower angle and lattice constant increases as shown in Figure 3.7(c). However, although Ag doping is very similar to Cu doping in terms of XRD and optical results, none of the samples deposited using Ag, Ag + Se targets are conductive. This might be due to a higher ionization energy of Ag_{Zn} in Ag doping. [20]

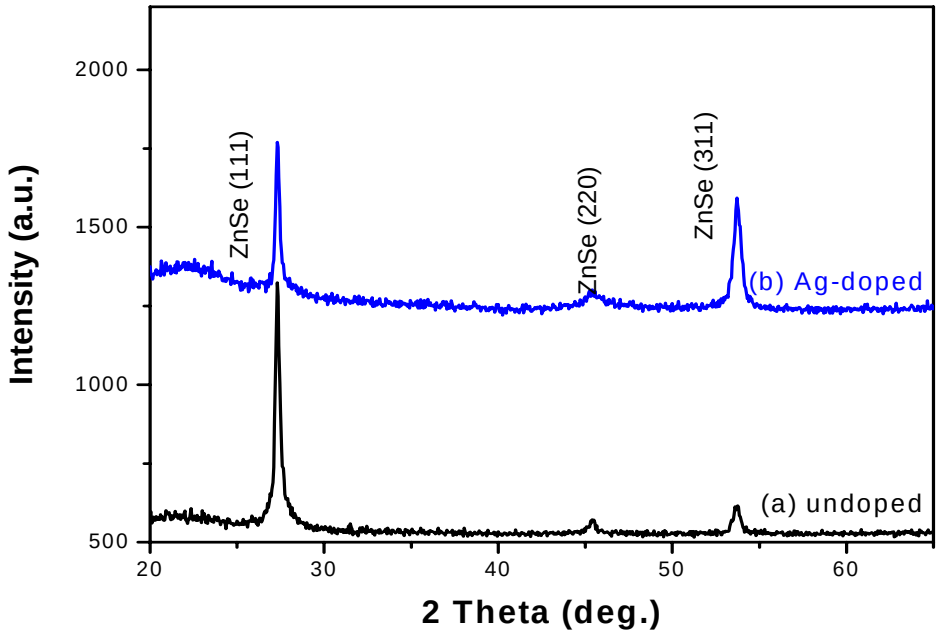

Figure 3.5 XRD patterns of (a) an undoped ZnSe film and (b) a Ag-doped ZnSe film.

3.3.3 Doping with nitrogen

Nitrogen doping was tried by admitting nitrogen gas into the deposition chamber during deposition. Different ambient pressures have been tried. Figures 3.6 (b) and (c) show XRD patterns of nitrogen-doped ZnSe films grown at 10 mTorr and 40 mTorr, respectively. Compared with other deposition pressures (1mTorr, 10 mTorr, 500 mTorr), ZnSe films grown at 40 mTorr have better crystallinity, determined from XRD results. From Figure 3.6, it can be seen that nitrogen doping has turned ZnSe films from cubic to hexagonal phase. A higher resolution XRD measurement has been done as shown in Figure 3.7(d). The peak shifts to a larger angle, indicating a decrease of lattice constant.

Transmittance and reflectance of nitrogen-doped ZnSe films have been measured as shown in Figure 3.8(e). Absorption coeffcients have been calculated using the equation

$\alpha = -\frac{1}{d}\ln\left(\frac{T}{1-R}\right)$. Plots of $(\alpha dhv)^2$ vs hv are shown in Figure 3.9. Bandgaps are calculated by extrapolation of $(\alpha hv)^2$ near the band edges. The bandgap is decreased by 155 meV from 2.626 eV to 2.471 eV. The change of absorption coefficients at the band edge becomes less steep after nitrogen doping, which is due to nitrogen doping induced defects.

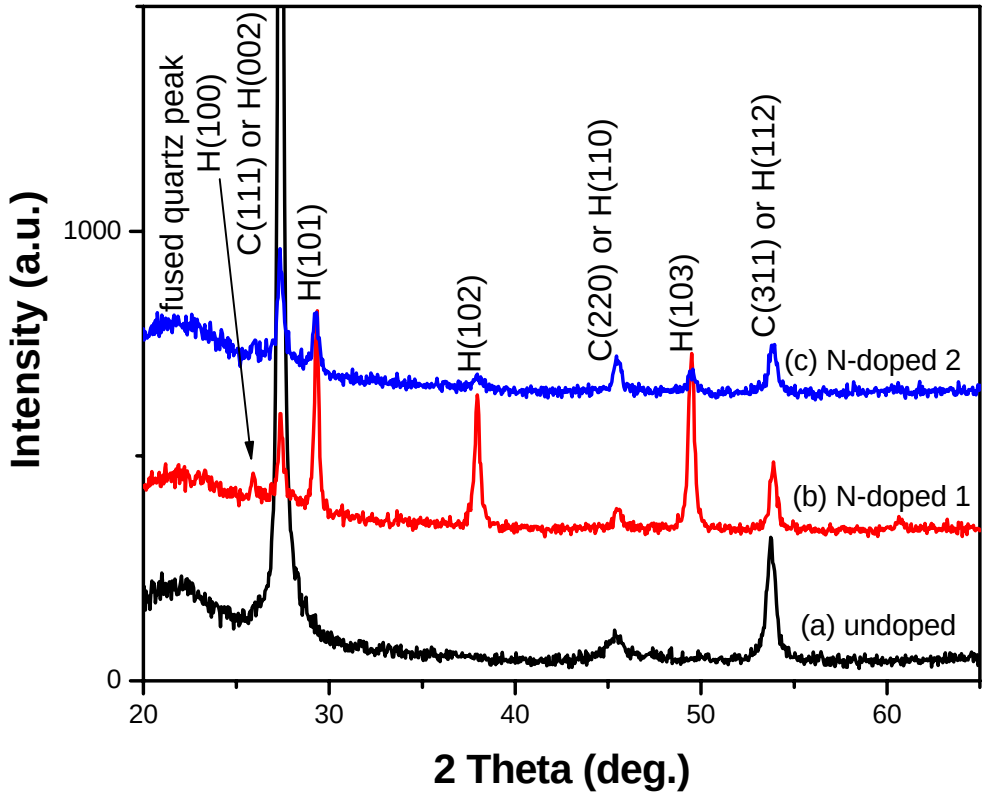

Figure 3.6 XRD patterns of (a) an undoped ZnSe film, (b) a nitrogen-doped ZnSe film deposited with an ambient nitrogen pressure of 40 mTorr, and (c) a nitrogen-doped ZnSe film deposited with an ambient nitrogen pressure of 10 mTorr. (C represents cubic phase, and H represents hexagonal phase).

Figure 3.10 shows Raman spectra of nitrogen-doped and undoped ZnSe films. 2TA (~139.21 cm^{-1}), TO (~202.239 cm^{-1}), and LO (~250.48 cm^{-1}) peaks of ZnSe films are observed. After nitrogen doping, the peaks become weaker and broader, indicating a decreased quality or increased disorder of films due to nitrogen doping. However, two new peaks appeared at 555 cm^{-1} and 602 cm^{-1}.

The observed Raman peak (~555 cm^{-1}) is consistent with the peak (~553 cm^{-1}) observed in localized vibrational mode absorption of ZnSe films after nitrogen

implantation. [21] The vibrational frequency is consistent with the substitution of N on Se sites in ZnSe films, verified by the authors with isotopic substitution of ^{14}N and ^{15}N. As is well-known, in hexagonal phase, there will be two LO phonon modes (A1 and E1). It is believed that the peak around 602 cm^{-1} is due to this phase change induced splitting.

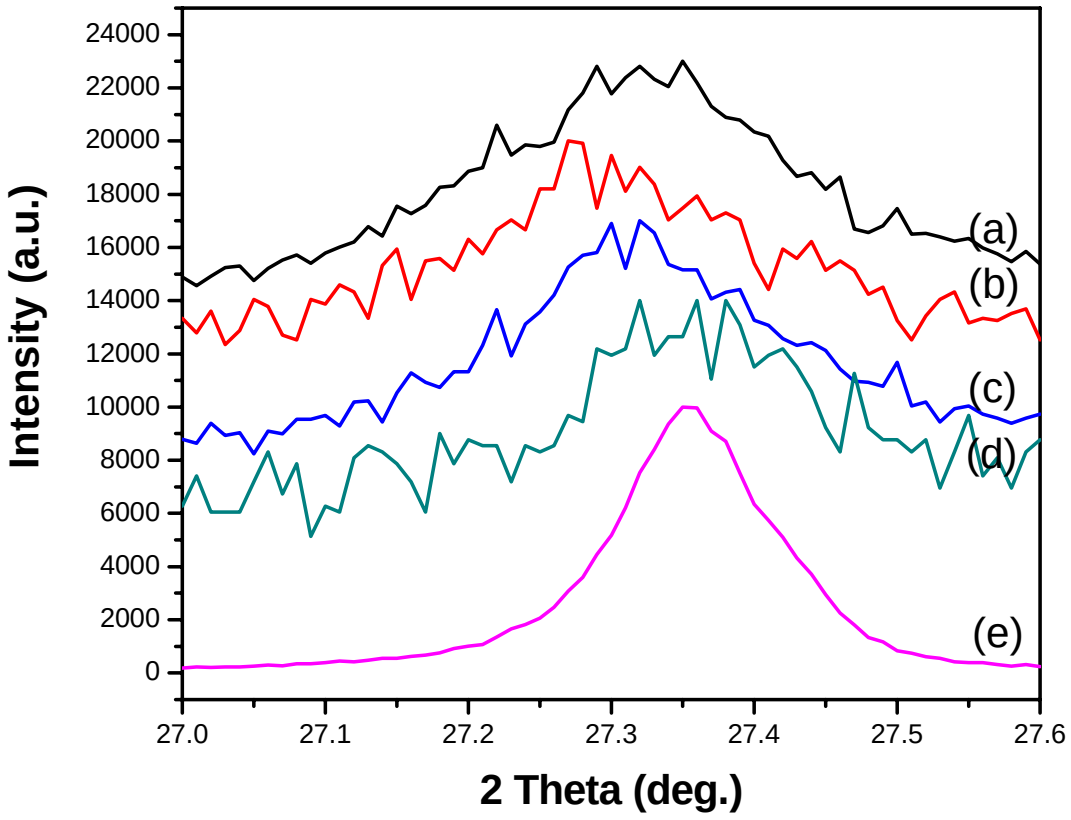

Figure 3.7 Small region XRD patterns of (a) undoped, (b) Cu-doped, (c) Ag-doped, (d) nitrogen-doped, and (e) Cu_2Se-doped ZnSe thin films.

Zunger *et al.*. have calculated the T=0 energy difference ΔE_{W-ZB} between wurtzite (W) structure and zinc-blende (ZB) for binary octet semiconductors using a numerically precise implementation of the first-principles local-density formalism (LDF), including structural relaxations [22] The result of phase change of ZnSe films after nitrogen doping is consistent with the linear model they proposed to explain the relationship between ΔE_{W-ZB} and atomistic orbital radii. As the anions change from Se to N, the anion size decreases, which in turn causes the size difference to increase, favoring the wurtzite phase.

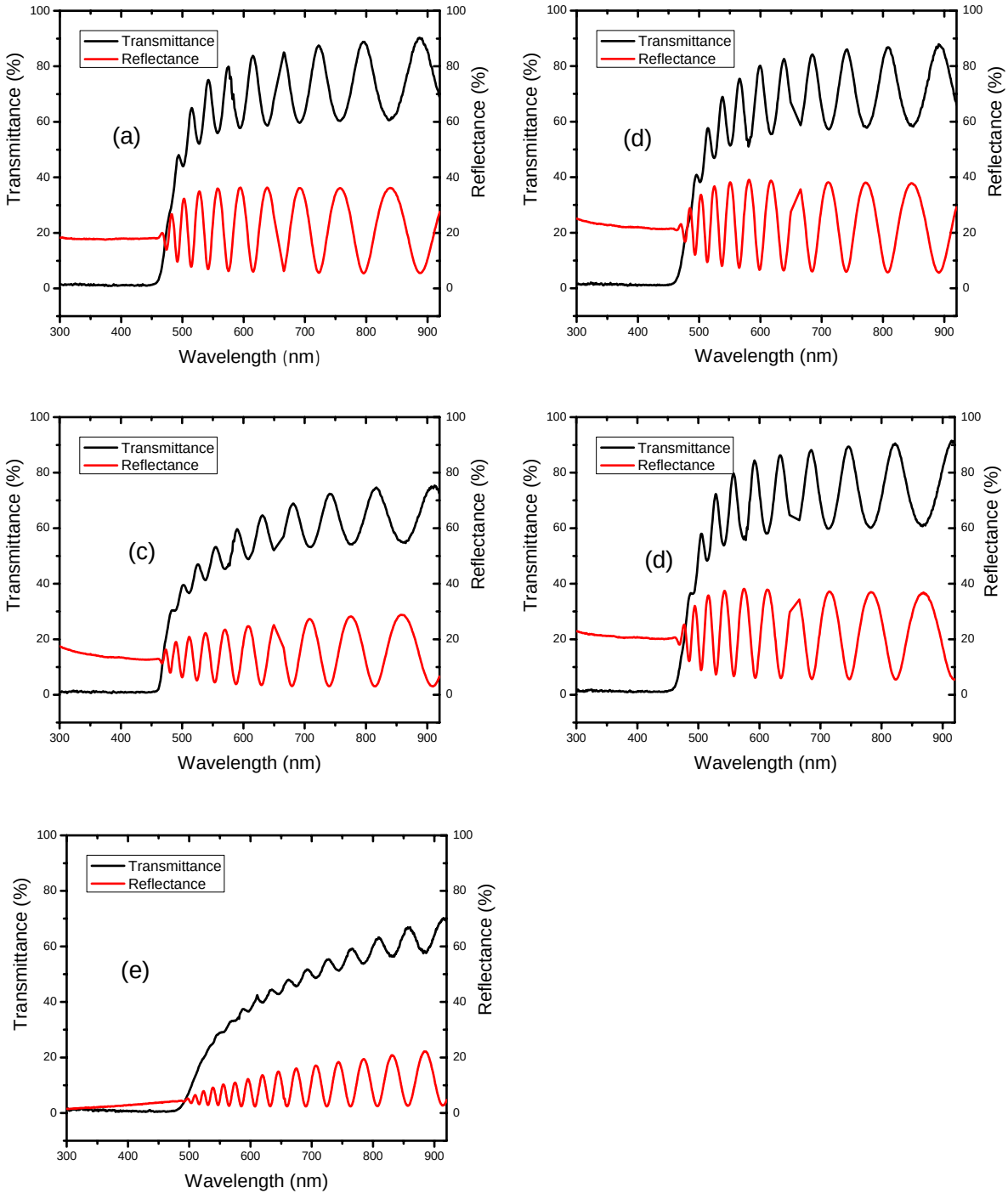

Figure 3.8 Transmittance and reflectance spectra of (a) undoped, (b) Cu-doped, (c) Cu_2Se-doped, (d) Ag-doped, and (e) nitrogen-doped ZnSe thin films.

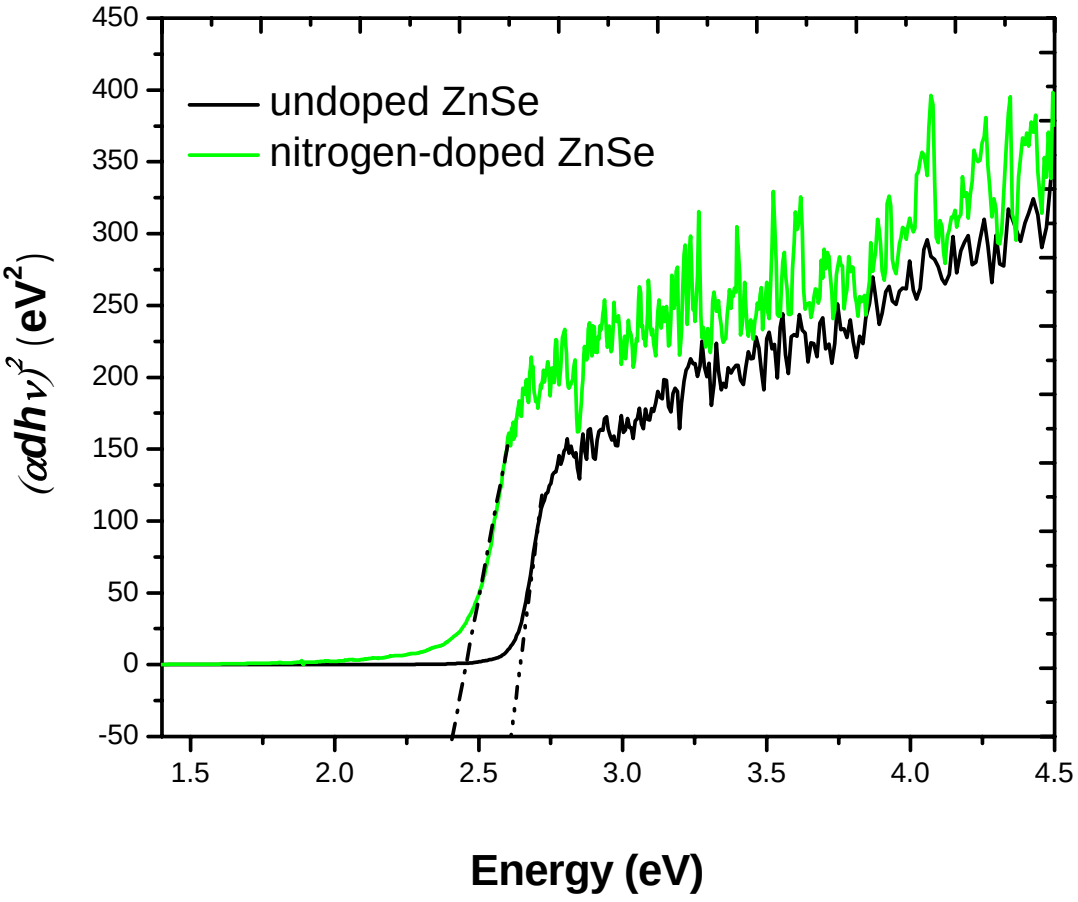

Figure 3.9 Plots of $(\alpha dh\nu)^2$ vs $h\nu$ for bandgap calculation.

Polytypism is a form of polymorphism in which different structures differ only in stacking sequences of identical, two-dimensional sheets or layers. Zinc blende (ZB) and wurtzite (W) are the most common polytypes with tetrahedrally bonded covalent structures. Expected to be free of stress and dangling bonds, heterostructures of zinc blende and wurtzite polytypes have great potential applications in band-structure engineering, spatial localization of electrons and holes, and study of anomalous photovoltaic effect. [23-26] In addition, due to the splitting of valence band maximum in wurtzite structure, the laser threshold of wurtzite ZnSe should be lower than that of zinc blende ZnSe. [27] Therefore, this work is of importance for these applications.

However, while zinc blende ZnSe films have been extensively studied, due to the difficulty of growing stable wurtzite ZnSe films, there are very few reports on wurtzite ZnSe films, which caused the difficulty of fabricating ZnSe-based polytypism. [28]

High-temperature X-ray diffraction showed that the cubic-hexagonal phase transformation occurred at a high temperature of 1425 °C. [29] There are some reports of hexagonal ZnSe. [30-32] However, the work has been extensively focuses on nanostructures. The occurrence of wurtzite phase in these reports can be explained from the thermodynamic point of view. [33] The surface energy of {1100} wurtzite planes is lower than {110} and {111} zinc-blende planes. [34] Therefore for nanostructures, in which surface energy plays a more important role, wurtzite structure can become more stable than zinc-blende structure. These wurtzite ZnSe nanostructures are not good for practical applications. It is believed that the work is promising for achieving stable wurtzite ZnSe films.

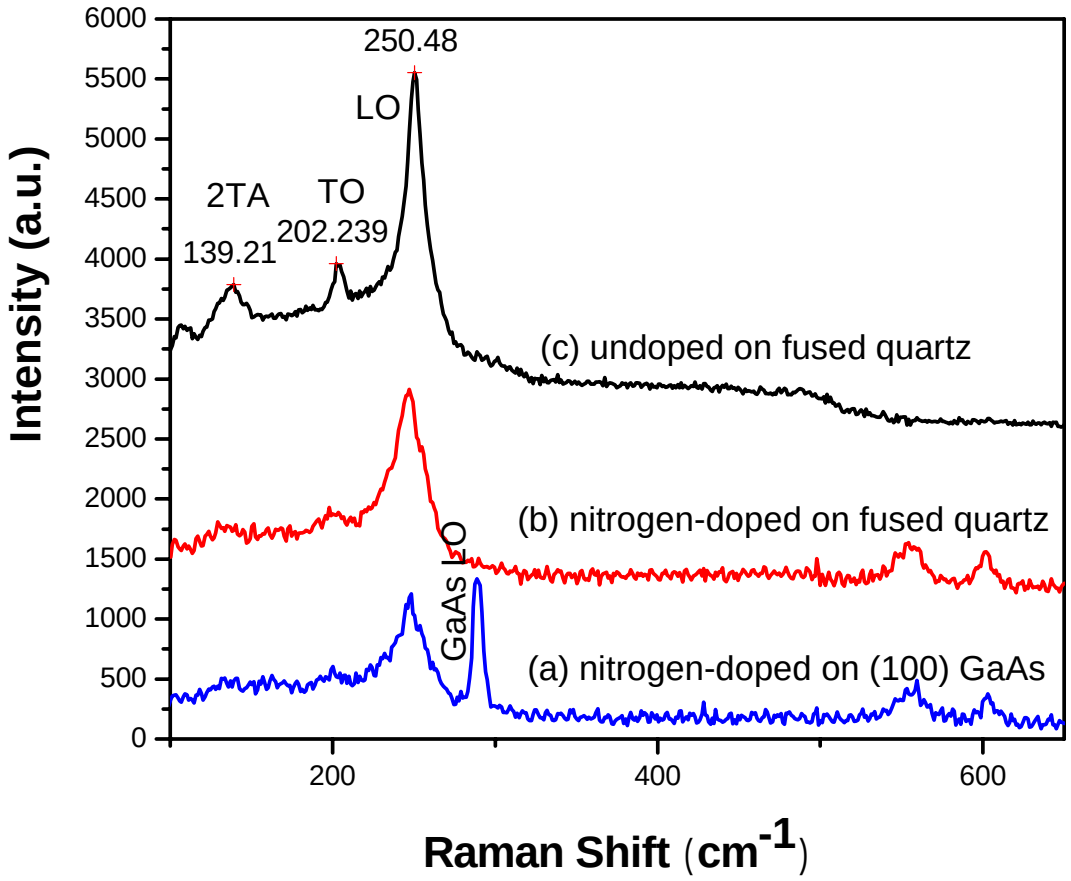

Figure 3.10 Raman spectra of (a) nitrogen-doped ZnSe film on (100) GaAs substrate, (b) nitrogen-doped ZnSe film on fused quartz substrate, and (c) undoped ZnSe film on fused quartz substrate.

Although all the results and analysis above indicate that N has replaced Se and gone into the lattice sites, the nitrogen-doped samples are all non-conductive. Similar to another II-VI wide-bandgap semiconductor ZnO, this difficulty of p-type doping by

nitrogen is believed to be due to compensating defects arising from the presence of native defects or other impurities. [35-37] Further work can be done for better understanding of the doping difficulties of these wide-bandgap semiconductors.

3.4 Summary

In summary, we have tried p-type doping of ZnSe films by Cu, Se, Cu_2Se, Ag, Ag_2Se, and nitrogen. Heavily p-type ZnSe by Cu_2Se doping has been demonstrated. For Cu_2Se-doped samples with Cu composition less than 15 mol%, no phase separation is observed. It is revealed that Cu_2Se doping can significantly promote grain growth and (111) texturing of ZnSe films. Optical spectroscopy measurements indicate that the bandgap is slightly modified from intrinsic ZnSe upon doping. Exceptional p-type conductivity is observed in Cu_2Se doping, with hole concentrations of $\sim 1.1 \times 10^{19}$ cm^{-3} and resistivities of ~0.098 Ohm•cm. Linear I-V curves have also been achieved. Ag and nitrogen are not successful in p-type doping of ZnSe. Nitrogen doping has turned ZnSe films more favorable to wurtzite structures. Two newly observed Raman peaks at 555 cm^{-1} and 602 cm^{-1} are assigned to N local vibrational modes of hexagonal ZnSe structures. The nitrogen-doped ZnSe films are not conductive, which might be due to compensating defects arising from the presence of native defects or other impurities. This work can be good for understanding nitrogen doping difficulties and solve the p-type doping problems of ZnSe films.

References:

[1] K. Ohkawa, T. Karasawa, and T. Mitsuyu, Japanese Journal of Applied Physics Part 2-Letters **30,** L152-L155 (1991).

[2] R. M. Park, M. B. Troffer, C. M. Rouleau, J. M. Depuydt, and M. A. Haase, Applied Physics Letters **57,** 2127-2129 (1990).

[3] J. Qiu, J. M. Depuydt, H. Cheng, and M. A. Haase, Applied Physics Letters **59,** 2992-2994 (1991).

[4] R. M. Park, M. B. Troffer, E. Yablonovitch, and T. J. Gmitter, Applied Physics Letters **59,** 1896-1898 (1991).

[5] Y. Koide, T. Kawakami, N. Teraguchi, Y. Tomomura, A. Suzuki, and M. Murakami, Journal of Applied Physics **82,** 2393-2399 (1997).

[6] Y. Fan, J. Han, L. He, J. Saraie, R. L. Gunshor, M. Hagerott, H. Jeon, A. V. Nurmikko, G. C. Hua, and N. Otsuka, Applied Physics Letters **61,** 3160-3162 (1992).

[7] W. Faschinger, J. Nurnberger, E. Kurtz, R. Schmitt, M. Korn, K. Schull, and M. Ehinger, Semiconductor Science and Technology **12,** 1291-1297 (1997).

[8] S. Tomiya, S. Kijima, H. Okuyama, H. Tsukamoto, T. Hino, S. Taniguchi, H. Noguchi, E. Kato, and A. Ishibashi, Journal of Applied Physics **86,** 3616-3623 (1999).

[9] R. G. Dandrea and C. B. Duke, Applied Physics Letters **64,** 2145-2147 (1994).

[10] P. M. Mensz, Applied Physics Letters **64,** 2148-2150 (1994).

[11] J. S. Song, J. H. Chang, M. W. Cho, T. Hanada, and T. Yao, Journal of Crystal Growth **229,** 104-108 (2001).

[12] J. L. Lei, F. McLarnon, and R. Kostecki, Journal of Physical Chemistry B **109,** 952-957 (2005).

[13] A. M. Hermann, C. Gonzalez, P. A. Ramakrishnan, D. Balzar, N. Popa, P. Rice, C. H. Marshall, J. N. Hilfiker, T. Tiwald, P. J. Sebastian, M. E. Calixto, and R. N. Bhattacharya, Solar Energy Materials and Solar Cells **70,** 345-361 (2001).

[14] K. H. Kim, K. H. Yoon, J. H. Yun, and B. T. Ahn, Electrochemical and Solid State Letters **9,** A382-A385 (2006).

[15] H. Cheng, J. M. Depuydt, J. E. Potts, and M. A. Haase, Journal of Crystal Growth **95,** 512-516 (1989).

[16] M. A. Haase, H. Cheng, J. M. Depuydt, and J. E. Potts, Journal of Applied Physics **67,** 448-452 (1990).

[17] H. Cheng, J. M. Depuydt, J. E. Potts, and T. L. Smith, Applied Physics Letters **52,** 147-149 (1988).

[18] I. S. Hauksson, J. Simpson, S. Y. Wang, K. A. Prior, and B. C. Cavenett, Applied Physics Letters **61,** 2208-2210 (1992).

[19] S. Poykko, M. J. Puska, and R. M. Nieminen, Physical Review B **57,** 12174-12180 (1998).

[20] P. J. Dean, B. J. Fitzpatrick, and R. N. Bhargava, Physical Review B **26,** 2016 (1982).

[21] H. J. Stein, Applied Physics Letters **64,** 1520-1522 (1994).

[22] C.-Y. Yeh, Z. W. Lu, S. Froyen, and A. Zunger, Physical Review B **46,** 10086 (1992).

[23] Z. Z. Bandicacute and Z. Ikonicacute, Physical Review B **51,** 9806 (1995).
[24] F. Bechstedt, auml, and P. ckell, Physical Review Letters **75,** 2180 (1995).
[25] G. Shachar and Y. Brada, Journal of Applied Physics **41,** 3127-3133 (1970).
[26] O. Brafman, I. T. Steinberger, Franenke.Bs, Z. H. Kalman, and E. Alexander, Journal of Applied Physics **35,** 1855 (1964).
[27] A. T. Meney and E. P. O. Reilly, Applied Physics Letters **67,** 3013-3015 (1995).
[28] A. Ohtake, J. Nakamura, M. Terauchi, F. Sato, M. Tanaka, K. Kimura, and T. Yao, Physical Review B (Condensed Matter and Materials Physics) **63,** 195325/1-195325/4 (2001).
[29] I. Kikuma and M. Furukoshi, Journal of Crystal Growth **71,** 136-140 (1985).
[30] Y. Jiang, X. M. Meng, W. C. Yiu, J. Liu, J. X. Ding, C. S. Lee, and S. T. Lee, Journal of Physical Chemistry B **108,** 2784-2787 (2004).
[31] Y. C. Zhu and Y. Bando, Chemical Physics Letters **377,** 367-370 (2003).
[32] C. X. Shan, Z. Liu, X. T. Zhang, C. C. Wong, and S. K. Hark, Nanotechnology **17,** 5561-5564 (2006).
[33] I. Zardo, S. Conesa-Boj, F. Peiro, J. R. Morante, J. Arbiol, E. Uccelli, G. Abstreiter, and A. F. I. Morral, Physical Review B **80** (2009).
[34] F. Glas, J. C. Harmand, and G. Patriarche, Physical Review Letters **99** (2007).
[35] A. Tsukazaki, A. Ohtomo, T. Onuma, M. Ohtani, T. Makino, M. Sumiya, K. Ohtani, S. F. Chichibu, S. Fuke, Y. Segawa, H. Ohno, H. Koinuma, and M. Kawasaki, Nature Materials **4,** 42-46 (2005).
[36] C. G. Van de Walle, Physical Review Letters **85,** 1012 (2000).
[37] B. Theys, V. Sallet, F. Jomard, A. Lusson, J. F. Rommeluere, and Z. Teukam, Journal of Applied Physics **91,** 3922-3924 (2002).

Chapter 4
Batch Growth of Thin Films by Pulsed Laser Deposition

4.1 Introduction

From chapters 2 and 3, we can see that for thin film fabrication we usually need to change deposition temperature or composition. Considering the time for pumping down, deposition, and cooling down, it is very time-consuming to fabricate these films with a different deposition temperature or a different composition one by one. In this chapter, batch growth of these films is to be discussed. Experimental results of batch grown films are presented.

4.2 Batch Growth of Thin Films with Different Deposition Temperatures

4.2.1 Introduction

As has been discussed in chapter 3, wide bandgap semiconductors such as ZnSe and ZnO have attracted great interest due to their potential applications in optical devices such as light emitting diodes and lasers. [1,2] Extensive studies have been done to improve their film quality. However, reports of the optimized growth conditions are not consistent. ZnSe films grown by pulsed laser deposition (PLD) are reported to show best quality at deposition temperatures ranging widely from 300 °C to 450 °C. [3-6] The temperature difference may result from instrumental errors or difference between thermocouple temperature and film surface temperature. For each individual system, distance from thermocouple to substrate, contact thermoresistances, or even substrate thermoresistance may be different. Therefore, even with reports in literature, for each different fabrication system, it is desirable to deposit a series of films and find a best deposition temperature. For a new material without enough reports in literature, it is obviously more desirable to fabricate them at different temperatures. In addition, with knowledge of such a relationship of film growth with deposition temperature, it is possible to find problems in growth of ZnSe films and solve them accordingly.

In this part, ZnSe films with different deposition temperatures have been deposited on fused quartz substrates by pulsed laser deposition. Instead of depositing films one by one, all the substrates were mounted on a plate holder that has a natural temperature gradient. X-ray diffraction (XRD), optical transmission and reflection, Raman spectroscopy, and Energy Dispersive X-ray analysis (EDX) measurements have been performed to characterize the films. With change of deposition temperatures, ZnSe films are shown to have problems associated with crystalline defects, selenium loss, or phase separation. The results show that deposition temperature and proper selenium adjustment are very

important factors in ZnSe growth and doping. ZnSe films with improved crystallinity and no phase separation have been achieved using a 16 mol%-Se-enriched target.

4.2.2 Experimental Details

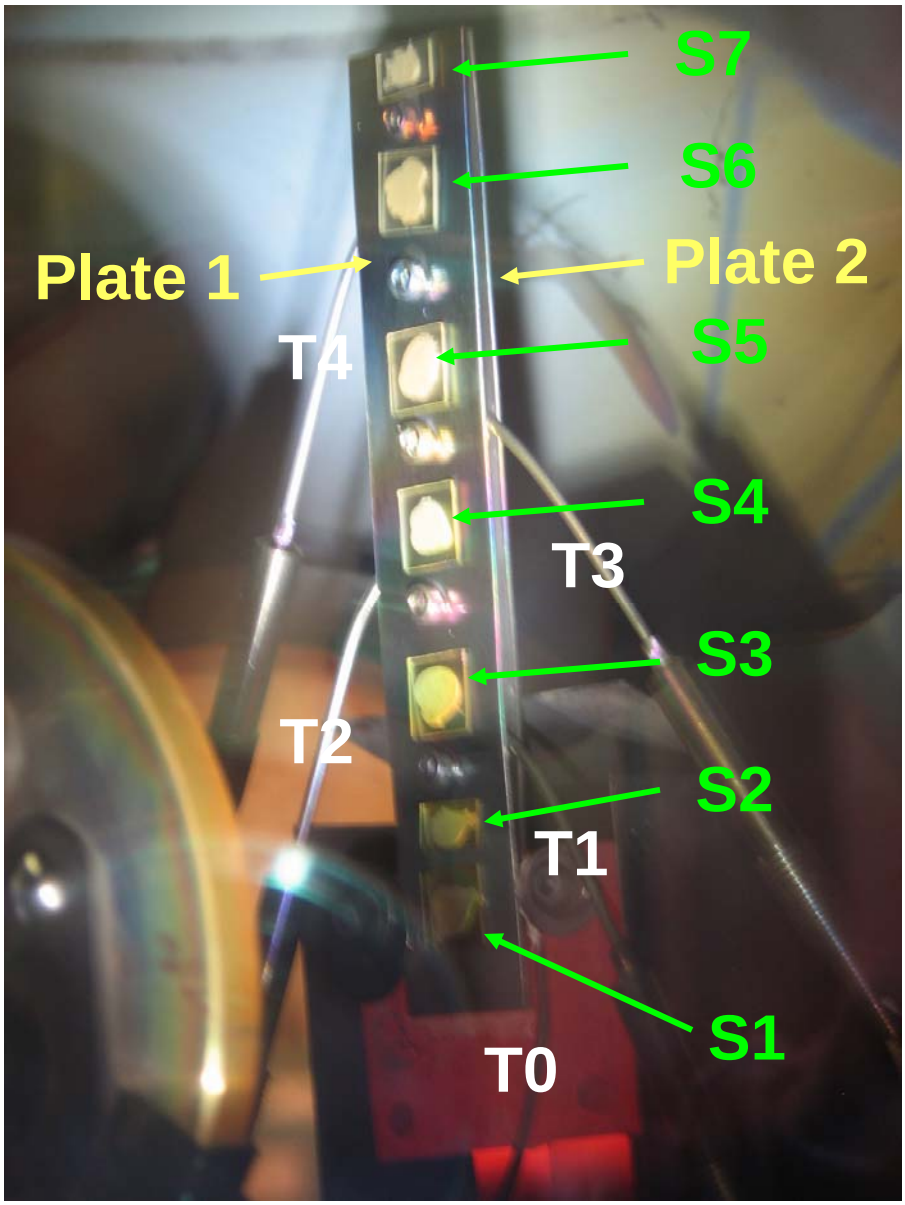

Figure 4.1 An image of the plate substrate holder with samples attached on it.

Two stainless steel plates (20 mm × 120 mm × 0.5 mm) with thermocouples (labeled as T0, T1, T2, T3, and T4 in Figure 4.1) in between were sandwiched together as a substrate holder. One end of the holder was mounted onto a resistance heater. The thermocouples were connected to two UHV feedthroughs for temperature measurement.

In order to reduce contact thermoresistance, silver paste was used to mount samples (7 samples in total, labeled as S1, S2, S3, S4, S5, S6 and S7 in the figure) onto the holder. Mainly due to heat radiation, the plate naturally formed a temperature gradient. The temperatures were obtained by measuring feedthrough pins outside the deposition chamber with a multimeter. Table 4.1 lists measured deposition temperature for each sample. Target-to-plate distance was 8.5 cm. Films were deposited in vacuum with a pressure of 1.6×10^{-6} Torr for 200 minutes. Pulse energy and frequency of the laser were 190 mJ and 8 Hz, respectively.

Table 4.1 Measured deposition temperatures of different samples.

Sample Label	S1	S2	S3	S4	S5	S6	S7
Deposition Temperature (°C)	695	502	293	195	165	133	Not measured, should be less than 133 °C.

X-ray diffraction (XRD) measurement was performed using a Siemens D500 XRD machine with Cu Kα radiation. Optical transmittance and reflectance spectra were obtained using the built-in function of a FilmTek 3000PAR SE ellipsometer. An ISA Groupe Horiba microscope Raman system with an internal He-Ne laser (wavelength: 632 nm) was used. The average acquisition time for each spectrum was 60 seconds. Detail of the Raman spectroscopy measurement can be found in a previous report. [7]

4.2.3 Results and Discussions

After deposition, samples were cooled down naturally. It is found that there was almost no film deposited on sample S1. The film was evaporated at a temperature of 695 °C. Figures 4.2 (a)-(e) show XRD patterns of the other films (samples S2, S3, S4, S5, S6, and S7). In order for better view, the figures are shifted and shown in a log scale. Sample S2, which was deposited at a plate temperature of 502 °C, shows a very strong and sharp (111) peak. However, there is a small amount of wurtzite hexagonal phase as labeled in the figure. Transformation of zincblende cubic phase to wurtzite hexagonal phase has been observed for ZnSe at a temperature above 1425 °C by in-situ X-ray diffraction study. [8] The occurrence of wurtzite phase in the film deposited around 502 °C here is possibly due to high energy of deposited species in pulse laser deposition. Sample S3, which was deposited at 293 °C, shows only cubic phase with preferred (111) orientation. There are some other peaks, such as (220) and (311), but the intensities are much weaker. For other samples, as temperature is lowered, XRD peaks become wider and weaker, which may be due to smaller grains or worse crystallinity at lower temperatures.

A small region θ-2θ XRD scan has also been performed using narrower slits for higher resolution. The results are shown in Figures 4.3(a)-(c). It can be seen that,

compared to sample S3, which has a full width at half maximum (FWHM) of around 0.28°, sample S2 peak is much narrower, with a width of 0.13°. In addition, sample S2 peak shifts to a smaller angle by 0.08°, which tells a 0.3% increase of lattice constant. After subtracting the instrumental broadening, a rough estimation of grain size using Debye-Scherrer equation gives a grain size of about 273 nm and 45 nm respectively for samples S2 and S3. Much broader peaks are observed for samples S4 and S5. A wider range scan of sample S4 (from 26.5° to 28.5°, not completely shown in the figure) shows a width of 0.75°. The estimated grain size is about 13 nm, much smaller than samples S2 and S3.

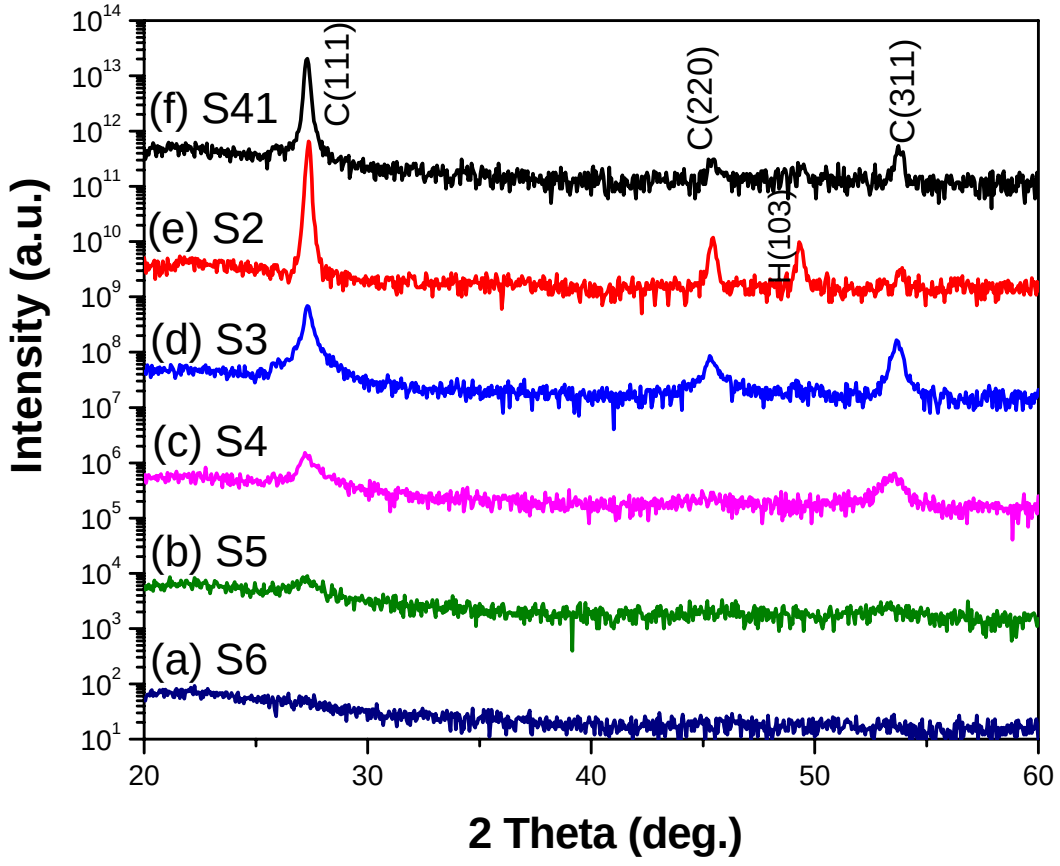

Figure 4.2 XRD patterns of ZnSe thin films deposited on fused quartz substrates ("H" represents hexagonal wurtzite phase; "C" represents cubic zincblende phase).

Figures 4.4 (a)-(f) show Raman spectra of the 6 samples. LO and TO peaks can barely be seen in sample S2, which might be due to lattice disorder induced by phase separation. Among the 6 samples, S3 shows the strongest and sharpest ZnSe LO peak (at 249.6 cm^{-1}) and TO peak (at 203.5 cm^{-1}). For other samples (S4, S5, S6, and S7), as temperature decreases, LO and TO peaks become weaker and wider. This Raman result is

consistent with the conclusion from XRD results that among the 6 samples, S3 has best crystallinity and does not show phase separation.

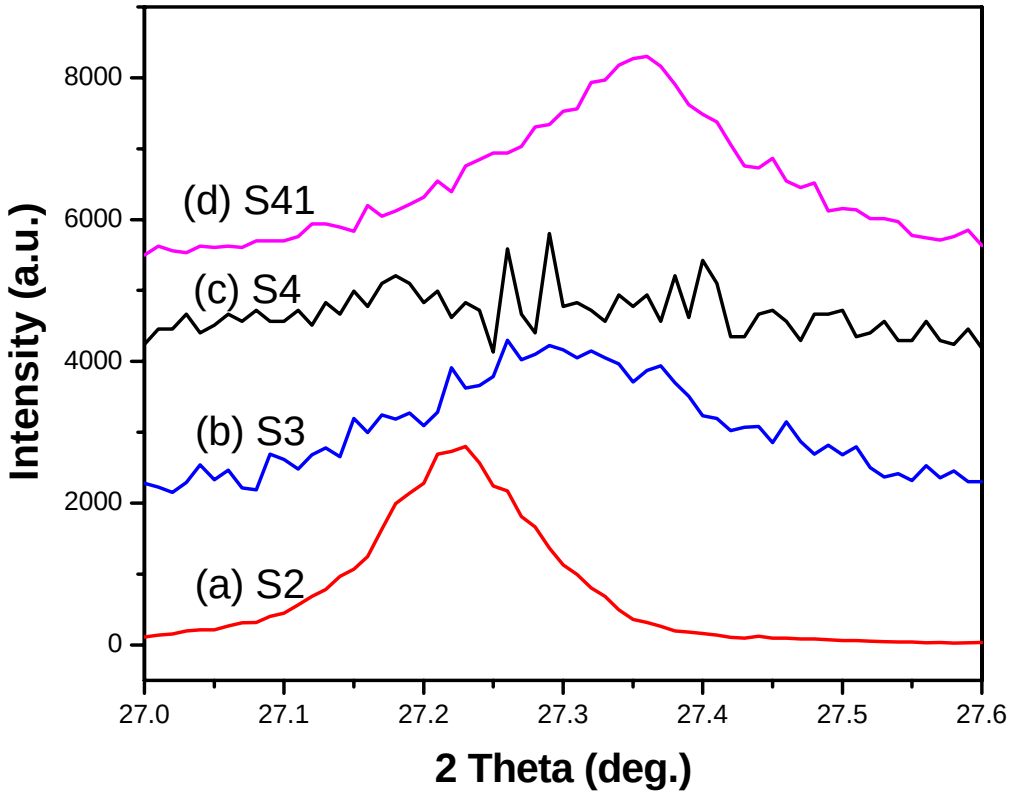

Figure 4.3 A small region θ-2θ XRD scan of ZnSe films.

Optical transmittance and reflectance spectra, shown in Figures 4.5 (a)-(e), were measured using the built-in function of a FilmTek 3000PAR SE ellipsometrer. For samples S2, S3, S4, and S5, dramatic change of transmittance was observed at the band edges. The product of absorption coefficient α and film thickness d has been calculated using the equation $\alpha d = -\ln\left(\frac{T}{1-R}\right)$, where T is transmittance, R is reflectance. For direct bandgap semiconductors, there is a well-known relationship described as $(\alpha h\nu)^2 = C(h\nu - E_g)$. Bandgaps are calculated by extrapolation of the linear part in plots of $(\alpha d h\nu)^2$ vs $h\nu$.

Calculated αd results are plotted in Figures 6 (a)-(f). Compared with other samples (samples S4, S5, S6, and S7), samples S2 and S3 have steeper slopes at the band edges. However, sample S2 shows a tail at the lower energy region. The absorption of sample S2 at lower energies might result from selenium deficiency related defects. As

temperature lowers, the slope becomes less and less steep. The extrapolated optical bandgaps are about 2.66 eV, which is consistent with previous reports in the literature. [9-11]

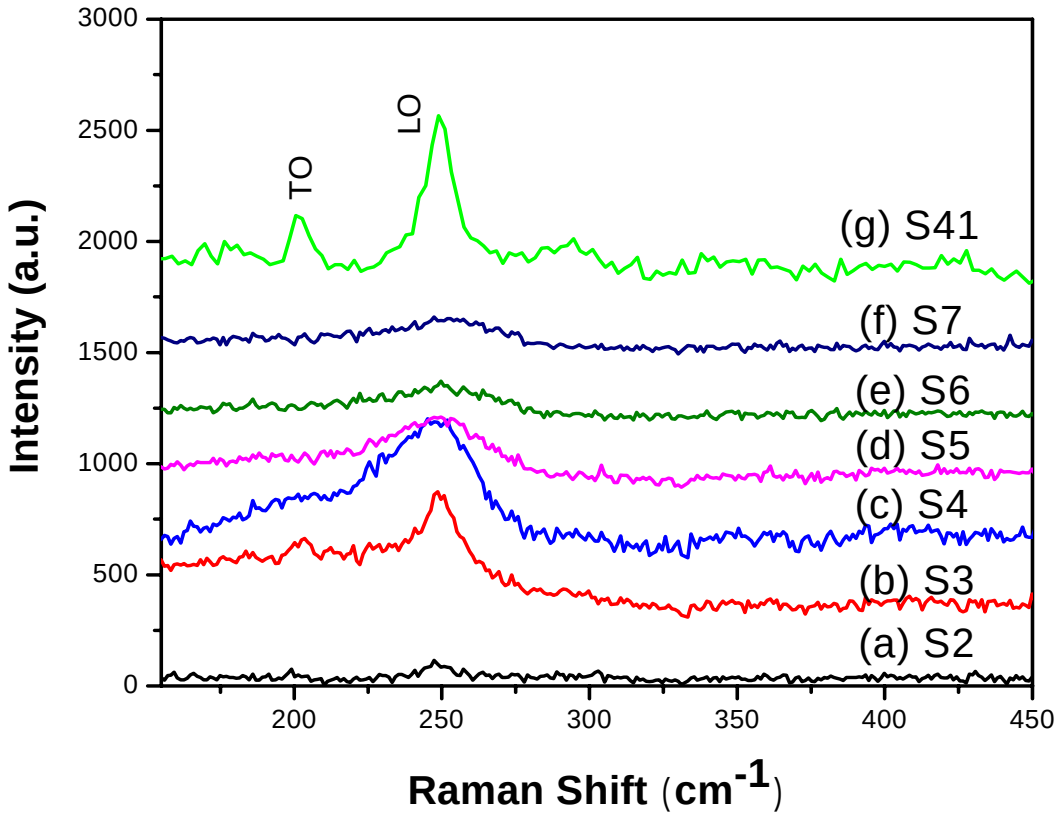

Figure 4.4 Raman spectra of ZnSe thin films.

As mentioned above, ZnSe films deposited above 502 °C will evaporate or have a phase separation problem. For films deposited at 300 °C or lower, surface diffusion is inhibited. Films will have problems associated with crystalline defects. They may have more grain boundaries due to smaller grains, or even become amorphous.

Since selenium normally has a higher saturation pressure than zinc[12], evaporation can cause selenium deficiency in ZnSe films. Energy Dispersive X-ray analysis (EDX) has been performed. For samples S4, S3 and S2, the atomic ratios of Zn to Se are 1: 0.871, 1: 0.80, 1: 0.751, respectively. The ratio decreases with increase of deposition temperature, indicating increased selenium loss at higher temperatures.

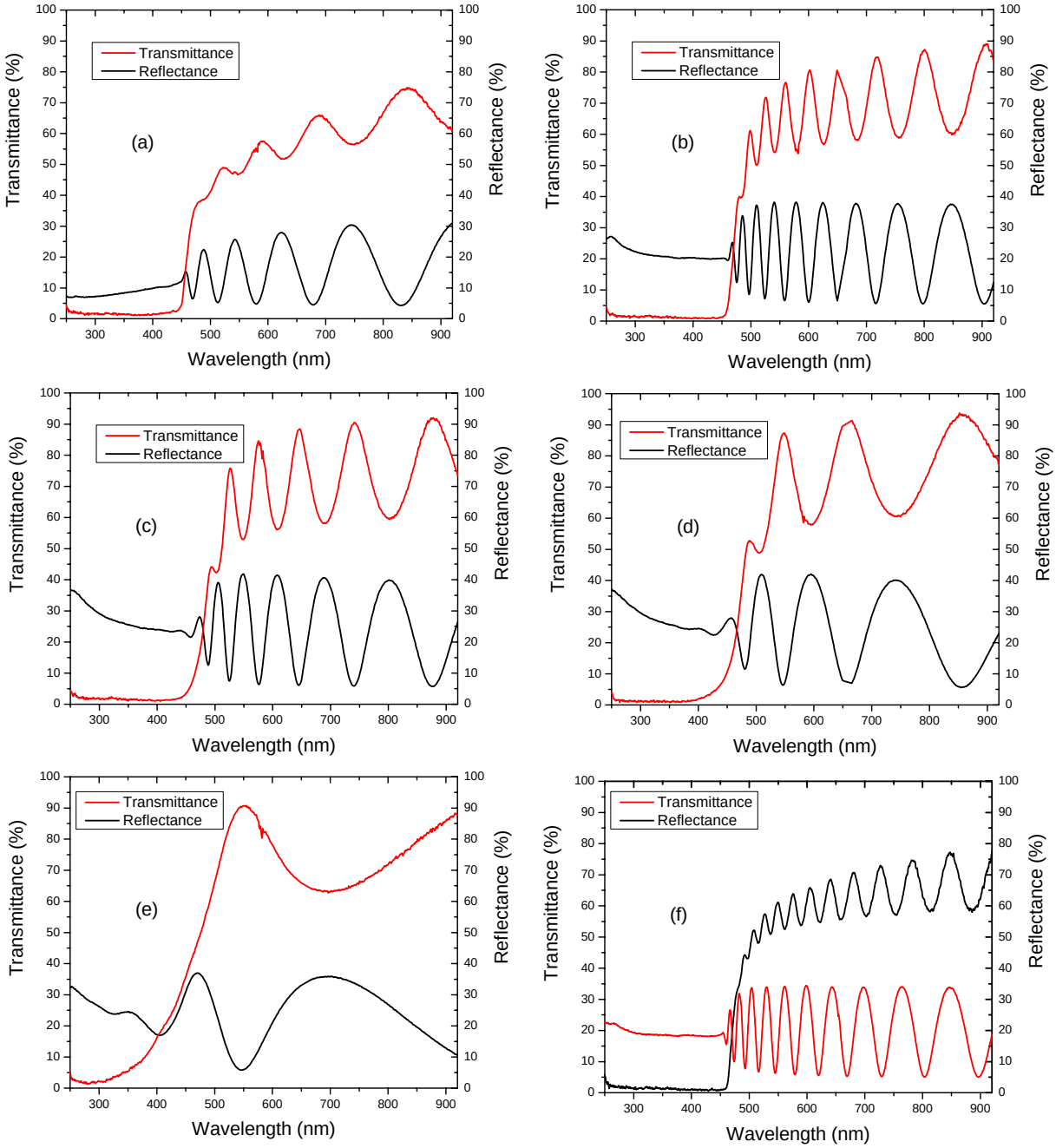

Figure 4.5 Transmission and reflection spectra of (a) sample S2, (b) sample S3, (c) sample S4, (d) sample S5, (e) sample S6, and (f) sample S41.

In order to solve these problems, another ZnSe film (sample S41) has been deposited at 400 °C using a 16mol% Se-enriched ZnSe target. The results are shown in Figures 4.2(f), 4.3(d), 4.4(g), 4.5(f), and 4.6(g). No ZnSe wurtzite peaks or selenium peaks are obviously observed in Figure 4.2(f). The (111) peak of sample S41, with a width of 0.18°,

is narrower than that of sample S3 (about 0.28°). Compared with S2 peak, it shifts to a larger angle by 0.14°. The XRD results reveal that ZnSe lattice constant increases with increase of selenium deficiency, and decreases with selenium added in. Raman peaks of sample S41 shown in Figure 4.4(g) are sharper and stronger, which indicates increased crystallinity or reduced defects. A dramatic change of absorption coefficient at the band edge is shown in Figure 4.6(g). The absorption tail observed in sample S2 at the lower energy region is not seen in sample S41.

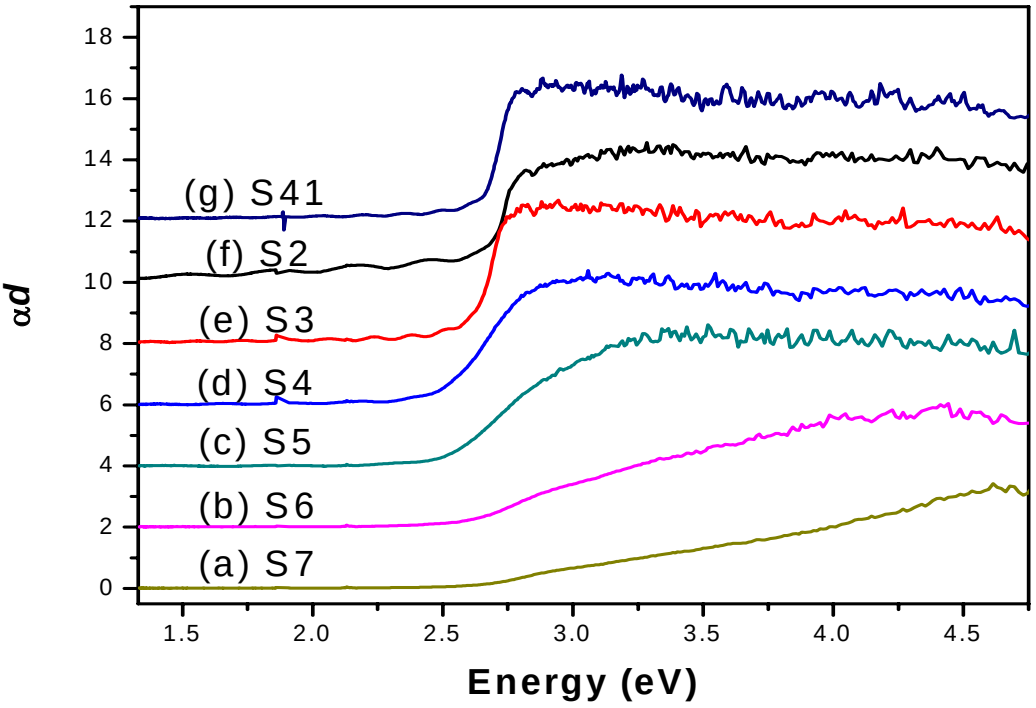

Figure 4.6 Plots of αd vs energy hv.

4.2.4 Summary

In summary, batch growth of ZnSe films with different deposition temperatures has been achieved using the natural temperature gradient of the substrate holder. XRD, Raman, transmittance and reflectance, and EDX measurements have been performed to characterize the films. At higher temperatures the films have phase separation and non-stoichiometry problems. As temperature decreases, there are problems due to crystalline defects. With selenium added in, ZnSe films show improved crystallinity without phase separation. It is believed that at proper deposition temperature and with selenium adjustment, further optimization can be performed to improve film quality or solve doping difficulties of ZnSe films.

4.3 Batch Growth of Thin Films with Different Compositions

4.3.1 Introduction

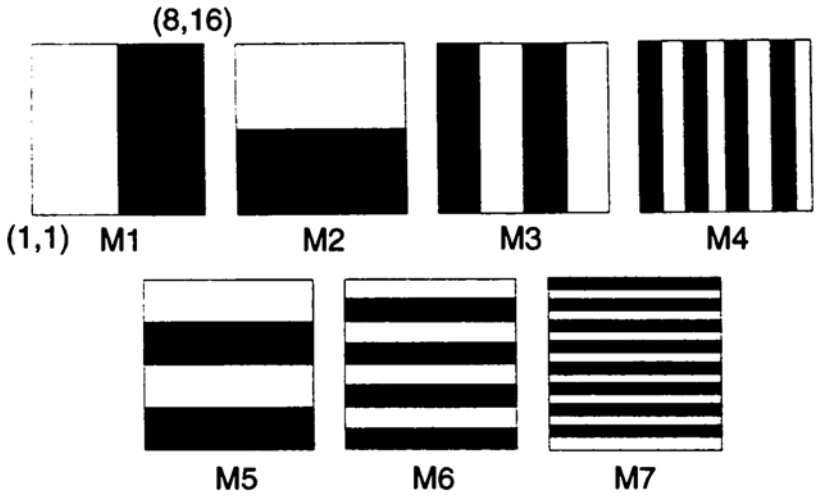

Figure 4.7(a) Binary masks used for combinatorial synthesis. [18]

Figure 4.7(b) A picture of a 128-member binary library prior to sintering. [18]

Recently there has been tremendous interest in compounds of solar cell absorber materials (i.e. $CuIn_xGa_{1-x}Se_2$ [13,14] or $CuIn_{1-x}Ga_xSe_{2-y}S_y$ [15]) and high-temperature superconductive metal oxides (i.e. $Ca(Fe_{1-x}Co_x)_2As_2$ [16] or $HgBa_2Ca_{m-1}Cu_mO_{2m+2+\delta}$ [17]). Properties of these compounds are closely dependent on their components. Optimization of several components has been a great part of materials research on compounds. Usually a series of materials with different compositions will be grown one-by-one in order to study these compounds and optimize the compositions for applications. Evidently this trial-and-error process is extremely time-consuming. Therefore there is a great need for an efficient and systematic way to search through the compounds so that materials research, especially research on those ternary and quaternary materials that have not been well explored, can be greatly facilitated.

In 1995, Xiang *et al.* invented combinatorial method for making compounds, in which they used a series of masks while sputtering precursor targets [18-20] (patent number: 5985356, 6004617, 6326090, 6346290, 7442665). A typical series of masks is shown in Figure 4.7(a). [18] The deposited film was separated by the masks into a library of element samples on the substrate, as shown in Figure 4.7(b). Using a series of steps of changing masks or targets, Xiang *et al.* controlled deposition of precursors onto these elements and obtained different precursor amounts at each element. The precursors at each element were then mixed into one compound through post annealing process. Since amounts of deposited precursors are different at each element, compositions of the compound after annealing are different. Therefore a series of compounds with different compositions can be obtained in a much more efficient way.

However, this combinatorial approach method that combines thin film deposition and physical masking techniques is a mixing-after-deposition process. It has some problems such as phase separation, mask misalignment, complex and time-consuming process, etc. In this paper, a low-cost, high-efficiency multi-plume pulsed laser deposition system is proposed and discussed in detail. This mixing-during-deposition system, supposed to be more uniform and suitable for growth of compound films, can greatly facilitate compound optimization and exploration process.

4.3.2 Instrument Description

An excimer laser (Lambda Physic LPX 210i) produces a high power UV laser beam at a wavelength of 248 nm as shown in Figure 4.8. Using two beam splitters (the first one: 30% reflectance and 70% transmittance; the second one: 50% reflectance and 50% transmittance) and one mirror, the laser beam is split into three beams. The beam splitters are mounted on flippers so that the setup is also compatible for two-beam or one-beam deposition. Before entering the vacuum chamber, those three beams are focused by spherical lenses. Three targets are mounted on a three-target holder and ablated by focused lasers. A substrate heated by a resistance block and covered with a mask is positioned facing the targets. Gas (inert gas or reactive gas like oxygen in some cases) is admitted into the chamber and controlled by a mass flow meter. There is a laser block which is mounted on a linear stage and controlled by a programmable linear motor.

During deposition, the laser block switches among the three positions for each target ablation.

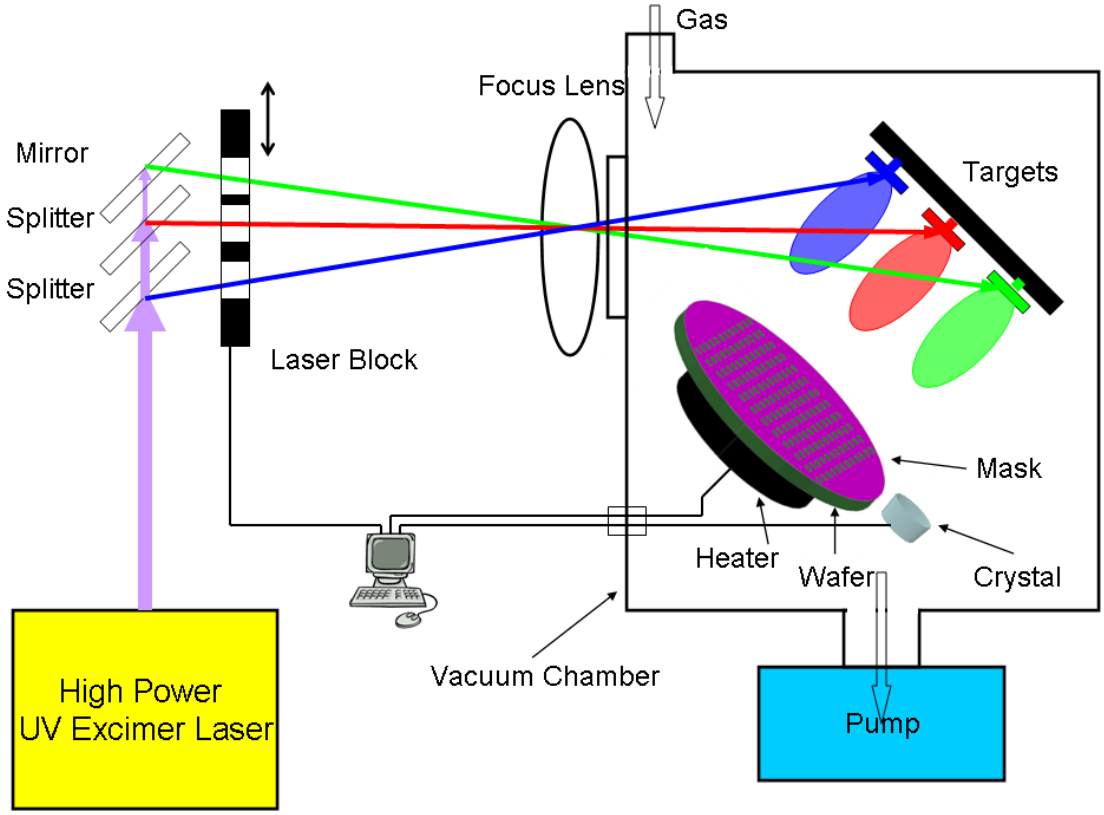

Figure 4.8 Schematic of the three-beam pulsed laser deposition system.

By using a mirror and two beam splitters, the high energy laser beam is split into three laser beams. These three beams are focused by spherical lenses onto three targets (targets A, B, and C). Precursor materials A, B, and C are ablated and deposited onto the substrate. A mask with square holes separates the deposited films into hundreds of small element samples. Since the three plumes caused by ablating three targets are physically separated and thickness of PLD-deposited films on substrate is not uniform, deposition rate of each precursor at each element is different. Therefore for each element sample, ratio of the three precursors is different. If there is no laser block, the three materials will be deposited and mixed simultaneously. It is optional to add a laser block with just one light opening for one laser beam to control starting and ending of the deposition or deposition sequence of the three laser beams. The linear motor can be controlled by a computer or a pre-written program. A crystal monitor measuring film thickness may be connected to a computer as a feedback for controlling.

Pulsed laser deposition has been widely used in materials research since its successful growth of $YBa_2Cu_3O_{7-\delta}$ thin films for high temperature superconductor applications in 1987. [21] As discussed previously, compared with other techniques such

as chemical vapor deposition and sputtering, pulsed laser deposition has many advantages. The composition of thin films deposited by pulsed laser deposition is almost the same as that of the target material. It is relatively easy for PLD to grow stoichiometric materials, which is very important for growth of compound materials such as high-temperature superconductive oxides and compound semiconductors. In addition PLD is a very versatile technology. Most of the materials in the nature can be ablated by high energy UV laser. Therefore PLD can be used to grow most kinds of materials, including metals, semiconductors, superconductors and insulators. The precursor material is just a small pellet, which is much easier to be obtained than in other technologies. Mainly because of these advantages, PLD has been widely used in new materials research and exploration.

However, PLD has a well-known disadvantage, that is, thickness non-uniformity. The thickness of films deposited on substrates can be described with a shape similar to a Gaussian curve. Figure 4.9 shows normalized thickness of a $Pb(Zr,Ti)O_3$ (PZT) film deposited in vacuum. [22] It can be seen that thin film growth rate of PZT is decreased by more than 50 times at a 60 mm distance away from the center.

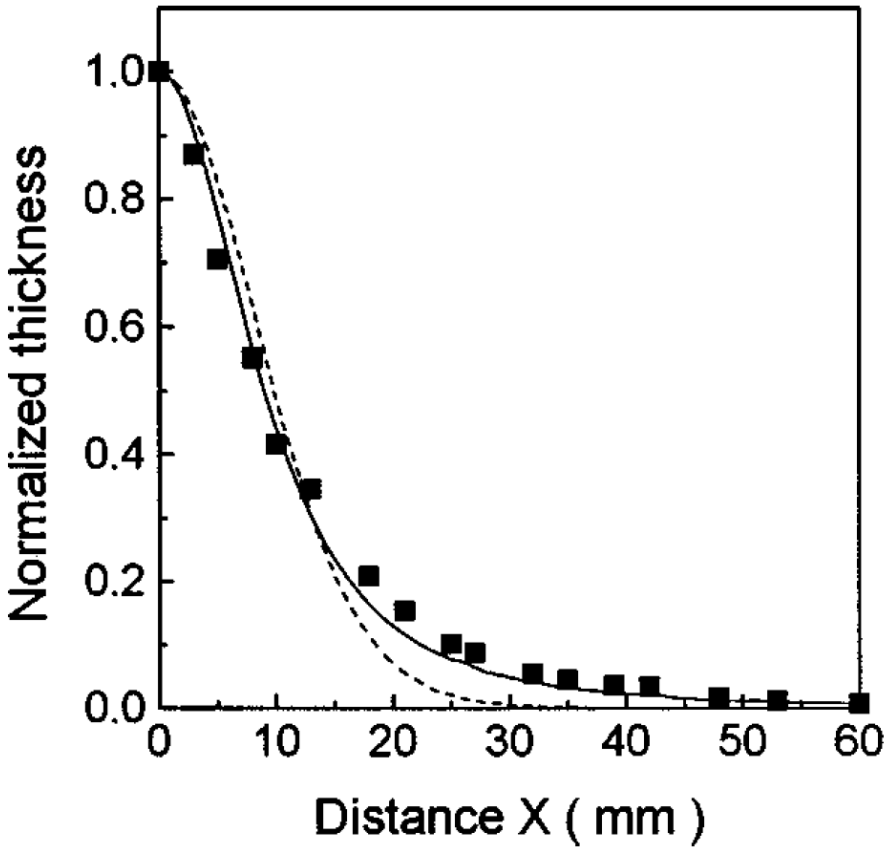

Figure 4.9 Normalized thickness of a PZT film deposited in vacuum as a function of distance from the center of the plume along the *X*-axis direction. The dashed line shows a fit to the $\cos^n$ (x) approximation. [22]

Thickness non-uniformity is usually a problem in thin film deposition, especially for applications where a large area of thin film with consistent and predictable properties is required. Therefore even though PLD has achieved great success on materials research in research laboratories, it has not been widely used in industry. However, non-uniformity is not always a problem. The multi-plume pulsed laser deposition system described in Figure 4.8 is proposed to utilize this property. According to Anisimov *et al.*'s modeling, for the geometry shown in Figure 4.10, the normalized thickness can be expressed as [22-24]:

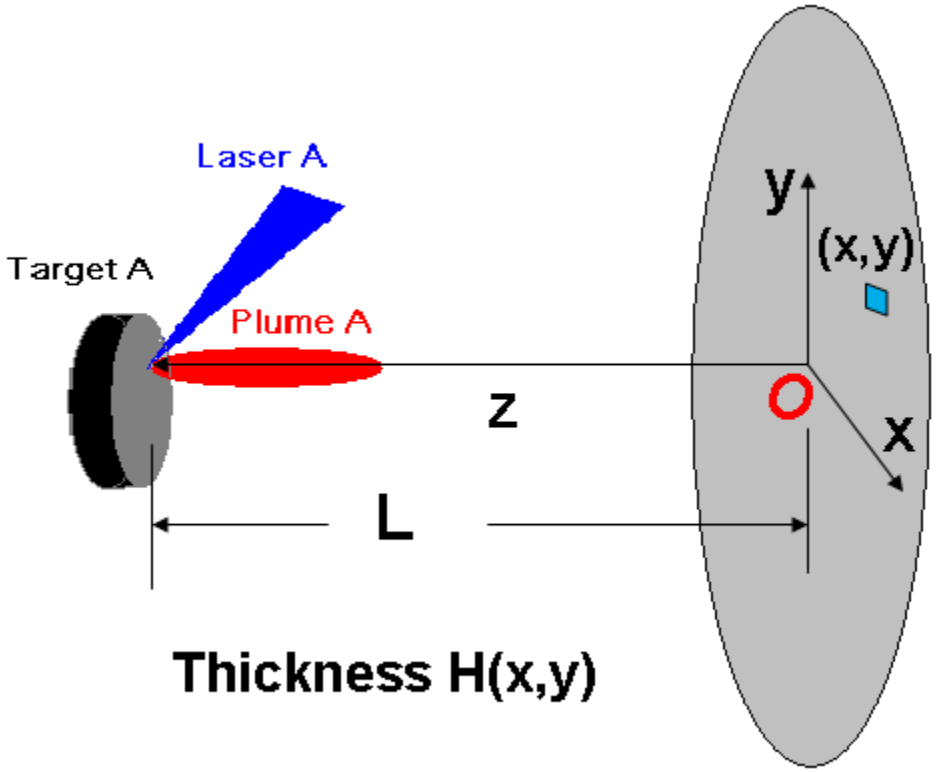

Figure 4.10 A schematic of the pulsed laser deposition geometry.

$$H(x,y) = (1 + ax^2 + by^2)^{-3/2} \qquad (1)$$

In the equation, H is the normalized thickness which equals to 1 at the plume center on the substrate; x and y are the distance to the center along x and y axes, respectively. And,

$$a = \frac{k_\varsigma}{Z_s^{\,2}}, \qquad b = \frac{k_\varsigma}{k_\eta^{\,2} Z_s^{\,2}} \qquad (2)$$

Z_s is the distance between the target and the substrate. k_ς and k_η are values determined by characteristics of plume. They can be changed by adjusting ambient gas pressure, laser pulse energy, etc.

Neglecting the plume-plume interaction and assuming a same molar volume, composition of the compound at each element is simply illustrated in Figure 4.11 using typical values of Z_s, k_ς and k_η (Z_s = 55 mm, k_ς = 4, and k_η = 1). The other two parameters used in the model are l and d. l is the distance between laser spots assuming an equilateral triangle shape of the three spots as illustrated in Figure 4.12. This distance is also the distance between plume centers on the substrate. d is the distance between elements on the substrate. In the simulation of Figure 4.11, l = 60 mm and d = 12.5 mm. It is clear to see three sections on the substrate, A-rich section, B-rich section, and C-rich section. More distributions can be obtained by changing the parameters above.

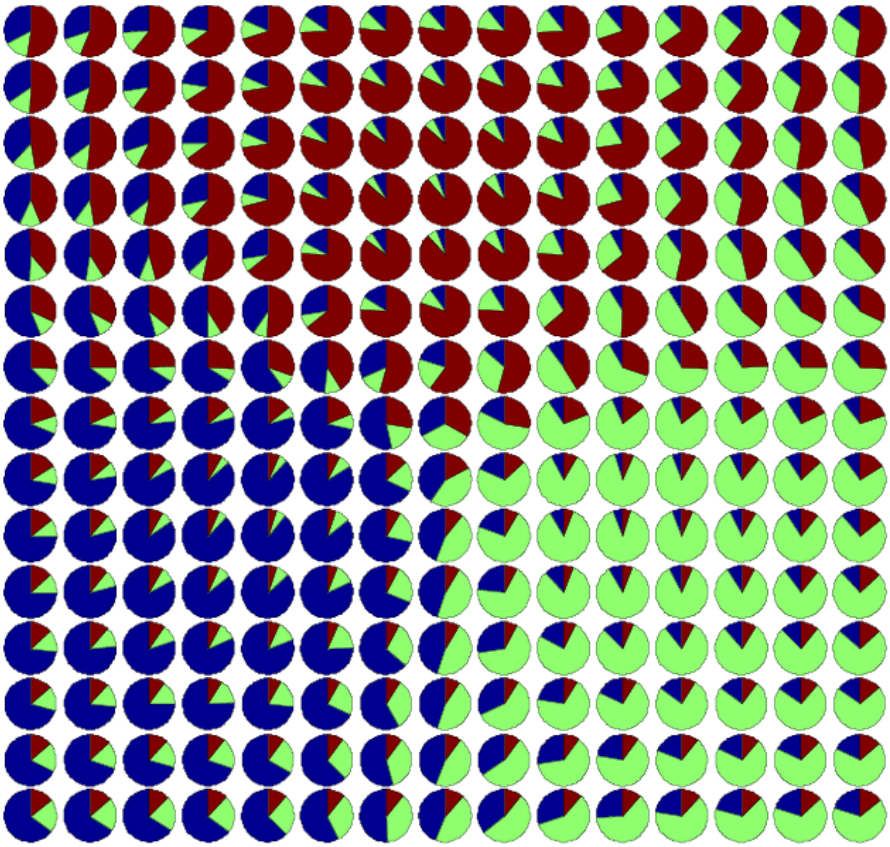

Figure 4.11 A schematic showing compositions on the substrate. Each cycle shows compositions of three precursors by sector areas (red: material A; blue: material B; green: material C) for each corresponding element sample on the substrate.

Therefore, because of the directionality of PLD plumes and thickness non-uniformity of PLD films, this system is supposed to be able to batch grow hundreds of thin films with different compositions on a large substrate.

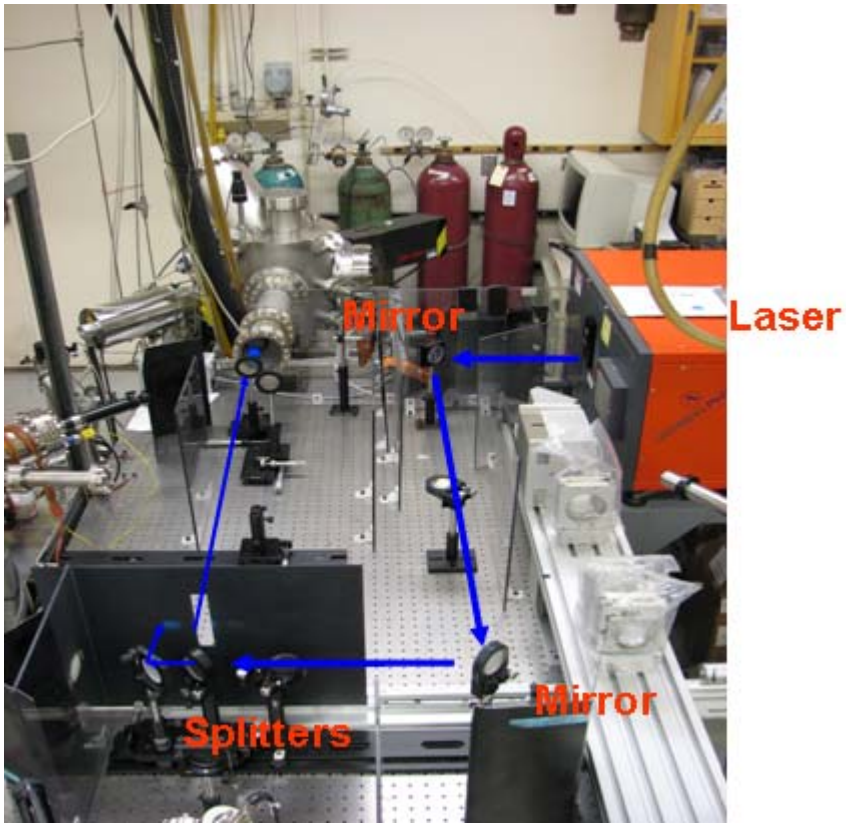

Figure 4.12 The multi-plume pulsed laser deposition system.

4.3.3 Results and Discussions

The system is shown in Figure 4.12. A mask (for 100 element samples), a substrate holder and a three-target holder, and a laser block are shown in Figures 4.13, 4.14, and 4.15, respectively. A typical fused quartz substrate with 100 element samples is shown in Figure 4.16.

Using the automatic scanning function of the FilmTek 3000PAR SE ellipsometer as shown in Figure 4.17 (transmission and reflection mode) with the revised stage, the optical transmittance and reflectance spectra of the sample are obtained. The compositions were measured by X-ray fluorescence (XRF). Optical bandgaps are extrapolated using the method mentioned previously. Using Ag_2Te and Ga_2Te_3 as targets, bandgaps of (Ag, Ga)Te_2 versus Ga and Ag compositions are shown in Figure 4.18. It is

seen that thin films with different Ag or Ga compositions have been successfully obtained in a batch growth way. Bandgaps are ranging from 1.89 eV to 2.375 eV.

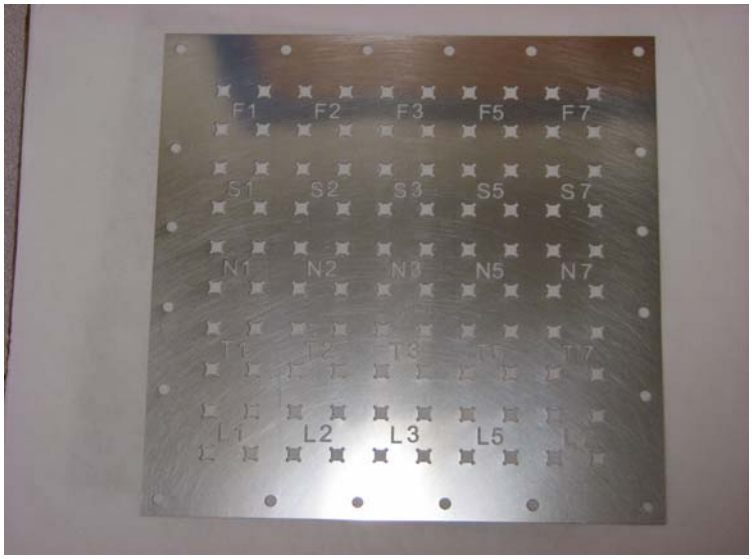

Figure 4.13 A picture of a mask for deposition of 100 samples.

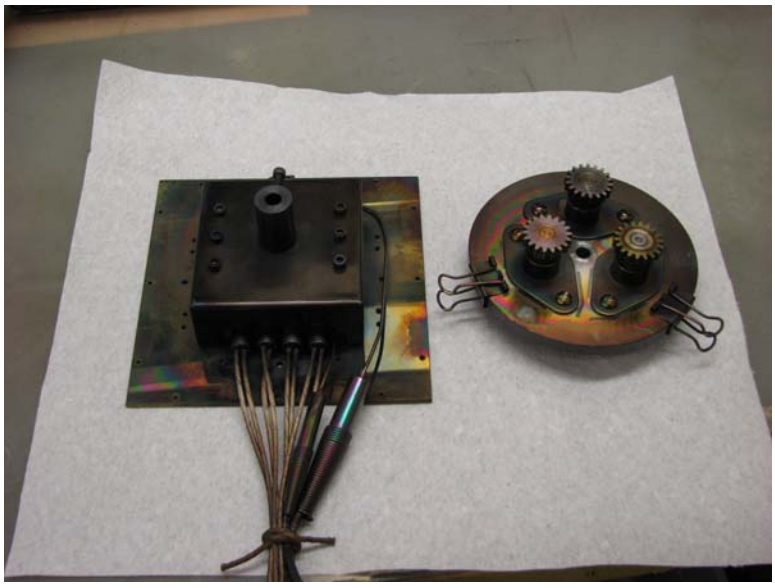

Figure 4.14 A picture of a substrate holder (back side) and a three-target holder.

The multi-plume pulsed laser deposition system proposed is supposed to have the following advantages:

Figure 4.15 A picture of a laser block.

1) Just like combinatorial synthesis, this system can fabricate on a same substrate many compounds together instead of one-by-one fabrication. In order to fabricate one sample in lab, it usually takes one or two days. Using this technique, it can fabricate 100 samples easily within one or two days. Therefore the efficiency of thin film fabrication is increased 100 times or higher.

2) With the ability to fabricate a regular array of compound thin films on a substrate, this technique can also facilitate measurement process instead of one-by-one measurement. By using a simple automatic scanning or programmable switch circuits, the measurement can be automatic and much faster. For example, in order to fabricate hundreds of solar cells on a substrate, electrodes can be deposited first using the same mask. Absorber materials with various compositions or doping can be grown using this technique. After fabrication of an array of heterostructured solar cell devices on substrate, it is possible to measure them by mounting onto a programmed motor stage or connecting the electrodes to programmed switches. By connecting output data automatically, it is possible to compare them by the program and find optimized compositions or doping concentrations quickly.

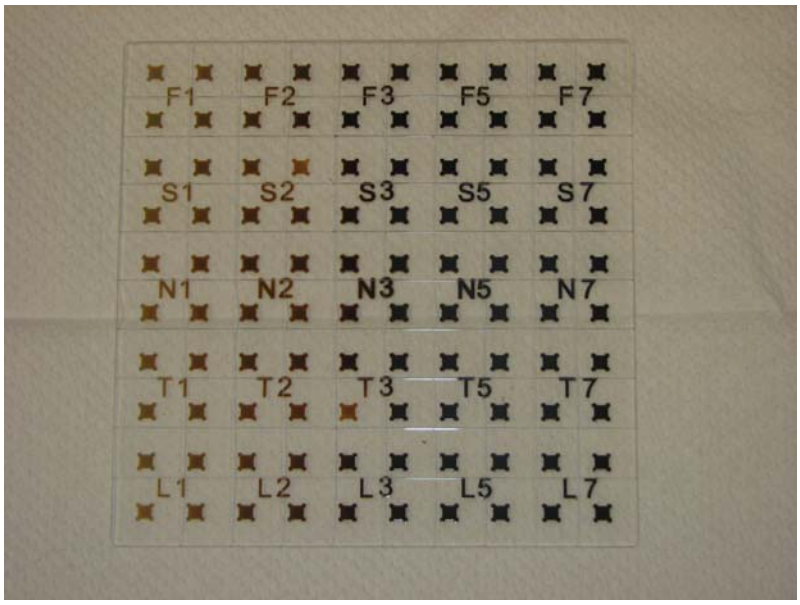

Figure 4.16 A picture of a fused quartz substrate with 10X10 samples and labels.

Figure 4.17 An ellipsometer with a homemade stage for automatic scanning measurement.

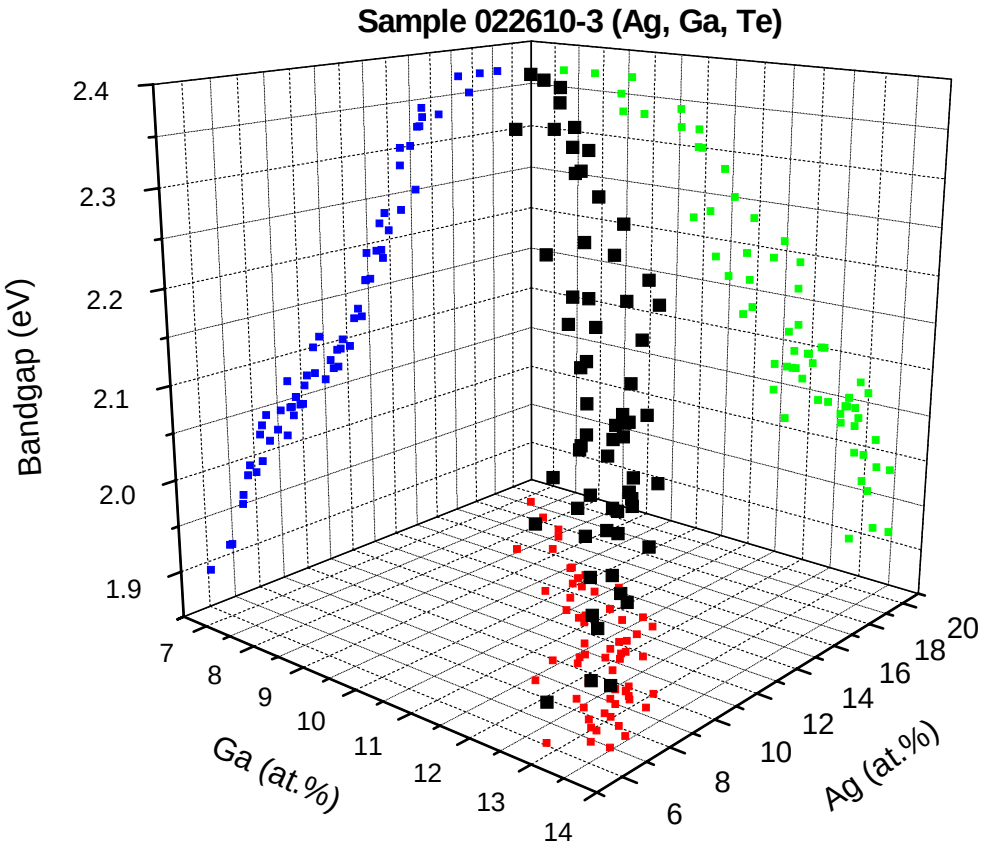

Figure 4.18 3D plot of (Ag, Ga)Te_2 with black dots showing relationship among Ga percentage (X axis), Ag percentage (Y axis) and their bandgap (Z axis). The red, blue, and green dots are the projections on XY, YZ and XZ planes, respectively.

3) Instead of depositing different precursor materials layer by layer, this technique deposits different precursor materials simultaneously. This avoids the troublesome and problematic annealing process in combinatorial synthesis. Deposited films are supposed to be uniform only if deposition parameters are not changed during deposition process. In combinatorial synthesis, since precursor materials are deposited layer by layer, post annealing is necessary in order to ensure uniform diffusion of precursors and subsequent phase formation. However, this process sometimes has been shown to be problematic. It is sometimes difficult to find a suitable annealing temperature to achieve uniformity without significant evaporation of deposited materials. If annealing temperature is too high, there might be problems associated with non-stoichiometry. If samples are annealed at a lower temperature, it needs a very long time and also a complex process. In Xiang *et al.*'s previous work [19], annealing was proceeded as follows: 200 °C for 150 hours, 400

°C for 24 hours, and 600°C for 12 hours, followed by treatment at 1000 °C for 2 hours in a high-purity argon flow (with temperature ramping rates of 1 °C per minute). Furthermore, this annealing process is very likely to see some other phases of precursor materials. For example, for deposition of materials A, B, followed by material C, it is very likely to get a stable phase only consisting of materials A and B (abbreviated as AB), or other phases like BC, instead of phase ABC with complete mixing.

4) It is much easier for this technique to deposit thick films. In order to deposit thicker films, it just needs to deposit for a longer time. However, since combinatorial synthesis needs post annealing to achieve uniformity, each layer of the precursor can not be too thick. Otherwise it will have problems in achieving a uniform mixture. Therefore combinatorial synthesis needs more processes for growing thick films. For example, in order to deposit 1.5 μm thick film of ABC, it may need a series of processes, like 30 nm A, 30 nm B, 30 nm C….. That makes it necessary to keep changing targets during deposition.

5) This technique does not have misalignment problem. In combinatorial synthesis, non-uniform distribution of precursors is controlled by using physical masks. In order to grow a library of materials on a substrate, combinatorial synthesis needs a series of masks and change and alignment of masks during deposition. All of these processes are being done mechanically and manually. It is not easy to do these processes in a vacuum chamber. There are always some alignment errors. Usually for an element, you may see many misaligned squares. The mechanical alignment process might be problematic due to thermal expansion if the substrate is heated.

6) The composition change of element samples grown by this technique is ordered and continuous, which is good for automatic measurement and fast screening. In order to save time and find good samples quickly, measurement of all the samples therefore is not necessary. One sample can be picked out from every four or nine neighbored samples. Detailed measurement can be performed later when interesting properties are found.

7) The process is much simpler and the system is much cheaper. It does not need to change masks or targets during the whole deposition process. Therefore these complex mechanical parts are avoided.

8) It is also very easy and reliable for this technique to heat the substrate during deposition. In-situ heating is very important for deposition of most materials. However, in combinatorial synthesis, if the substrate is heated, mechanical alignment of masks has been proved to be very difficult. More steps for in-situ heating may thus be needed. In addition, in-situ heating may cause lower-order phases such as previously mentioned AB and BC phases, which, if they are stable, are often difficult to be removed later in post annealing.

9) This technique is more flexible. By changing only one mask, the size of each element sample, the total number of samples, or distribution of the samples, or even the size of the substrate can be changed easily. However, if a series of masks and these masks

are mounted and aligned critically on a mask holder, change of masks or size of element samples is extremely difficult.

10) The distribution of precursors on substrate is easy to be changed for various experimental purposes. Sharp composition change may be needed for fast screening. Sometimes small variation may be needed for detailed characterization. The precursor distribution can be easily changed by adjusting substrate-to-target distance, ambient gas pressure, and even distance between the plumes. More gradual change of compositions is expected at a larger substrate-to-target distance. [22] The distribution can also be changed by adjusting ambient gas pressure during deposition. In addition, it is also easy to change the distance between laser spots by adjusting the beam splitters and the mirror as shown in Figure 4.19. Laser spot positions on targets can be changed, and as a result the positions of the plumes can be changed, which obviously will affect precursor distribution on substrate.

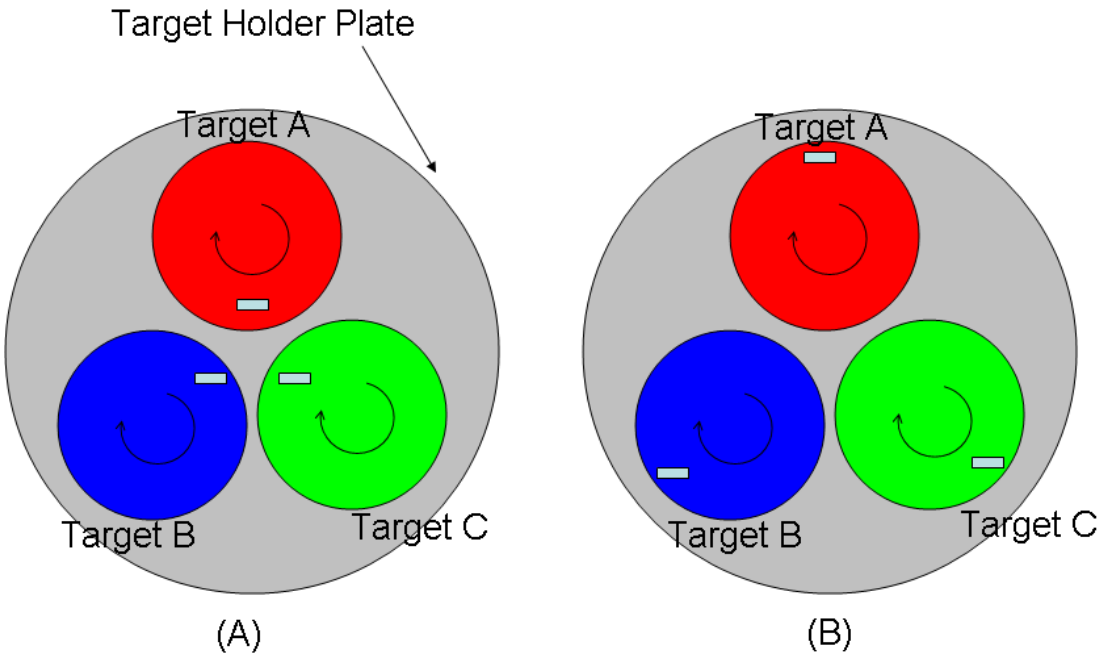

Figure 4.19 Schematic of the target holder showing different spot distances (A) close spots (B) spots are far away. Rectangles represent focused laser spots.

4.4 Batch Growth of Thin Films with Different Compositions and Deposition Temperatures

With change of compositions for different samples on the substrate, the deposition temperature may need to be changed for different films on the same substrate, especially for those materials whose melting temperature changes greatly with composition. Fortunately, because of the energetic species, growth temperature of pulsed laser

deposition can be much lower than other techniques. Another way to solve this problem is to combine the temperature gradient and composition gradient, as illustrated in Figure 4.20. With positioning two plume centers parallel to the lines, the compositions mainly change along the line direction. With heating at one edge of the substrate holder, temperature gradient along the column direction can be obtained. Therefore, on the same substrate, thin films with different compositions and deposition temperatures can be obtained.

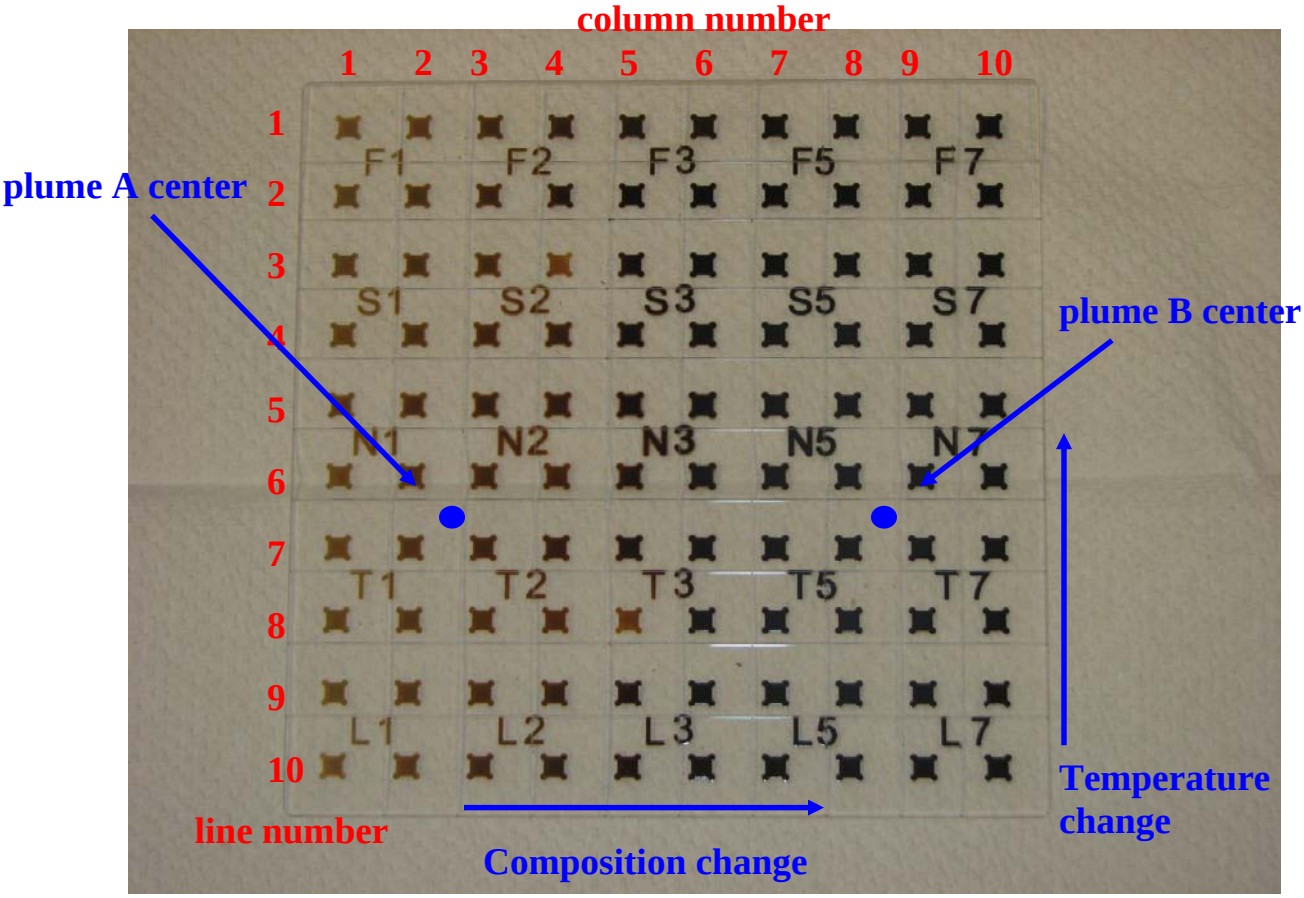

Figure 4.20 A picture of a fused quartz substrate with 10X10 samples and labels.

4.5 Summary

Batch growth of thin films with different deposition temperatures or compositions has been tried. A natural temperature gradient has been used for batch growth of thin films with different deposition temperatures. A low-cost, high-efficiency multi-plume pulsed laser deposition system has been proposed and compared to previous techniques in detail. With directionality of PLD plumes and non-uniformity of PLD film thickness, this system is promising for high-throughput compound thin film fabrication.

References:

[1] U. Ozgur, Y. I. Alivov, C. Liu, A. Teke, M. A. Reshchikov, S. Dogan, V. Avrutin, S. J. Cho, and H. Morkoc, Journal of Applied Physics **98** (2005).

[2] H. Morkoc, S. Strite, G. B. Gao, M. E. Lin, B. Sverdlov, and M. Burns, Journal of Applied Physics **76,** 1363-1398 (1994).

[3] M. Y. Chern, H. M. Lin, C. C. Fang, J. C. Fan, and Y. F. Chen, Applied Physics Letters **67,** 1390-1392 (1995).

[4] J. L. Deiss, A. Chergui, L. Koutti, J. L. Loison, M. Robino, and J. B. Grun, Applied Surface Science **86,** 149-153 (1995).

[5] T. Ganguli, M. Vedvyas, P. Bhattacharya, L. M. Kukreja, A. Ingale, K. P. Adhi, K. S. Chandrashekharan, B. M. Arora, and K. C. Rustagi, Thin Solid Films **388,** 189-194 (2001).

[6] Y. R. Ryu, S. Zhu, S. W. Han, H. W. White, P. F. Miceli, and H. R. Chandrasekhar, Applied Surface Science **127,** 496-499 (1998).

[7] J. L. Lei, F. McLarnon, and R. Kostecki, Journal of Physical Chemistry B **109,** 952-957 (2005).

[8] I. Kikuma and M. Furukoshi, Journal of Crystal Growth **71,** 136-140 (1985).

[9] G. E. Hite, D. T. F. Marple, M. Aven, and B. Segall, Physical Review **156,** 850 (1967).

[10] J. Gutowski, N. Presser, and G. Kudlek, Physica Status Solidi a-Applied Research **120,** 11-59 (1990).

[11] Y. D. Kim, S. L. Cooper, M. V. Klein, and B. T. Jonker, Applied Physics Letters **62,** 2387-2389 (1993).

[12] A. M. Klimova, V. A. Ananichev, M. Arif, and L. N. Blinov, Glass Physics and Chemistry **31,** 760-762 (2005).

[13] I. Repins, M. A. Contreras, B. Egaas, C. DeHart, J. Scharf, C. L. Perkins, B. To, and R. Noufi, Progress in Photovoltaics **16,** 235-239 (2008).

[14] M. A. Contreras, B. Egaas, K. Ramanathan, J. Hiltner, A. Swartzlander, F. Hasoon, and R. Noufi, Progress in Photovoltaics **7,** 311-316 (1999).

[15] A. Ennaoui, S. Siebentritt, M. C. Lux-Steiner, W. Riedl, and F. Karg, Solar Energy Materials and Solar Cells **67,** 31-40 (2001).

[16] T. M. Chuang, M. P. Allan, J. Lee, Y. Xie, N. Ni, S. L. Bud'ko, G. S. Boebinger, P. C. Canfield, and J. C. Davis, Science **327,** 181-184.

[17] L. Gao, Y. Y. Xue, F. Chen, Q. Xiong, R. L. Meng, D. Ramirez, C. W. Chu, J. H. Eggert, and H. K. Mao, Physical Review B **50,** 4260-4263 (1994).

[18] X. D. Xiang, X. D. Sun, G. Briceno, Y. L. Lou, K. A. Wang, H. Y. Chang, W. G. Wallacefreedman, S. W. Chen, and P. G. Schultz, Science **268,** 1738-1740 (1995).

[19] J. S. Wang, Y. Yoo, C. Gao, I. Takeuchi, X. D. Sun, H. Y. Chang, X. D. Xiang, and P. G. Schultz, Science **279,** 1712-1714 (1998).

[20] G. Briceno, H. Y. Chang, X. D. Sun, P. G. Schultz, and X. D. Xiang, Science **270,** 273-275 (1995).

[21] D. Dijkkamp, T. Venkatesan, X. D. Wu, S. A. Shaheen, N. Jisrawi, Y. H. Minlee, W. L. McLean, and M. Croft, Applied Physics Letters **51,** 619-621 (1987).

[22] M. Tyunina, J. Wittborn, C. Bjormander, and K. V. Rao, Journal of Vacuum Science & Technology A **16,** 2381-2384 (1998).

[23] S. I. Anisimov, B. S. Lukyanchuk, and A. Luches, Applied Surface Science **96-8,** 24-32 (1996).
[24] S. I. Anisimov, B. S. Luk'yanchuk, and A. Luches, Journal of Experimental and Theoretical Physics **81,** 129-138 (1995).